INVESTIGATION OF THE INTERACTION BETWEEN A HUMAN INDEX FINGER AND SPACESUIT GLOVE

A Thesis

by

PATRICK JOHN CHAPATES

Submitted to the Office of Graduate and Professional Studies of
Texas A&M University
in partial fulfillment of the requirements for the degree of

MASTER OF SCIENCE

Chair of Committee,	Bonnie J. Dunbar
Co-Chair of Committee,	John D. Whitcomb
Committee Members,	Darren J. Hartl
	Thomas K. Ferris
Head of Department,	Rodney Bowersox

May 2019

Major Subject: Aerospace Engineering

ABSTRACT

With over five decades of spaceflight experience, from the Mercury Program to the current International Space Station, it is well recognized that Extravehicular Activity (EVA), is a critical operational capability necessary for successful space habitation. Whether in LEO or on the Lunar and Martian surfaces, an EVA suit must provide life support systems, communication, power, thermal protection and radiation protection. In addition to these functions, the EVA suit must be comfortable and not inhibit the performance of the human. A critical component of the EVA suit are the gloves. Whether it be for exterior assembly, maintenance or science-based surface operations, there will be a continued reliance on manual tasks, requiring fine use of a crew member's hands. The long duration nature of a Lunar or Martian mission requires spacesuit gloves to be reliable, durable and nearly invisible to the crew-member. While several researchers have studied the effects of EVA Gloves and pressurization on hand strength, dexterity and tactility, these efforts relied on exterior measures of the performance of a glove. Although measures such as grip strength, range of motion and task completion time are valid metrics for how well a glove performs, they provide little insight on the mechanics of the human-glove interaction. To engineer the best glove for future LEO, Lunar and Martian EVA missions, it is critical to develop a deeper understanding of the complex interactions that take place inside of the glove. A finite element model of the interaction between the human index finger and notional EVA glove pressure bladder and restraint layer was developed to further understand this interaction. It was found that material modulus was the largest contributing factor (accounting for approximately 72% of overall stiffness) followed by bunching of the glove (accounting for approximately 25% of overall stiffness). It was also determined that pressure had minimal effect on the overall stiffness of the EVA glove finger. Additionally it was found that the pre-bunching of the restraint layer significantly reduced the overall stiffness of the glove finger. Finally, it was shown that material modulus and thickness of the restraint layer, material thickness of the pressure bladder and convolute size had the largest effects on glove stiffness.

DEDICATION

I dedicate this thesis to all of those close to me who have encouraged me to never stop in the pursuit of knowledge. Their leadership has inspired me to always hunger to know more.

ACKNOWLEDGMENTS

I give my sincerest thanks to Dr. Dunbar, Dr. Whitcomb and Dr. Hartl who provided tremendous support throughout my time at Texas A&M. I would like to specially acknowledge Dr. Whitcomb for his encouragement to pursue graduate school and his guidance during my undergraduate years and graduate years, Dr. Dunbar for her guidance and expertise on all things human-spaceflight related and Dr. Hartl for his guidance and teaching on all things related to this thesis. I would also like to acknowledge the Aerospace Human Systems Lab, the Department of Aerospace Engineering and Texas A&M University for the opportunity to pursue this research.

CONTRIBUTORS AND FUNDING SOURCES

Contributors

This work was supported by a thesis committee consisting of Professor Bonnie J. Dunbar [advisor], Professor John D. Whitcomb [co-advisor] and Professor Darren J. Hartl of the Department of Aerospace Engineering and Professor Thomas K. Ferris of the Department of Industrial Engineering. All work conducted for the thesis was completed by the student independently.

Funding Sources

This work was funded by the TAMU Aerospace Human Systems Laboratory (AHSL) under the directorship of Professor Bonnie J. Dunbar, and the generous support of the Chancellor's Research Initiative (CRI).

NOMENCLATURE

EVA	Extravehicular Activity
NASA	National Association of Space and Aeronautics
EMU	Extravehicular Mobility Unit
ISS	International Space Station
TMG	Thermal Micrometeoroid Garment
HUT	Hard Upper Torso
LTA	Lower Torso Assembly
FEA	Finite Element Analysis
FEM	Finite Element Method
DIP	Distal Interphalangeal Joint
PIP	Proximal Interphalangeal Joint
M_{DIP}	Joint Torque about DIP Joint
M_{PIP}	Joint Torque about PIP Joint
R_{DIP}	Rotation of DIP Joint
R_{PIP}	Rotation of PIP Joint

TABLE OF CONTENTS

Page

LIST OF FIGURES

FIGURE Page

LIST OF TABLES

TABLE Page

1. INTRODUCTION

1.1 Introduction

Space is an inherently inhospitable environment. Astronauts in Low-Earth Orbit (LEO) experience temperatures from $-170°C$ to $123°C$ with an atmospheric pressure of approximately $10^{-6}torr$ [1]. The surfaces of the moon and Mars are not any more hospitable to humans, with a temperature range of $-173°C$ to $127°C$ [2] and $-55°C$ to $20°C$ [3] and an atmospheric pressure of $10^{-6}torr$ [2] and $4.49torr$ [3] respectively. Because of these environments, it is necessary to provide the appropriate environmental control and life support systems for crewmembers.

As humans continue to operate in LEO, plan to return to the Moon, and eventually journey to Mars, the ability to perform Extravehicular Activity (EVA) remains a necessity. Whether it be to assemble a space station, perform routine maintenance, conduct scientific experiments, or explore the surface of a planetary body, EVA is a fundamental component of future human-spaceflight mission architecture. To sustain human life in the hostile environment of space, a spacesuit must act as a form-fitting spacecraft complete with all of the life support systems present in a full-sized spacecraft. A spacesuit must provide a pressurized environment as well as thermal, radiation and micrometeoroid protection to the crewmember inside. In addition to providing multi-layered material protections, the spacesuit must be form-fitting, flexible and not significantly inhibit the crewmember. The added bulk provided by the suit, combined with the internal pressurization result in a garment that can significantly reduce crew productivity and performance. EVA gloves are a critical component of the EVA suit. Whether it be for exterior assembly, maintenance or science-based surface operations, crewmembers will continue to perform dexterous tasks using their hands. Because of this, it is critically important to understand the fundamental causes for performance degradation caused by the EVA gloves. This section will provide a background on Extravehicular Activity, NASA's Extravehicular Mobility Unit, the Phase VI EVA glove and provide a literature survey of prior analysis of EVA gloves and the methodology that was used in this research.

1.2 Extravehicular Activity (EVA)

Extravehicular activity (EVA) refers to all activities performed by an astronaut outside of a spacecraft or habitat in the environment of space. The first human to perform a spacewalk was Russian cosmonaut, Alexey Leonev, on March 18th, 1965 during the Voskhod 2 mission (Figure 1.1). Leonev's EVA lasted 24 minutes [4]. While reports at the time claimed that Leonev's EVA proceeded without difficulty, later reports revealed that Leonev struggled to work against the pressure of the ballooned suit, had to partially depressurize his suit to return through the airlock and nearly suffered heat-stroke [4]. While the first spacewalk was not trouble-free, Leonev did successfully demonstrate EVA capability.

Figure 1.1: Alexey Leonev Voskhod 2 EVA (1965) [5]

Less than three months later, on June 3rd, 1965, astronaut, Ed White, became the first American to perform an EVA - lasting 36 minutes during the Gemini 4 mission [4] (Figure 1.2). White successfully demonstrated the United State's ability to perform EVA, a critical step to realizing the goal of having man walk on the moon. Objectively, the EVA was successful. White reported that his suit operated well and was comfortable. The only trouble occurred when White attempted to close the hatch upon re-entering the spacecraft. White struggled to close hatch, overheated

and exceeded the cooling capability of the Gemini 4C suit. This caused fogging of White's visor. Despite this shortcoming, the EVA demonstration was considered successful [4]. While Leonev and White's EVAs were extremely short duration and solely for the purpose of demonstrating the capability, they were a critical leap forward in human spaceflight. For the U.S., this demonstration proved that a critical, component of the Apollo mission architecture was possible.

Figure 1.2: Ed White Gemini 4 EVA (1965) [6]

While NASA continued to perform EVAs in later flights of the Gemini program (with a total of 9 EVAs across the program), 3 of the EVAs were terminated prematurely due to crew fatigue or overheating [4]. This problem underscores a significant shortcoming in thermal management and operability of the EVA suit at the time. It wasn't until Gemini 12 that the first true long duration EVA was performed. On November 13th, 1966, Buzz Aldrin performed a spacewalk lasting 2 hours and 18 minutes [4] (Figure 1.3). This was a critical demonstration that proved the long duration surface EVAs planned for the Apollo missions were possible.

Figure 1.3: Buzz Aldrin Gemini 12 EVA (1966) [7]

Nearly three years later, on July 21st, 1969, Neil Armstrong and Buzz Aldrin became the first humans to perform an EVA on the surface of the moon (Figure 1.4), lasting 2 hours and 32 minutes. A total of fifteen Lunar EVAs were performed across the subsequent Apollo missions [4].

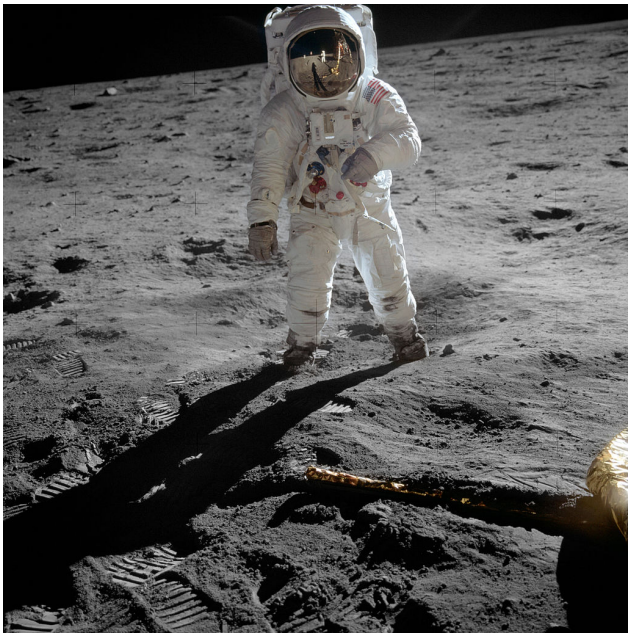

Figure 1.4: Apollo 11 EVA [8]

Following the Apollo program, the next advancement in EVA capability occurred during NASA's Skylab program. During Skylab 2, Pete Conrad, Joseph Kerwin, and Paul Weitz performed the first repairs of a spacecraft through EVA. The three man crew performed a total of three EVAs from May 26 to June 19, 1973 to repair stuck solar panels and a stuck circuit breaker (Figure 1.5). Throughout the duration of the Skylab program, a total of ten EVAs across three crews of three men each were performed [4].

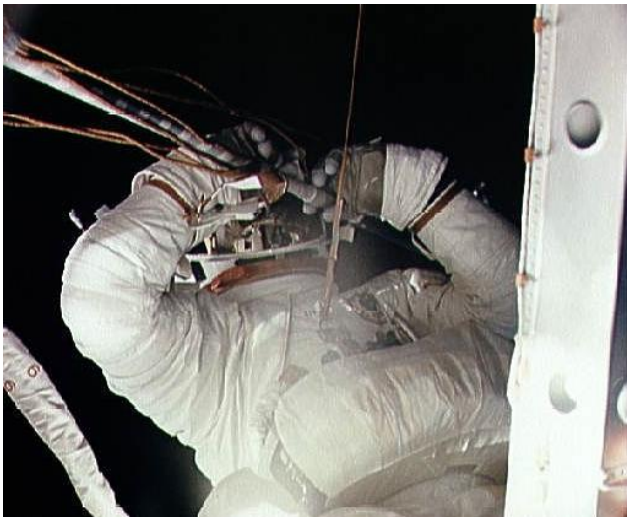

Figure 1.5: Skylab 2 EVA [9]

After the Skylab program was terminated, there were no further human spaceflight missions until the U.S. resumed EVAs during the Space Shuttle Program (1981-2011) and continues to perform EVAs through the International Space Station (ISS) program (1998-Present).

The capability to perform EVA enabled the assembly of the ISS and it still enables critical maintenance to aging ISS components as well as support for scientific experiments. Without EVA capability, the ISS could not have been assembled. As humans continue to inhabit the LEO environment and look toward long-duration Lunar and Martian missions, the ability to safely and routinely perform EVA remains an utmost priority.

1.3 EVA Suits and Gloves

1.3.1 NASA Extravehicular Mobility Unit (EMU)

All of the suits used in the aforementioned EVAs shared a number of key characteristics. In addition to serving as a flexible pressure vessel with its own internal pressurized atmosphere, the suits provided humidity control, thermal control, power, command/control, communications, and radiation protection to the crewmember. All of these requirements result in a spacesuit with many complex layers that significantly inhibit the performance of the human.

The most successful suit, as determined by the Apollo and Skylab astronauts, was the A7LB. This suit was custom made and comprised primarily of soft materials [10]. After the completion of the Skylab program, NASA developed the next-generation suit, the Extravehicular Mobility Unit (EMU), for use in the subsequent Space Shuttle program. In 1974, Hamilton United and ILC Dover received a contract to design and develop what would become the EMU. NASA received the first production unit in 1982 [11]. The first EVA using the EMU was performed on STS-6 by Story Musgrave and Donald Peterson. This version of the EMU was successfully used through STS-110 and was eventually replaced by an updated version, the Enhanced EMU [11]. The Enhanced EMU was largely unchanged, but included enhancements to sizing of the arms, sizing of the lower-torso assembly and arm-Hard Upper Torso and Hard Upper Torso-Lower Torso Assembly interfaces. [12].

The EMU was designed as an orbital EVA suit, meaning that it was never intended to operate on planetary surfaces. The EMU is comprised of a Hard Upper-Torso (HUT) with softgood legs, arms and gloves as well as a separate helmet. Figure 1.6 shows the enhanced EMU in use on STS-118. Unlike the custom made suits of Mercury, Gemini, Apollo and Skylab, the EMU was first manufactured in 5 HUT sizes, with sizing modifications available in the soft-good arms and legs. Helmets and neck wrings were manufactured in one size only [10].

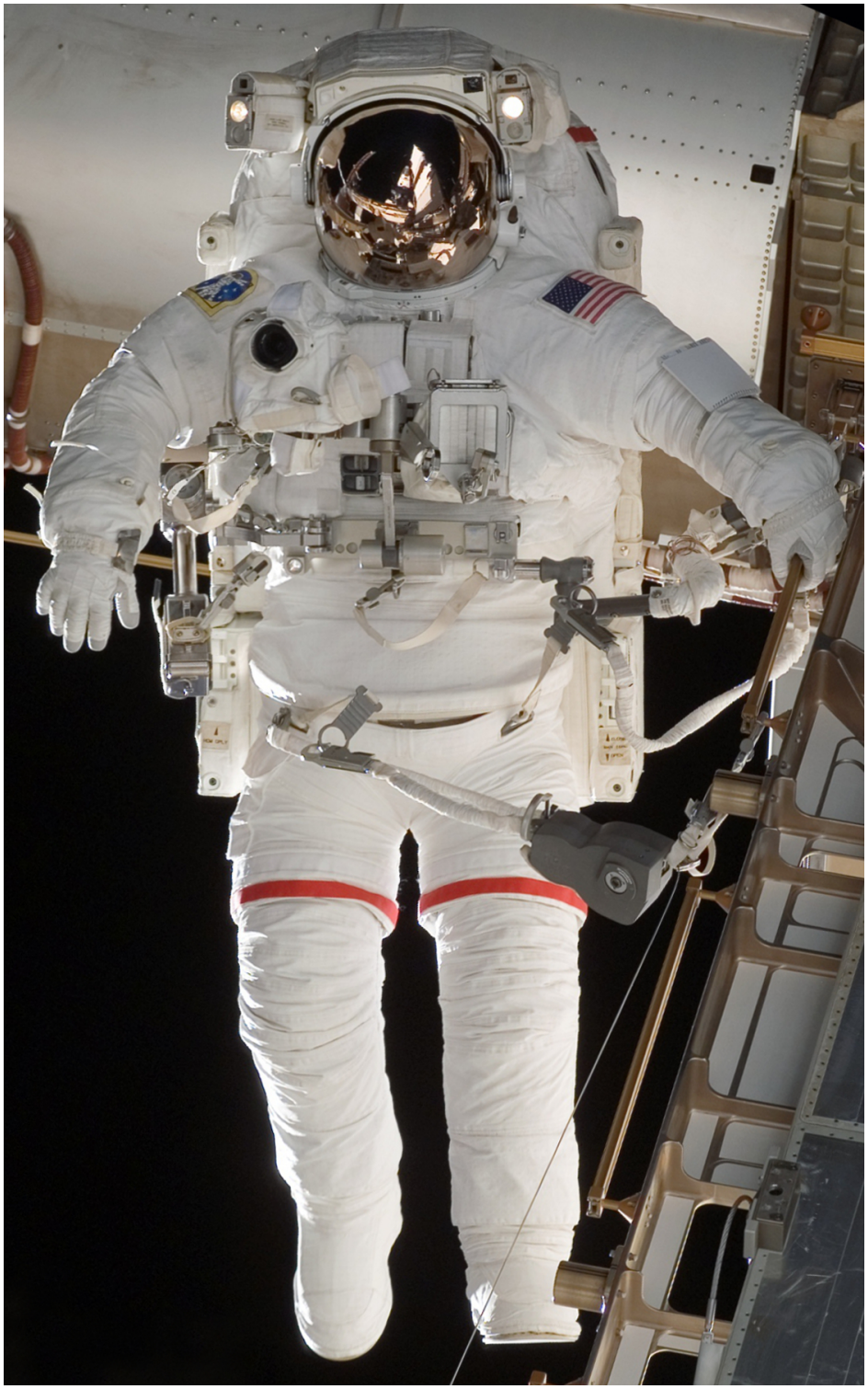

Figure 1.6: NASA Enhanced EMU [13]

The softgoods of the suit (neglecting the gloves) are comprised of 14 individual layers (Figure

1.7) [14]. The first three layers (closest to the crewmembers body) comprise a separate garment, the Liquid Cooling and Ventilation Garment (LCVG). This is a form-fitting nylon garment with small tygon tubes woven throughout. The tubing transports water to regulate the temperature crewmember. The next layer is the pressure bladder. The pressure bladder is comprised of urethane coated nylon. The purpose of this layer is to provide an air-tight bladder inside of the suit. Next is the restraint layer. The restraint layer is composed of a nylon ripstop fabric. The purpose of the restraint layer is to carry the pressure and man-induced loads inside of the suit as well as to provide shape to the pressure bladder. The remaining layers provide thermal and micrometeoroid protection [14].

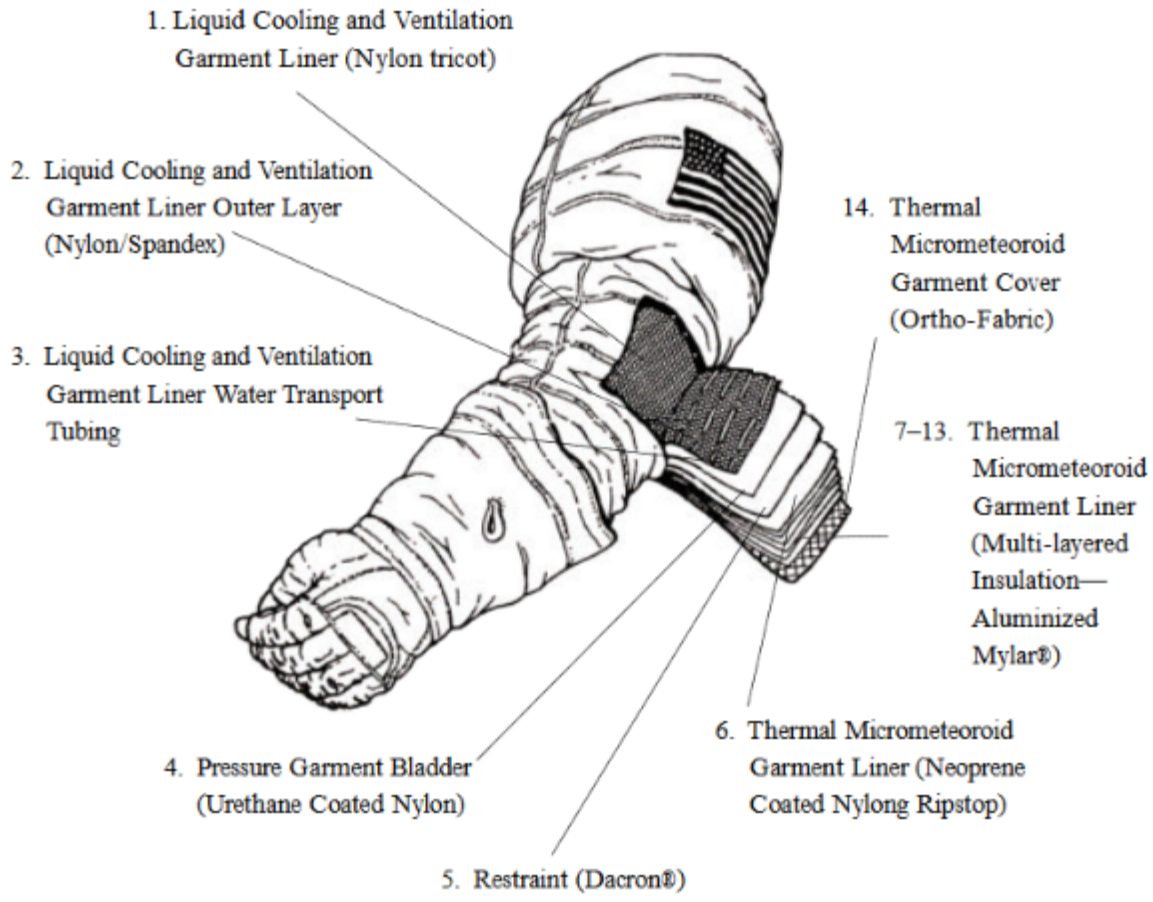

Figure 1.7: Layers of NASA EMU [14]

While the purpose of the soft-good components of the EMU are identical to those in the EVA glove, the EVA glove follows a different design. The remainder of this thesis will focus on the EVA glove.

1.3.2 Phase VI EVA Glove

The current gloves used in the EMU are the Phase VI EVA gloves developed by ILC Dover. The Phase VI gloves connect with EMU arms via a rigid bearing connector and are comprised of three main layers. Figures 1.8, 1.9, 1.10 show each layer of the Phase VI glove [15].

Figure 1.8: EVA Glove Pressure Bladder [16]

Figure 1.9: EVA Glove Restraint Layer [17]

Figure 1.10: EVA Glove Thermal Micrometeoroid Garment [13]

The innermost layer is the pressure bladder. The pressure bladder is comprised of a dipped urethane membrane and is a thin, elastic, conformal membrane whose sole purpose is to maintain an airtight environment around the human hand. The fingers of the pressure bladder have convolutes on the dorsal surface. These convolutes aide in reducing the bending stiffness of the glove [15]. Figure 1.11 illustrates the convolutes on the index finger of the Phase VI pressure bladder.

Figure 1.11: EVA Glove Pressure Bladder Convolutes

The middle layer of the Phase VI glove is the restraint layer. The restraint layer is a polyester woven (Dacron) textile [16]. The restraint layer is responsible for carrying all of the pressure loads and human-induced loads inside of the glove as well as maintaining the shape of the pressure bladder. The fingers of the restraint layer are oversized in length, and adjusted to optimal fit through the use of two adjustment chords along the side seams of the fingers. Figure 1.12 illustrates the sizing cords on the index finger of the restraint layer.

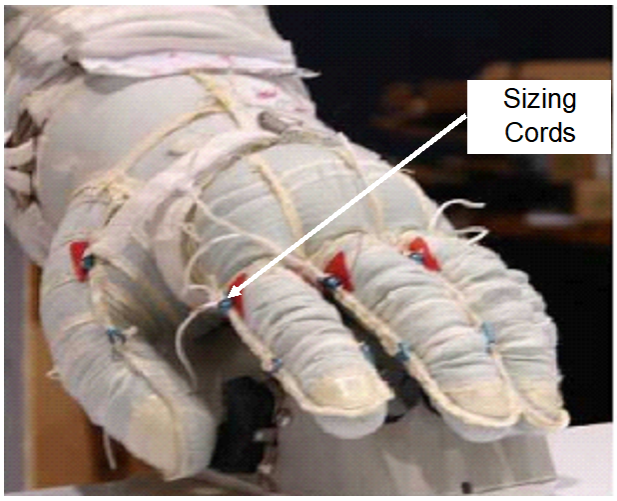

Figure 1.12: EVA Glove Restraint Layer Sizing Cords

The outermost layer is the Thermal Micrometeoroid Garment (TMG). The TMG is comprised of 7 layers of neoprene, nylon ripstop, aluminized Mylar, Dacron and Ortho-Fabric. These layers provide thermal, impact and radiation protection to the crew-member and the other layers of the glove.

All Phase VI gloves used on orbit are custom fit or custom manufactured to the specific anthropometrics of a crewmembers hand. This process starts with a plaster cast of the crewmembers hand. The cast is then scanned using a 3D laser scanning system. This produces an accurate computer model of the crewmembers hand. From there, proprietary CAD algorithms are used, and an SLA mold for the pressure bladder and flat-patterns for the restraint layer and TMG are made [15].

1.4 Analysis of EVA Gloves

From initial development of EVA gloves in the 1960s, engineers have been interested in studying the effects of EVA gloves on hand performance. However, the first published study was performed by O'Hara et al. in 1988 [18]. This study was the first to propose evaluating EVA gloves based on mobility, dexterity and strength. A more detailed study, based on the work of O'Hara, was performed by Bishu and Klute in 1993 [19] [20] [21]. The researchers performed a systematic study of grip strength, pinch strength and dexterity measures for the Phase 3000 EVA glove (the predecessor to the Phase VI) as well as two development gloves at a suit pressure of 0 PSID and 4.3 PSID defined as the differential pressure between the interior of the glove and ambient environment. Each test was also performed with and without the TMG layer of the glove. The researchers found that, although there was significant variance across test-subjects, EVA gloves reduced hand strength to approximately 50% of ungloved strength on average without the internal pressure of the suit. The researchers found additional strength decrements caused by the addition of pressurization and the TMG layers of the glove. However, the numerical values of the further strength decrement was inconsistent between subjects.

Mesloh et al. performed a similar study to Bishu on the Phase VI Glove. Mesloh showed that simply by donning the pressure bladder and restraint layer of the Phase VI EVA glove, subject's hand strength was reduced to 66% of their bare-hand strength [17]. By pressurizing the glove, the subject's hand strength was further reduced to 58% of their ungloved strength. The addition of the TMG (while pressurized) was shown to further reduce subjects' hand strength to 46% of their nominal strength. This study utilized external measures of glove performance during operation of the glove by a human subject, namely grip strength measured with a dynomometer. While the measurement of subjects' grip strength in various glove configurations can provide quantitative measurements of glove stiffness, it cannot provide insight into the complex interactions happening inside of the glove that lead to the resulting stiffness.

Additionally, it has been shown that the Phase VI glove can initiate injuries such as fingernail delamination [22] in some crewmembers. While the exact cause of the increased injury risk is

unknown, a number of studies have been performed in an attempt to determine the root cause of the issue. Farran et al. have shown humidity to be a potential cause due to deterioration of fingernail strength [23]. Opperman et al. used an array of pressure transducers and a Laser Doppler Flowmetry (LDF) probe to correlate blood flow reduction in the finger to finger pressure [24]. Their study concluded that the fingerpad pressure required to move the pressurized glove was more likely to cause injury due to blood flow restriction than a tight fitting glove.

Additional work has been done to develop an instrumented glove for subject's to wear inside of the EVA glove. Reid and McFarland performed a feasibility assessment of using an interior glove equipped with sensors to evaluate contact pressure, moisture, and temperature inside of the Phase VI glove [25]. As part of this feasibility study, NASA's EC2 Soft Goods group designed and fabricated comfort gloves to carry all of the sensors. This design was based on a previous University Collaboration study with Georgia Tech, Virginia Tech and Rhode Island School of Design. While this study did determine that an array of sensors that could be used inside of the glove, an instrumented comfort glove still adds an additional layer to the glove and can potentially alter the interaction between the hand and glove.

NASA's High-Performance EVA Glove (HPEG) project is aimed at designing the next generation EVA glove that mitigates injury risk and performance decrements present in the Phase VI glove. McFarland and Walsh's HPEG Project summary outlines the results of this project [26]. This report details the test methodology (external measure of glove performance such as grip strength and dexterity measures) for two candidate gloves developed by ILC Dover and David Clark Industries. Through all tests, the two candidate gloves showed no significant improvement in performance over the Phase VI glove. This lack of improvement demonstrates the need for a fundamental understanding of the interaction between the hand and glove.

Mousavi et al. developed an experimental setup to evaluate the stiffness of an index finger of the Russian Orlan EVA glove [27]. By using a mechanically actuated artificial finger, the researchers were able to vary joint torque and measure the resulting displacement of the finger. The researchers were then able to quantify the relationship between joint torque and joint rotation for

the Metacarpal-Phalangeal (MCP) joint, Proximal Interphalangeal (PIP) joint and Distal Interphalangeal (DIP) joint at various internal pressures of the glove. This study is the first to use internal measures of glove performance in an attempt to better understand the performance of the EVA glove. While this study provided valuable results, it still did not provide any detail into the driving forces and contributing factors of glove stiffness.

The literature available on the analysis of EVA gloves demonstrate a clear knowledge gap. While extensive work has been done to study the effects of EVA gloves on exterior performance measures such as grip strength or dexterity, these results do not provide adequate information about the interaction between the hand and glove inside of the glove. While an instrumented comfort glove could potentially provide some of the required insight, by adding sensors and an additional layer to the glove, it is likely that the interaction between the hand and glove would be altered. It is hypothesized that the powerful computational tools of finite element analysis lend themselves better to study the internal interaction between the hand and EVA glove.

Vishala et al. demonstrated the application of the powerful tool of Finite Element Analysis to study the interaction between an index finger and EVA glove pressure bladder [28]. The researchers demonstrated the capability to model contact between a deformable index finger and pressure bladder membrane. The researchers then applied an optimization technique in attempt to determine the optimal pressure bladder design to minimize glove stiffness. However, the model was limited to small motions of the index finger, the restraint layer was ignored, and the majority of the researchers' focus was on the optimization of pressure bladder design. Additionally, the computational model was not experimentally validated. However, the work by Vishala et al. forms the basis for the research that will be discussed in this thesis. Although, as Vishala's work is the only use of finite elements to model the interaction between a hand and glove in literature, prior work on finite element analysis of inflatable structures will also provide a background for this research.

1.5 Finite Element Analysis of Inflatable Structures

While little prior work has used FEA to model the interaction between the hand and EVA glove, extensive work has used FEA to model the behavior of inflatable structures. Elsabbagh developed

a nonlinear finite element model for analyzing axisymmetric inflatable beams [29]. Elsabbagh et al. showed how the finite element model can be used to predict the bending stiffness of inflatable beams as a function of inflation pressure. The researcher also demonstrates how the model can be used to predict wrinkling behavior of such a beam. While Elsabbagh et al. used the finite element model to solve a relatively simple problem, they concluded that the use of a nonlinear finite element model is a valid technique for analyzing real-life inflatable structures.

Gajbhiye et al. applied nonlinear finite element analysis to study the vibration behavior of an inflatable torus [30]. The researchers used Abaqus and theoretical models to compare the eigen-frequencies of the inflated torus for various aspect ratios. The researchers found that when considering the mass of the air inside of the inflated torus, a reduction in natural frequencies occurred. Ultimately, the researchers found good agreement among the analytical solution and the finite element model for understanding the dynamic response of an inflated torus structure.

Rowe et al. used ANSYS (a commercial finite element package) to model the behavior of inflatable aircraft wings [31]. The researchers were interested in the inflatable wing's response to bending and torsional loads. The researchers first performed lab-based experiments measuring resultant tip deflection and twist for applied specified loads on a scaled model. The experiments were performed on a half-span inflatable wing mockup and were repeated for various levels of internal pressure. The researchers then developed a finite element model of the wing using ANSYS. Their model included a non-linear static pressurization step and a non-linear static loading step following the pressurization. The researchers used this model to simulate both the bending and torsional tests. Ultimately, the researchers achieved good agreement between the experimental data and the finite element model. This study lends credibility to modeling the behavior of a pressurized structure through the use of subsequent non-linear pressurization steps and loading steps.

Sosa et al. used Abaqus and HYPERMESH to model the deployment of a large inflatable structure [32]. The researchers were working off of an existing set of experimental data on the inflation of a large plug contained in a tunnel. By using Abaqus' explicit dynamic solver, the researchers were able to successfully model the deployment and contact interaction between the

inflatable plug and tunnel. The model was comprised of steps modeling the folding, placement and inflation of this large-scale plug. The researchers conclude that the agreement of the finite element model with the experimental data mean that these modeling techniques can be used for parametric study and initial design. This study lends credibility to using Abaqus to perform a contact analysis between an inflatable membrane structure and a rigid body.

Glaser et al. also showed good agreement between finite element models and experimental data for the inflation of a thin-walled oblate spheroid [33]. The researchers compared various modeling techniques including both implicit and explicit formulations as well as multiple models for the gas dynamics during pressurization. In the end, a valid explicit quasi-static analysis of the inflation produced results that agreed well with the experimental results.

Many other researchers have shown that finite element analyses of inflatable structures, including large deformations of those structures can produce results that agree with experimental data [34] [35] [36] [37]. The extensive literature on using finite elements to model the behavior of inflatable structures including contact interaction has shown good agreement with experimental data. So although there is very little work in the available literature on modeling the interaction between a pressurized EVA glove and human hand, the modeling techniques used in the larger scope of inflatable structures have been shown to be credible and will be used in the following research. The aforementioned papers demonstrate the validity of using a finite element solver to model the interaction between the inflated (pressurized) EVA glove and a hand.

1.6 Quasi-Static Explicit Finite Element Analysis

Another area of research that is relevant to this thesis is the use of an explicit finite element solver to model quasi-static problems. The term quasi-static refers to dynamic processes that occur slow enough that they can be approximated as equivalent to static processes. In a quasi-static structural analysis, inertial terms should be negligible, meaning that static equilibrium is approximately satisfied across the analysis.

Explicit finite element analyses have been used widely in the automotive industry for the simulation of crash tests [38] [39]. Due to the robustness of an explicit analyses, it is able to handle

the highly dynamic problem with large deformations, material nonlinearity and contact analyses necessary for the simulation of vehicle collisions. The use of explicit analyses for solving dynamic problems has been shown to have good agreement with experimental results [40] [41]. While Explicit finite element analyses were originally used to model high-speed, highly dynamic structural events, there has been a large amount of research done that uses explicit finite element solvers to model quasi-static processes.

Lu et al. discuss the theoretical and practical application of an explicit finite element solver to solve quasi-static problems [42]. In the context of a fixed plate subjected to an out-of-plane load, the researchers studied the effects of mass-scaling and time-scaling on the accuracy of the explicit solution. Mass-scaling refers to artificially increasing the material density. Time scaling refers to altering the time-scale of the loading. The researchers conclude that using an explicit analysis to model a quasi-static problem is a useful technique for problems with large deformations, large amounts of contact or large nonlinearities. The researchers also conclude that care should be taken when utilizing mass-scaling and time-scaling to achieve lower computational expense. While some degree of oscillation in the results of an explicit analysis are unavoidable, one can easily introduce large amounts of error into one's model with careless use of mass scaling.

Explicit quasi-static analyses are commonly used to model the punching and drawing of metal components. Nakamachi et al [43] demonstrated the use of an explicit quasi-static analysis for modeling the forming of a hemispherical sheet metal part in 1996. The researchers systematically studied the effect of punch speed on the validity of the quasi-static results. Ultimately, when ensuring that the ratio of kinetic energy to internal energy of the finite element model was less than 0.1, the researchers achieved results that showed good agreement with the experimental data.

More recently, Gulavani et al. detailed the application of an explicit dynamic solver to model the quasi-static loading test used in certifying aircraft seats [44] [45]. The researchers chose to use an explicit analysis due to the large amount of contact analysis necessary to model this problem. The researchers highlighted some of the challenges with an explicit analysis, namely that equilibrium is only satisfied when using small time increments. This leads to a large amount of

timesteps necessary for solution. The researchers than present a systematic approach to validating quasi-static explicit analyses in the absence of experimental data. This includes starting with large mass-scaling factors and iterating until the ratio of kinetic energy to internal energy is less than 5%. Additionally, the authors suggest holding the loading constant at the end of a loading step to check for equilibrium. The researchers then demonstrate how these techniques can be used to study the behavior of aircraft seats. The researchers also show how the results from this quasi-static explicit analysis produce good agreement with experimental results.

Additionally, work by Yurdbak et al. demonstrate similar results to those found by Gulavani [46]. Yurdbak presented results on studying the effects of material density and loading time on the explicit quasi-static results for the simple problem of a plate with a hole. Yurdbak found that for a ratio of kinetic energy to internal energy of less than 10%, the explicit results agree with both the implicit finite element model as well as the closed-form analytical solution.

In summary, it has been well-demonstrated that with care to keep kinetic energy terms small, a dynamic explicit finite element analysis can produce accurate results when modeling quasi-static problems. While there is some disagreement across the literature of the exact threshold of this ratio for a valid quasi-static analysis, the exact ratios of these energies for this research will be presented whenever relevant. The prior literature validating explicit quasi-static analyses provides credibility to the methodology used in this research, and the guidelines used by the aforementioned researchers will be considered when performing the quasi-static analysis of the interaction between the hand and EVA glove.

1.7 Research Objectives

The main objective of this research is to develop a deeper understanding of the interaction between the human hand and EVA glove through the use of finite element analysis. Due to the complexity of this task, the scope of this research is limited to studying the interaction between the human index finger, the pressure bladder and restraint layer of the EVA glove. It is assumed that the methodology used in this research will eventually be applied to the entire hand. To develop this deeper understanding, a finite element model of an index finger as well as the index finger

portion of the EVA glove pressure bladder and restraint layer will be created. This model should incorporate realistic motions of the finger as well as contact analysis between all parts of the model. The outcomes of this research are threefold. The first outcome will be a robust model of the contact interaction between the index finger, pressure bladder and restraint layer. This model must be able to accommodate changes in glove geometry and material properties. The second outcome is an understanding of how suit pressure, bunching of the glove and material stiffness effect the overall stiffness of the EVA glove. The final outcome is a quantification of the sensitivity of glove stiffness to design parameters of the glove. The specific design variables of interest will be enumerated in the methodology section. These three outcomes, once validated through experimental data, could result in a greater understanding of the behavior of the hand-glove interaction that will eventually lead to glove designs that significantly reduce the risk of injury and performance degradation.

2. THEORY

2.1 Finite Element Method

This section provides the basics of the finite element method. In this section, Einstein's summation convention will be used. Additionally, tensorial quantities will be denoted using bold-faced variables. Einstein's summation convention states that repeating an index once in any given term implies summation over that term. For the purposes of this section, all summations will be from the range 1 to 3 representing an ortho-normal coordinate system. Equation 2.1 shows an example of Einstein's summation convention:

$$a_i x_i = \sum_{i=1}^{3} a_i x_i \tag{2.1}$$

The following sections will provide an overview of the governing equations of Continuum Mechanics: kinematics, measures of stress, constitutive relations and equilibrium. Following this, the weak formulation will be presented and the finite element method defined.

2.1.1 Kinematics

Kinematics describe the motion of a body. Kinematics can be used to describe both rigid body motion and deformation of a body. Kinematics is used to describe the deformation of a body. Figure 2.1 shows the motion of point P originally at location $\mathbf{X}$ at time t=0 and it's location $\mathbf{x}$ now at time t.

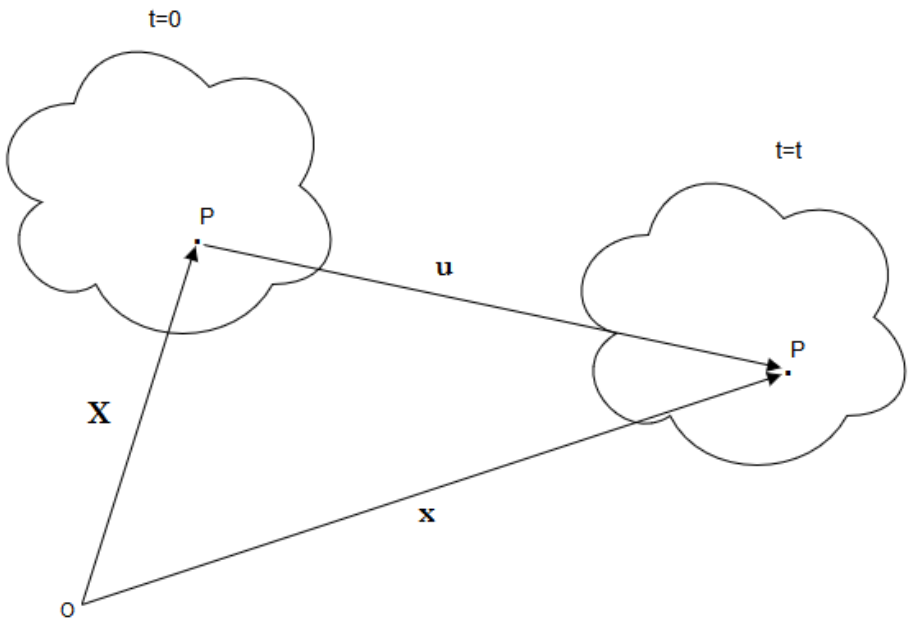

Figure 2.1: Motion of Material Point in Continuum Body

The motion of a material point can be described as below:

$$x_i = x_i(X_1, X_2, X_3, t) \tag{2.2}$$

Where (X_1, X_2, X_3) describes a specific material particle at time $t = 0$ and $\mathbf{x}$ describes the current position of the particle that resided at initial position $\mathbf{X}$ now at time t. The displacement of a material point is defined as:

$$u_i(X_1, X_2, X_3, t) = x_i(X_1, X_2, X_3, t) - X_i \tag{2.3}$$

This equation shows the displacement of material point initially at point $\mathbf{X}$ now at time t. While equation 2.3 describes the displacement of a material point of a body, it is desirable to be able to describe how the body deforms. Equation 2.4 defines the deformation gradient tensor, which is actually the gradient of the motion.

$$F_{ij} = \delta_{ij} + \frac{\partial u_i}{\partial x_j} \tag{2.4}$$

2.1.2 Stress

For the solution of Continuum Mechanics problems, it is also necessary to develop the notion and measures of stress. The definition of the stress tensor starts with the notion of contact forces. Consider slicing a body with a single cut. To maintain equilibrium, there must be a contact force acting on the surface of the cut. If one considers a small area, the ratio between contact force and contact area can be defined as below:

$$\frac{\Delta f_i}{\Delta A} \tag{2.5}$$

Taking the limit of this equation as the contact area shrinks results in the following limit:

$$\lim_{\Delta A \to 0} \frac{\Delta f_i}{\Delta A} \tag{2.6}$$

The Euler-Cauchy principle states that this limit exists and is only dependent on the outward normal of the contact area, n_i. Cauchy defines the value of this limit as traction as shown in Equation 2.7:

$$t_i = \lim_{\Delta A \to 0} \frac{\Delta f_i}{\Delta A} = \frac{df_i}{dA} \tag{2.7}$$

Cauchy also defined a linear transformation that transforms a unit normal to the resulting traction vector. This linear transformation is defined as the Cauchy Stress Tensor:

$$T_{ij} : n_j \to t_i \tag{2.8}$$

$$T_{ij} n_j = t_i \tag{2.9}$$

2.1.3 Conservation and Equilibrium

For further solution of Continuum Mechanics problems, it is necessary to express equilibrium. Cauchy's Equations of Motion are used to describe equilibrium. For an arbitrary body of density ρ subjected to body forces B_i and resulting acceleration a_i, equilibrium can be written in the

following way on on arbitrary control volume V with surface area A:

$$\int_A t_i dA + \int_V \rho B_i dV = \int_V \rho a_i dV \tag{2.10}$$

By writing the traction in terms of the Cauchy stress tensor and unit normal, the equilibrium equation becomes:

$$\int_A T_{ij} n_j dA + \int_V \rho B_i dV = \int_V \rho a_i dV \tag{2.11}$$

Equation 2.11 calls for the application of the Divergence Theorem. By applying the Divergence theorem to the first term, equilibrium becomes:

$$\int_V T_{ij,j} dV + \int_V \rho B_i dV = \int_V \rho a_i dV \tag{2.12}$$

Where $T_{ij,j,} := \frac{\partial T_{ij}}{\partial x_j}$ Combining terms in Equation 2.12 results in where $\forall V$ means for any volume, V:

$$\forall V \int_V (T_{ij,j} + \rho B_i - \rho a_i) dV = 0 \tag{2.13}$$

As Equation 2.13 is true for all control volumes, the integrand must be identically zero. Therefore, the equation of equilibrium becomes:

$$T_{ij,j} + \rho B_i - \rho a_i = 0 \tag{2.14}$$

For static equilibrium, $a_i = 0$ and the equation of equilibrium becomes:

$$T_{ij,j} + \rho B_i = 0 \tag{2.15}$$

2.1.4 Constitutive Relations

As the kinematics have been defined, and equilibrium is defined in terms of Cauchy stress, it is necessary to develop a relation between stress and strain.

Hooke determined that there exists a linear relation between stress and strain in a continuous body. That relation can be expressed between Cauchy's Stress tensor and the Green-Lagrangian strain tensor. Where the Green-Lagrangian strain tensor, E_{ij} is defined as follows:

$$E_{ij} = \frac{1}{2}(\frac{\partial u_i}{\partial x_j} + \frac{\partial u_j}{\partial x_i} + \frac{\partial u_i}{\partial x_j}\frac{\partial u_j}{\partial x_i}) \tag{2.16}$$

The constitutive relation states the relation between Cauchy Stress ($\mathbf{T}$) and Green-Lagrangian Strain ($\mathbf{E}$) is as follows:

$$T_{ij} = C_{ijkl}E_{kl} \tag{2.17}$$

This equation states that Stress is equal to a fourth order tensor, known as the stiffness tensor, double contracted into Green-Lagrange strain. The stiffness tensor (C_{ijkl}) is a fourth order tensor and, in general, would have 81 components. The constitutive relation can be inverted and written as follows:

$$E_{ij} = S_{ijkl}T_{kl} \tag{2.18}$$

One can make use of the symmetry of T_{ij} and E_{ij} and express both of these second order tensors as vectors using Voigt Notation:

$$\begin{pmatrix} T_1 \\ T_2 \\ T_3 \\ T_4 \\ T_5 \\ T_6 \end{pmatrix} = \begin{pmatrix} T_{11} \\ T_{22} \\ T_{33} \\ T_{23} \\ T_{13} \\ T_{12} \end{pmatrix} \tag{2.19}$$

$$\begin{pmatrix} E_1 \\ E_2 \\ E_3 \\ E_4 \\ E_5 \\ E_6 \end{pmatrix} = \begin{pmatrix} E_{11} \\ E_{22} \\ E_{33} \\ E_{23} \\ E_{13} \\ E_{12} \end{pmatrix} \tag{2.20}$$

Using Voigt notation, Hooke's law can be expressed as follows:

$$\begin{pmatrix} T_1 \\ T_2 \\ T_3 \\ T_4 \\ T_5 \\ T_6 \end{pmatrix} = \begin{pmatrix} C_{11} & C_{12} & C_{13} & C_{14} & C_{15} & C_{16} \\ C_{12} & C_{22} & C_{23} & C_{24} & C_{25} & C_{26} \\ C_{13} & C_{23} & C_{33} & C_{34} & C_{35} & C_{36} \\ C_{14} & C_{24} & C_{34} & C_{44} & C_{45} & C_{46} \\ C_{15} & C_{25} & C_{35} & C_{45} & C_{55} & C_{56} \\ C_{16} & C_{26} & C_{36} & C_{46} & C_{56} & C_{66} \end{pmatrix} \begin{pmatrix} E_1 \\ E_2 \\ E_3 \\ E_4 \\ E_5 \\ E_6 \end{pmatrix} \tag{2.21}$$

Similarly, the inverse relation can be written as follows:

$$\begin{pmatrix} E_1 \\ E_2 \\ E_3 \\ E_4 \\ E_5 \\ E_6 \end{pmatrix} = \begin{pmatrix} S_{11} & S_{12} & S_{13} & S_{14} & S_{15} & S_{16} \\ S_{12} & S_{22} & S_{23} & S_{24} & S_{25} & S_{26} \\ S_{13} & S_{23} & S_{33} & S_{34} & S_{35} & S_{36} \\ S_{14} & S_{24} & S_{34} & S_{44} & S_{45} & S_{46} \\ S_{15} & S_{25} & S_{35} & S_{45} & S_{55} & S_{56} \\ S_{16} & S_{26} & S_{36} & S_{46} & S_{56} & S_{66} \end{pmatrix} \begin{pmatrix} T_1 \\ T_2 \\ T_3 \\ T_4 \\ T_5 \\ T_6 \end{pmatrix} \tag{2.22}$$

For an isotropic material, the compliance matrix can be written in terms of Young's Modulus and

Poisson's Ratio as follows:

$$\begin{pmatrix} E_1 \\ E_2 \\ E_3 \\ E_4 \\ E_5 \\ E_6 \end{pmatrix} = \begin{pmatrix} \frac{1}{E} & \frac{-\nu}{E} & \frac{-\nu}{E} & 0 & 0 & 0 \\ \frac{-\nu}{E} & \frac{1}{E} & \frac{-\nu}{E} & 0 & 0 & 0 \\ \frac{-\nu}{E} & \frac{-\nu}{E} & \frac{1}{E} & 0 & 0 & 0 \\ 0 & 0 & 0 & \frac{1}{\mu} & 0 & 0 \\ 0 & 0 & 0 & 0 & \frac{1}{\mu} & 0 \\ 0 & 0 & 0 & 0 & 0 & \frac{1}{\mu} \end{pmatrix} \begin{pmatrix} T_1 \\ T_2 \\ T_3 \\ T_4 \\ T_5 \\ T_6 \end{pmatrix} \tag{2.23}$$

Hooke's Law states that all sub-matrices of this compliance matrix must be positive definite. For the purposes of this research, all materials were assumed to be isotropic and linearly elastic. This leads to a permissible range of Poisson's ratio ($-1 < \nu < \frac{1}{2}$) and of the bulk modulus ($\mu > 0$).

2.1.5 The Weak Formulation

While the equations of equilibrium can be solved analytically for a relatively small class of problems, as geometry and loading becomes more complex, it is not possible to integrate over the domain. Because of this limitation, it is necessary to solve most complex structural problems through numerical techniques. To do so, a displacement-based finite element method will seek to satisfy equilibrium in an average sense: that is equilibrium will be satisfied over a finite volume. The weak formulation for structural problems can be formulated using the principle of virtual work resulting in the vector equation of static equilibrium becoming a scalar equation integrated over a domain.

$$\int_V (T_{ij,j} + f_i)\delta u_i dV = 0 \tag{2.24}$$

Where δu_i is an arbitrary virtual displacement field of the domain. Using integration by parts and the definition of the Cauchy Stress tensor on Equation 2.24 results in the following:

$$\int_S t_i \delta u_i dS + \int_V f_i \delta u_i dV - \int_V T_{ij} \delta E_{ij} dV = 0 \tag{2.25}$$

This equation represents static equilibrium using the weak formulation. This will be used in the finite element formulation.

2.1.6 Finite Element Formulation

In the finite element formulation, the displacement field is approximated as the sum of a discrete number of interpolation functions multiplied by the displacement at each of the nodes of an element:

$$u_i = \sum_{k}^{n} N^k u_i^k \tag{2.26}$$

Where N^k is an interpolation function associated with node k and u_i^k is the displacement of node k in the x_i direction. The interpolation functions are usually selected such that $N^k = 1$ at node k and $N_i^k = 0$ at all other nodes. This approximation of the displacement results in the classical equilibrium equation in finite elements as:

$$[K^e][u^e] = [F^e] \tag{2.27}$$

Equation 2.27 states that for each element, an element stiffness matrix, $[K^e]$ times the nodal displacements, $[u^e]$, is equal to an equivalent nodal forces vector, $[F^e]$. A static, implicit finite element method assembles all of the element stiffness matrices, $[K^e]$ into a global stiffness matrix, $[K]$. Similarly, the element equivalent nodal force vector, $[F^e]$ is assembled into a global nodal force vector $[F]$ which also contains concentrated nodal forces. The nodal displacements can then be calculated as follows:

$$[u] = [K]^{-1}[F] \tag{2.28}$$

After the nodal displacements are calculated, strain distribution can be calculated using the displacement as follows:

$$E_{ij} = \frac{1}{2}(\frac{\partial u_i}{\partial x_j} + \frac{\partial u_j}{\partial x_i}) \tag{2.29}$$

Where u_i is calculated using equation 2.26. After calculation of the distribution of strain, stress distribution can be calculated using the constitutive relation.

2.2 Dynamic, Implicit Analyses

In a dynamic finite element analysis, the equilibrium equation becomes:

$$\mathbf{M\ddot{u}} + \mathbf{I} - \mathbf{P} = \mathbf{0} \tag{2.30}$$

Where $\mathbf{M}$ is the mass matrix, $\mathbf{\ddot{u}}$ is the nodal acceleration, $\mathbf{I}$ is the internal force vector and $\mathbf{P}$ is the external force vector. An Implicit dynamic analysis refers to using an implicit integration scheme to solve Equation 2.30. An Implicit integration scheme solves for displacements (and their time derivatives) and time $t + \Delta t$ based on the information from time t and time $t + \Delta t$. This is significantly different from an Explicit integration scheme that only uses the information from time t to calculate the values at time $t + \Delta t$.

2.3 Dynamic, Explicit Analyses

Dynamic equilibrium can be written in the following manner:

$$\mathbf{M\ddot{u}} = \mathbf{P} - \mathbf{I} \tag{2.31}$$

Where $\mathbf{M}$ represents the material mass, $\mathbf{\ddot{u}}$ represents the second time derivative of displacement, $\mathbf{I}$ represents the inertial forces and $\mathbf{P}$ represents all other forces. This equation is general and applies to any mechanical system. Additionally, in the case of zero, or inertial forces, equation 2.31 represents static equilibrium.

What differentiates Explicit Dynamics from Implicit Dynamics is the method of solving equation 2.31. In an explicit analysis, a forward Euler or central difference integration scheme is used. This allows the unknown values to be calculated from known values. Because of this, an explicit analysis does not require iteration or convergence checking. However, time incrementation must be very small.

Equation 2.31 can be rearranged to directly sole for nodal acceleration at time n as shown in

equation 2.32:

$$\ddot{\mathbf{u}} = \mathbf{M}^{-1}(\mathbf{P} - \mathbf{I}) \tag{2.32}$$

After calculating the nodal accelerations, using simple forward difference integration, the nodal velocities can be calculated at time $n + \frac{1}{2}$ and nodal displacements at time $n + 1$. The efficiency of the Explicit integration algorithm comes through the use of Lumped Mass matrices. This refers to element mass matrices that are diagonal matrices. This makes inverting the mass matrix an computationally cheap calculation.

2.3.1 Stability and Time Incrementation

The solution of an explicit dynamics problem can be thought of as a wave propagation problem where unbalanced forces propagate between neighboring elements as stress waves. Because of this, a stable solution is only guaranteed when the time increment used in the forward-stepping integration scheme is less than the stable time increment. The stability limit can be calculated using equation 2.33:

$$\Delta t_{min} \leq \frac{2}{\omega_{max}}(\sqrt{1 + \xi^2} - \xi) \tag{2.33}$$

Where ω_{max} is the highest eigenvalue of the model and ξ is the fraction of critical damping in the highest mode. This is the exact equation for the stability limit for an explicit analysis. However, the value of this limit can be approximated as follows. The stable time increment can be related to dilation wave speed of the material. The dilation wave speed c_d of a material is defined as below:

$$c_d = \sqrt{\frac{E}{\rho}} \tag{2.34}$$

Where E is the Young's modulus of the material and ρ is the material mass-density. The stable time increment is related to the dilation wave speed through the following equation:

$$\Delta t = \frac{L^e}{c_d} \tag{2.35}$$

Equation 2.35 states that the stable time increment is directly proportional to L^e, the characteristic element length and c_d, the dilation wave speed. By substituting 2.34 into 2.35, we see the following relation between the stable time increment (Δt), Young's Modulus (E), the material density (ρ) and the characteristic element length (L^e):

$$\Delta t = \frac{L^e \sqrt{\rho}}{\sqrt{E}} \tag{2.36}$$

The consequences of Equation 2.36 are threefold:

1. Increasing the characteristic element length (mesh size) increases the stable time increment.
2. Increasing material density increases the stable time increment.
3. Decreasing material stiffness increases the stable time increment.

In Abaqus, the stable time increment is initially calculated by determining the stable time increment for each element across the model and using the smallest stable time increment. This step is repeated at the end of each time increment, and the new stability limit is enforced.

2.3.2 Energy Balance

As equilibrium is not guaranteed in a Dynamic Explicit analysis, examination of the balance of energies can be used to determine whether an Explicit analysis is producing accurate results. In Abaqus/Explicit, the energy balance is given by the following equation:

$$E_I + E_{VD} + E_{FD} + E_{KE} - E_W = E_{TOT} = CONST \tag{2.37}$$

Where E_I represents the internal energy of the model, E_{VD} represents the energy absorbed by viscous dissipation (bulk viscosity), E_{FD} represents the energy dissipated due to friction, E_{KE} represents the kinetic energy, E_W represents the work due to external forces and E_{TOT} represents the total energy of the system.

It is possible, and quite common, to model quasi-static problems with an explicit dynamic solver. While an explicit solver cannot enforce true static equilibrium, the goal of a quasi-static analysis is to ensure that inertial forces are very small in magnitude relative to other forces.

In a quasi-static analysis, kinetic energy should be a small fraction (around 5 to 10%) of the internal energy of the system. By ensuring that resulting kinetic energy of the model follows this guideline, static equilibrium is approximately satisfied.

3. METHODOLOGY

3.1 Model

This section presents all of the major components of the finite element model used to study the interaction between the human index finger and EVA glove pressure bladder and restraint layer. This will detail the finite element solver, the components of the model, material models, element selection, loads and boundary conditions, model outputs and the parametric study.

3.1.1 Finite Element Solver

Abaqus/CAE 6.14 was used for entirety of this research. Abaqus/CAE is a commercial finite element program that provides CAD, meshing and solving utilities. Abaqus also includes many element types, loads and boundary conditions, contact models, scripting capabilities and implicit and explicit analysis schemes. Abaqus' Dynamic, Explicit solver was used for this model. Due to the large displacements of the finger and glove combined with the post-buckling behavior of the glove and large contact analysis, an Explicit solver was chosen over an Implicit.

For the analyses performed in this thesis, an Dynamic,Explicit analysis was used. Explicit finite element analysis is an analysis scheme formulated originally for use in high energy impact analysis, however it is commonly used for quasi-static analyses with large deformation and large amounts of contact. In early model development for this research, an Implicit analysis was used. However, convergence issues were experienced with smaller-than-realistic deformations of the index finger. Therefore, it was determined that further development of the model would use an explicit analysis.

3.1.2 Parts of Model

The model is comprised of 3 main components: the index finger, the pressure bladder and the restraint layer. Figure 3.1 shows an overview of the parts of the model. The subsequent subsections will discuss in detail each part.

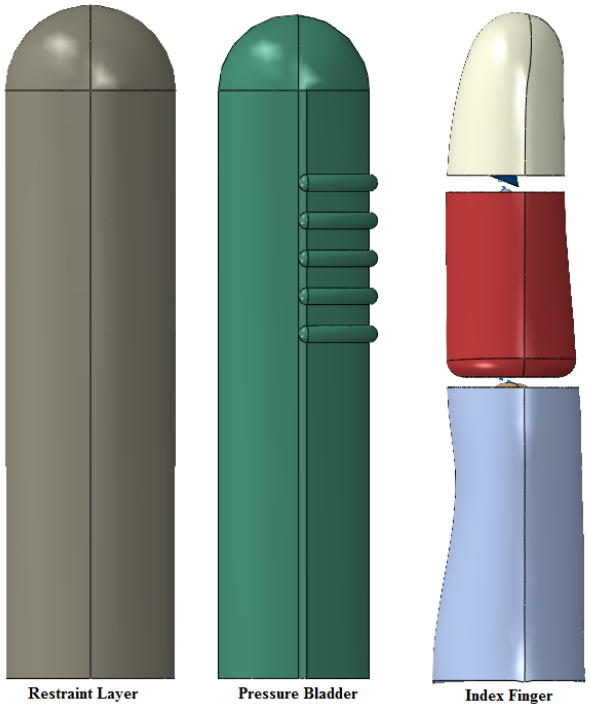

Figure 3.1: Overview of Parts of Model

3.1.2.1 Finger

The index finger was modeled using two idealizations. Both idealizations, the segmented idealization and full finger idealization, are simplified geometries of a notional index finger acquired from GrabCAD. The length of the index finger used was 80 mm, the author's finger length, which in this case correlated to a 75th percentile male hand by length when compared to the NASA STD-3001 [47]. For future glove development, NASA STD-3001 requires future EVA gloves and suits be designed to accommodate 1st percentile Asian Females to 99th percentile Caucasian males. However, for the purposes of this study, a single finger and glove were used. Both idealizations are comprised of flesh and bone. It was assumed that the stiffness of the bones were orders of magnitude greater than the flesh. To save computational time, the bones were modeled as rigid bodies. The three phalanges of the index finger are modeled: the proximal, medial and distal phalanges. Connectors are created between each bone to simulate the motion of the interphalangeal joints. Figure 3.2 illustrates the skeletal structure of the index finger.

Figure 3.2: Index Finger Skeletal Structure

Two idealizations of the bulk flesh were considered. The first idealization was continuous flesh of the finger. Figure 3.3 illustrates this idealization.

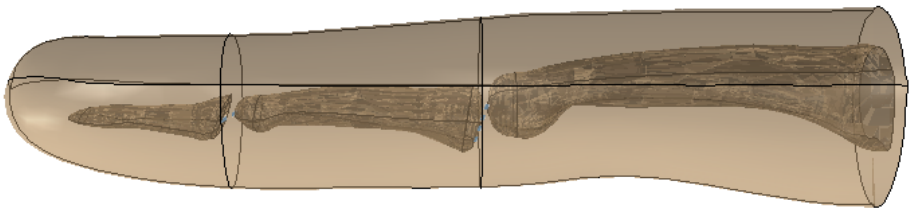

Figure 3.3: Full Finger Idealization

A second idealization of a "segmented" finger was also considered. In this idealization, the finger was segmented at each phalanx and the flesh was allowed to interpenetrate the other segments. Additionally, the proximal end of the medial segment was rounded slightly to prevent inter-penetration of the sharp edge into the pressure bladder of the glove during contact analysis. This idealization was considered to allow for further motions of the index finger. Details of this study are provided in Chapter 4. Figure 3.4 illustrates this idealization.

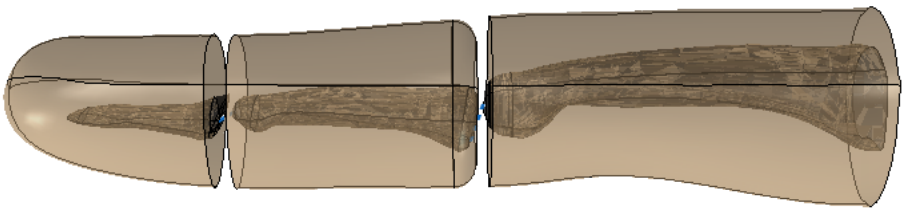

Figure 3.4: Segmented Finger Idealization

The bones were modeled using R3D4, Rigid, 3D 4-node shell elements. Both idealizations of the flesh were modeled using C3D10M elements, 10 node, second order tetrahedral elements with a modified integration formula. These are the recommended 3D continuum elements for an Explicit analysis using Abaqus. The results of these two idealizations are detailed in the results section.

The flesh was modeled as a linearly elastic, isotropic material with Young's modulus of 16.7 MPa and a Poisson's ratio of 0.4. While a linearly elastic material model is not the most realistic for flesh, it was assumed to be sufficient for the level of fidelity required for this model. As the mechanical response of the flesh of the finger was not of utmost interest, the computational expense, and lack of available literature on material properties of flesh surrounding human-phalanges, a linearly elastic model was deemed sufficient.

3.1.2.2 Pressure Bladder

The pressure bladder was modeled as a 3D shell part. The pressure bladder includes rolling convolutes on the dorsal surface representative of those in the real pressure bladder. Figure 3.5 shows the Abaqus model of the pressure bladder compared with a still-image of the Phase VI EVA glove index finger of the pressure bladder. While the comparison shows that the geometries are not exactly the same, they share the same features, namely the size and number of convolutes. Future work will seek to incorporate more realistic geometry of the pressure bladder.

Figure 3.5: Comparison of Pressure Bladder

An assumption that the pressure bladder finger was a right circular cylinder with constant radius was made to simplify part creation in Abaqus. While it is likely that the pressure bladder is manufactured with a non-constant cross-section to conform more closely to the individuals' finger, without information available in literature, a constant cross-section model was deemed sufficient. The tip of the pressure bladder was rounded to conform to the shape of the index finger. The most significant feature of the pressure bladder are the rolling convolutes. Again, while there is no available geometric data on the convolutes of the pressure bladder in the literature, the geometry of the convolutes in this model were modeled after available still images of the pressure bladder finger. Figure 3.6 shows an isometric view of the pressure bladder model and identifies the rolling convolutes.

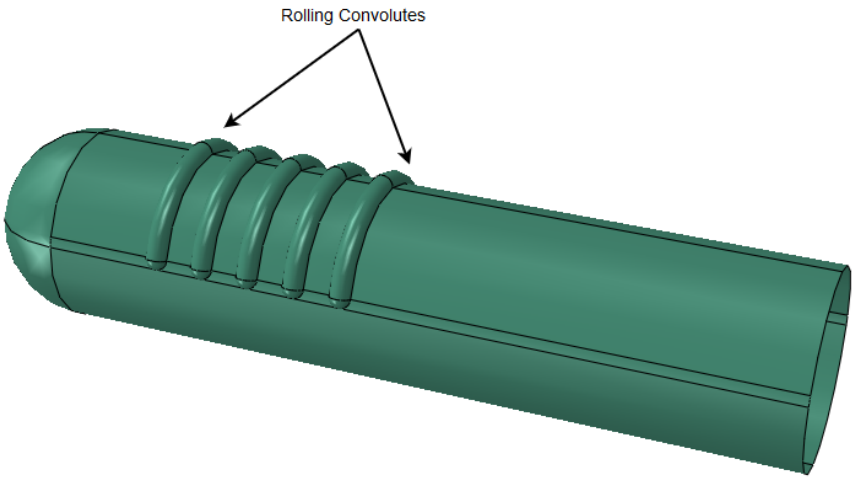

Figure 3.6: Rolling Convolutes in Pressure Bladder Model

Figure 3.7 shows a side view of the pressure bladder model and illustrates the geometric meaning of the convolute starting location. The convolute starting location is defined as the location of the first convolute with respect to the proximal end of the pressure bladder.

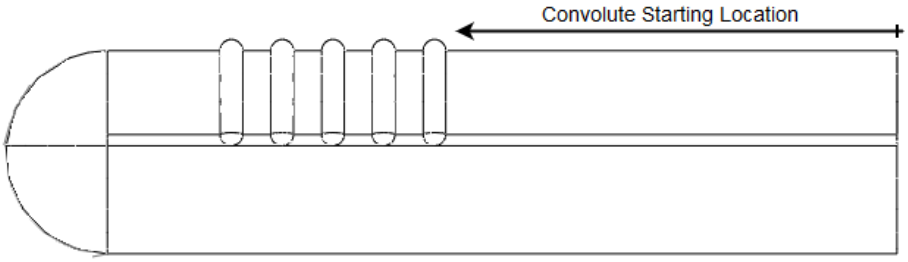

Figure 3.7: Convolute Starting Location

There are a total of 5 rolling convolutes on the dorsal surface of the pressure bladder. The convolutes are modeled as semi-circular arcs revolved around the longitudinal axis of the pressure bladder. The ends of the convolutes are tapered at their ends to smoothly attach to the remainder of the pressure bladder. Figure 3.8 illustrates the cross-sectional geometry of the convolute portion

of the pressure bladder.

Figure 3.8: Convolute Cross-Section Geometry

First order 4-node quadrilateral shell elements with reduced integration (element type S4R) were used to model the pressure bladder. First order elements were chosen over second order due to the use of a lumped mass-matrix in Abaqus/Explicit. When using first-order elements, the element mass matrix becomes a diagonal matrix and is easily inverted during the explicit integration scheme. This results in a significantly less computationally expensive model.

The pressure bladder material was modeled as a linearly elastic shell material. The linearly elastic model was chosen due to lack of availability of quantified results of the material response of the Rucothane used in the real pressure bladder. Because of this, the simplifying assumption of a linear material response was made. As the performance of the glove as a function of material properties of the bladder was of utmost interest, the Young's modulus and thickness of the pressure bladder were varied through a parametric study detailed in subsequent sections. While it is likely that a membrane material (where the material has no out-of-plane stiffness) would have been sufficient for modeling the thin pressure bladder, a shell section was ultimately selected to prevent any under-estimation of glove stiffness that could occur by neglecting the out-of-plane stiffness. The trade off is that shells are computationally more expensive than membrane sections. The computational cost penalty was deemed necessary for this model.

3.1.2.3 Restraint Layer

The restraint layer is modeled as a 3D shell part. The geometry of the restraint layer is assumed to be a right circular cylinder of constant diameter with a domed end-cap. Like the pressure bladder, this simplifying assumption was made to allow for easily varying the size of the part as well as lack

of available information about the true geometry of the Phase VI restraint layer. As a first-order approximation of the restraint layer, the geometry was simplified and the sizing adjustment cords were not modeled. Figure 3.9 shows the restraint layer geometry in Abaqus.

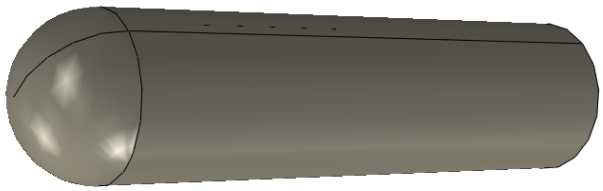

Figure 3.9: Restraint Layer Geometry

First order 4-node quadrilateral shell elements were used to model the restraint layer. Like the pressure bladder, first order shell elements were selected due the Lumped mass-matrix characteristics of first order shell elements.

The restraint material was modeled as a linearly elastic shell material. The linearly elastic model was chosen due to lack of availability of quantified results of the material response of the textile used in the real pressure bladder. Because of this, the simplifying assumption of a linear material response was made. Additionally, a simplifying assumption of homogenization and isotropy was made. While it is possible that the material used in the Phase VI glove restraint layer is heterogeneous and anisotropic, due to lack of available information about that material, an isotropic and homogeneous material model were used. As the performance of the glove as a function of material properties of the restraint layer was of utmost interest, the Young's modulus and thickness of the restraint layer were varied through the parametric study detailed in subsequent sections.

3.1.3 Contact Model

A frictionless, contact model was used to model the contact interaction between the finger and glove. Figure 3.10 shows the behavior of this contact relationship in Abaqus. While two parts are not in contact, there is no contact pressure. Contact pressure does not occur until the parts come

into contact (have zero clearance), from there the contact pressure is calculated with any level of pressure possible. This results in a behavior where surfaces separate if the contact pressure reduces to zero, and when the clearance reduces to zero, the contact pressure becomes non-zero. This is the default contact algorithm for Abaqus, Explicit.

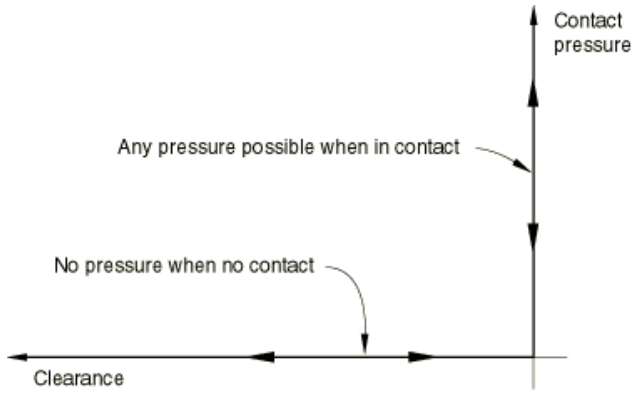

Figure 3.10: Hard Contact Pressure-Overclosure Diagram

A frictionless contact model was chosen due to the large unknowns about material properties of the actual glove. It was assumed that friction would not be a dominant force in the contact between the finger and pressure bladder. Contact was considered in a pair-wise approach, where pairs of parts that were allowed to contact with each other were manually specified. Table 3.1 shows a summary of each part and the respective pairs considered in the contact analysis. Self refers to the ability for a contact analysis to be performed on a part contacting itself.

Part	**Contact Pair**
Finger	Pressure Bladder
Pressure Bladder	Finger, Self, Restraint Layer
Restraint Layer	Self, Pressure Bladder

Table 3.1: Summary of Contact Pairs

3.1.4 Analysis Steps

The analysis was broken up into 3 distinct steps to model the interaction between the index finger and glove during bending:

Analysis Step	Purpose
Over-Pressurization	To deform the glove finger to eliminate initial inter-penetration of the finger.
Pressure Reduction	To reduce the glove pressure to nominal value.
Bending	To perform the bending and contact analysis.

Table 3.2: Analysis Steps

Figure 3.11 shows the assembly in Abaqus and the global coordinate system. This coordinate system will be referenced when displacement-type boundary conditions are discussed.

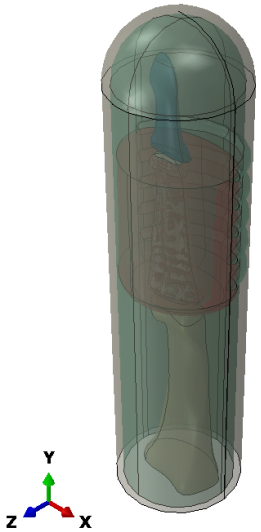

Figure 3.11: Global Coordinate System in Abaqus Assembly

Figure 3.12 shows the time history of the amplitude of the internal pressure of the glove.

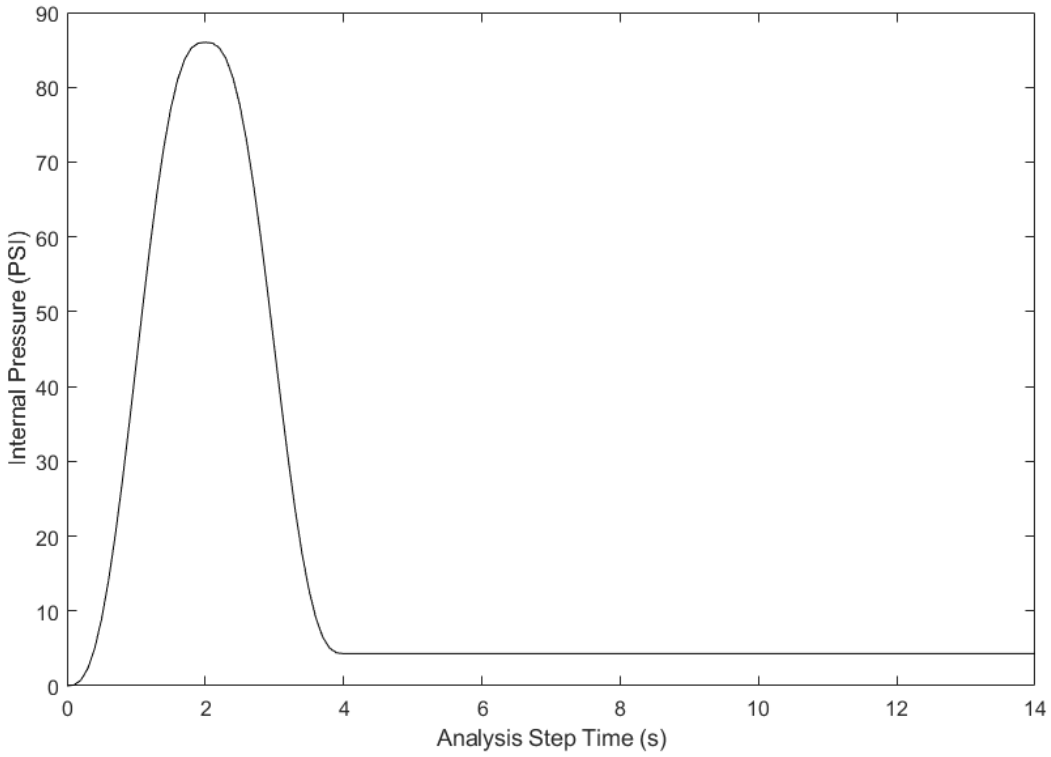

Figure 3.12: Time History of pressure amplitude

3.1.4.1 Over-Pressurization

Initially, the index finger starts inside of the glove but is allowed to interpenetrate the pressure bladder and restraint layer. This is to allow for undersizing of the glove finger. The first step is over-pressurization of the pressure bladder. Here, an artificially high internal pressure is applied to the pressure bladder to cause large "ballooning" of the glove-finger. The purpose of this step is to eliminate any interpenetration of the finger into the glove. In this step, contact between the finger and glove is ignored.

In this step, the finger is constrained from moving. Additionally, the bottom of the pressure bladder and restraint layer are constrained from moving vertically, but allowed to move in the X-Z plane. In this step, a uniformly distributed pressure load is applied to the inside of the pressure bladder. The magnitude of the pressure load is ramped using a smooth step amplitude function to

a value 50x greater than the nominal glove pressure.

3.1.4.2 Pressure Reduction

Next, the pressure is reduced to the nominal pressure. The purpose of this step is to end with the finger fit inside of the glove with the correct internal pressure of the glove. During this step, contact between the pressure bladder-finger, and pressure bladder-restraint layer were modeled.

In this step, the finger is constrained from moving and the same constraint of X-Z motion of the bottom of the pressure bladder and restraint layer were applied. In this step, the internal pressure of the pressure bladder was reduced using a smooth-step amplitude function from the over-pressurized value to the nominal value.

3.1.4.3 Bending

The bending step of the analysis is the most important. The purpose of the previous two steps is to set-up the model for the bending analysis. In this step, the index finger is bent, and the contact analysis between the finger and glove is performed.

In this step, the lower portion of the pressure bladder and restraint layer are clamped. Additionally, the proximal edge of the finger is clamped. The internal pressure of the glove remains constant throughout this step. The PIP joint is rotated 1.9 radians using a smooth-step amplitude function. The DIP joint is rotated 0.85 radians using a smooth-step amplitude function. Throughout the duration of the bending step, a 2:1 ratio of PIP rotation to DIP rotation is maintained. Figure 3.13 illustrates the kinematics of the index finger.

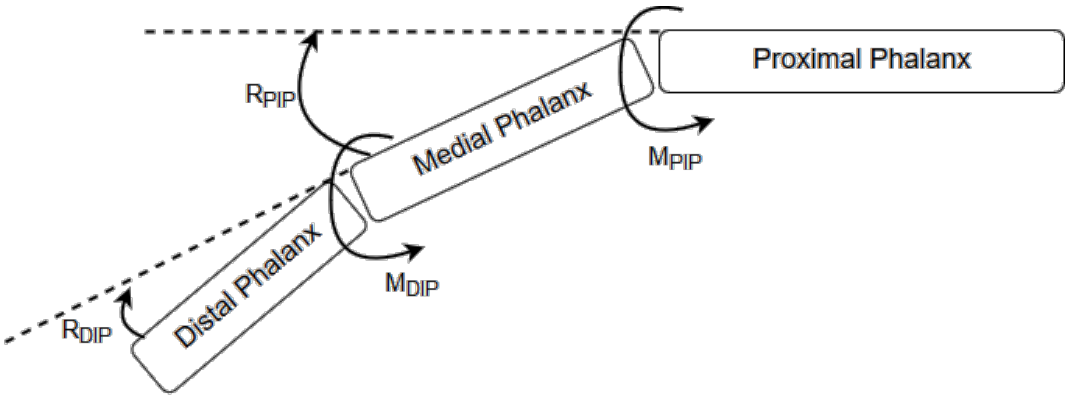

Figure 3.13: R_{DIP} and R_{PIP} Kinematics of Index Finger

Figure 3.14 illustrates the clamped boundary condition for the flesh, proximal phalanx, pressure bladder and restraint layer for the bending step.

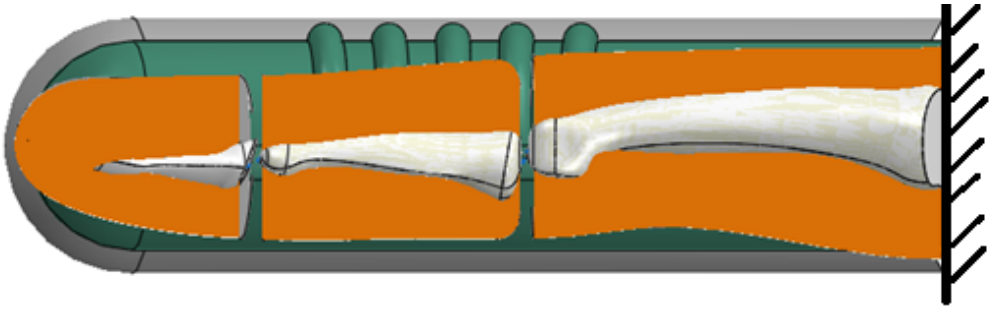

Figure 3.14: Boundary Conditions for Bending Step

Figure 3.15 shows the deformed configuration at each step of the analysis. Here, one can clearly see the interpenetration of the finger into the pressure bladder at the initial step. After over-pressurization, all interpenetrations are gone and after pressure reduction, the glove is at it's nominal state after pressurization. In this state, one can see that the convolutes have expanded quite a bit as the pressure bladder is shorter in length than the restraint layer. However, the convolutes are not entirely flat at this stage and will act to reduce the resistance the glove provides during bending. Finally, one can see the bent configuration of the finger and glove.

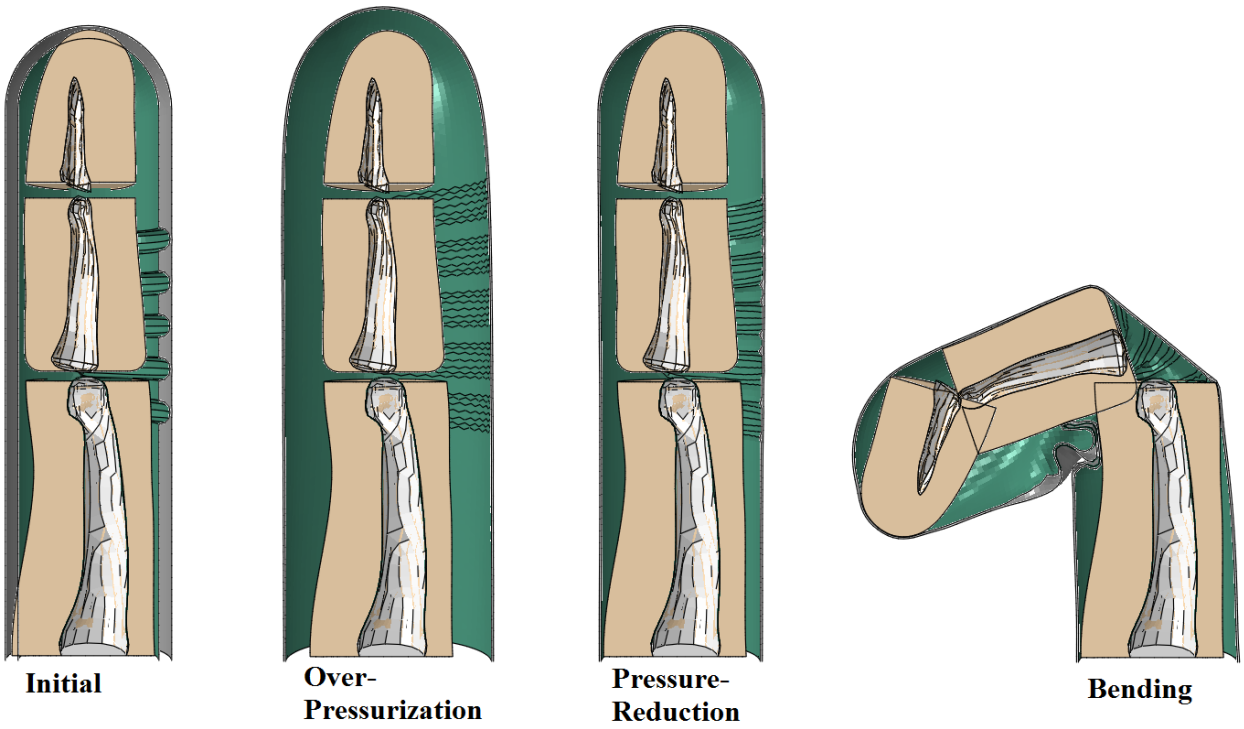

Figure 3.15: Deformed Configuration at Each Step

3.1.5 Model Outputs

The primary model outputs are displacement, stress and strain in the finger, pressure bladder and restraint layer. Additionally, contact pressure on the index finger is output. The model also outputs the total resultant force due to contact with the glove on the dorsal and palmar surfaces of the distal phalange segment and medial phalange segment as well as the line of actions of those forces. The output quantities are used to calculate the joint torque caused by contact with the glove about the PIP and DIP joints. Figure 3.16 shows the output quantities used to calculate the resulting joint torque due to contact with the glove.

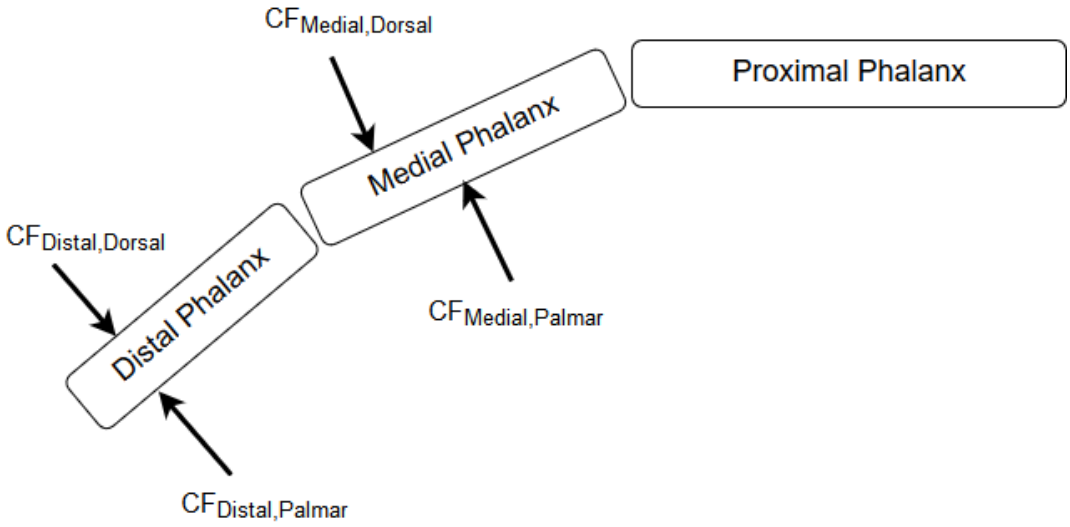

Figure 3.16: Output Variables used to calculate joint torque due to contact

Due to the behavior of Abaqus, the finger model is split into 4 contact surfaces surfaces to allow for the output of the magnitude, direction and line of action of the contact force due to the glove on the dorsal and palmar surfaces of the distal and medial phalanges.

The primary model outputs are the torques about the DIP and PIP joints due to contact with the glove. These are the measures of the resistance the glove provides to the finger. These joint torques can be calculated using equations 3.1 and 3.2. Where Y_{DIP}, Z_{DIP}, Y_{PIP} and Z_{PIP} refer to the Y and Z coordinates of the DIP and PIP joints respectively. For the force terms, the first subscript denotes the Y or Z component and the second subscript denotes the contact surface where DD denotes the dorsal distal surface, PD denotes the palmar distal surface, DM denotes the dorsal medial surface and PM denotes the palmar medial surface. the Z and Y terms with those subscripts indicate the line-of-action of the contact force acting upon that surface.

$$\begin{aligned} M_{DIP} = F_{Y,DD}(Z_{DIP} - Z_{DD}) + F_{Z,DD}(Y_{DIP} - Y_{DD}) \\ + F_{Y,PD}(Z_{DIP} - Z_{PD}) + F_{Z,PD}(Y_{DIP} - Z_{PD}) \end{aligned} \tag{3.1}$$

$$
\begin{aligned}
M_{PIP} = F_{Y,DD}(Z_{PIP} - Z_{DD}) + F_{Z,DD}(Y_{PIP} - Y_{DD}) \\
+F_{Y,PD}(Z_{PIP} - Z_{PD}) + F_{Z,PD}(Y_{PIP} - Z_{PD}) \\
+F_{Y,DP}(Z_{PIP} - Z_{DP}) + F_{Z,DP}(Y_{PIP} - Y_{DP}) \\
+F_{Y,PP}(Z_{PIP} - Z_{PP}) + F_{Z,PP}(Y_{PIP} - Z_{PP})
\end{aligned}
\tag{3.2}
$$

Additional model outputs of model internal energy and model kinetic energy are used for validation purposes.

3.2 Mass Scaling Study

Because an Explicit, Quasi-static analysis was used for this model, it is important to understand how mass scaling effect the model output as well as computational expense. To do this, the assembly-level mass-scaling was applied to the entire model. This artificially scales the density of all materials in the analysis. The purpose of this study was to find the highest amount of mass scaling (to reduce runtime) while not adversely affecting model output. For this study, the model was run first with a very large amount of mass scaling (500). After determining whether this mass scaling factor produced valid quasi-static results, the mass scaling factor was decreased until a valid level was achieved. After a valid level of mass-scaling was determined, this value was used for the remainder of the analyses.

3.3 Mesh Refinement Study

A mesh refinement study was performed on all components of the model except for the skeletal structure. As the skeletal structure was modeled as rigid bodies and the internal stresses of the finger were not considered in this model, it was deemed unnecessary to perform a mass scaling study on the skeletal structure of the finger. This study was broken into two parts. The first part studies the effect of mesh refinement of the index finger on the resulting joint torques. Three levels of mesh refinement were considered for the finger. After this study was performed, three levels of mesh refinement on the pressure bladder and restraint layer were considered with the mesh refinement of the index finger held constant. The following table details the average size of elements for the pressure bladder and restraint for each level of mesh refinement.

	Average Element Side Length [mm]	
Mesh Refinement Level	***Pressure Bladder***	***Restraint Layer***
Coarse	0.5	0.75
Medium	0.25	0.5
Fine	0.175	0.35

Table 3.3: Summary of Mesh Refinement Study

Figure 3.17 shows the pressure bladder and restraint layer meshes for each level of mesh refinement. As the geometry of the restraint layer is much simpler than the pressure bladder, a coarser mesh was used on the restraint layer across all cases.

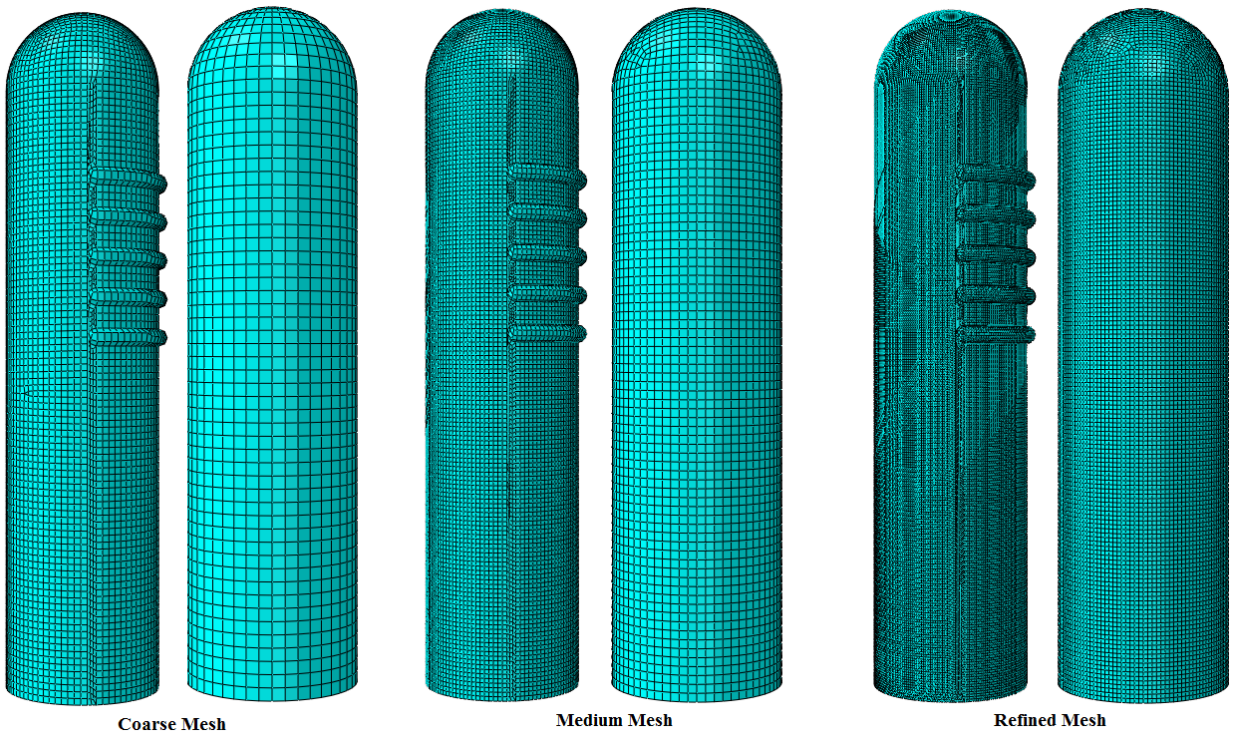

Figure 3.17: Mesh Refinement Levels for Pressure Bladder and Restraint Layer

After the a convergence study on the mesh refinement was performed, the coarsest mesh that exhibited convergence was used for the remainder of the analyses. Details of these results are given in Section 4.

3.4 Scripting Model Creation

In order to easily perform the parametric study, Python was used to script portions of the model creation. Through Abaqus' 6.14 Python environment, a script was created to read in a a default design configuration. The script was then used to vary the design variables and create analysis input files for each case in the parametric study.

3.5 High-Performance Computing

All of the analyses were run on Texas A&M's High-Performance Research Computing's (HPRC) Ada supercomputer. An x86 Linux build of Abaqus 6.14 was used to run the Abaqus models. The Ada supercomputer is a x86-64 Linux machine with a total of 852 compute nodes with a total of 17,340 processing cores. The majority of the compute nodes have 64 GB of memory at a clock speed of 1866 MHz. Each compute node houses 2 sockets with Intel Xeon E5-2670 processors, each with 10 cores running at a clock speed of 2.5 GHz.

Abaqus/6.14 installed on the Ada cluster is what is used to run all analyses used in this research.

The model was run with domain-level parallelization. This means that regions of the assembly are split into discrete domains and distributed equally among computational cores. An MPI-based multiprocessing mode was used. The model was split into 20 domains for all analyses. Figure 3.18 shows how the model is split into each of the 20 domains.

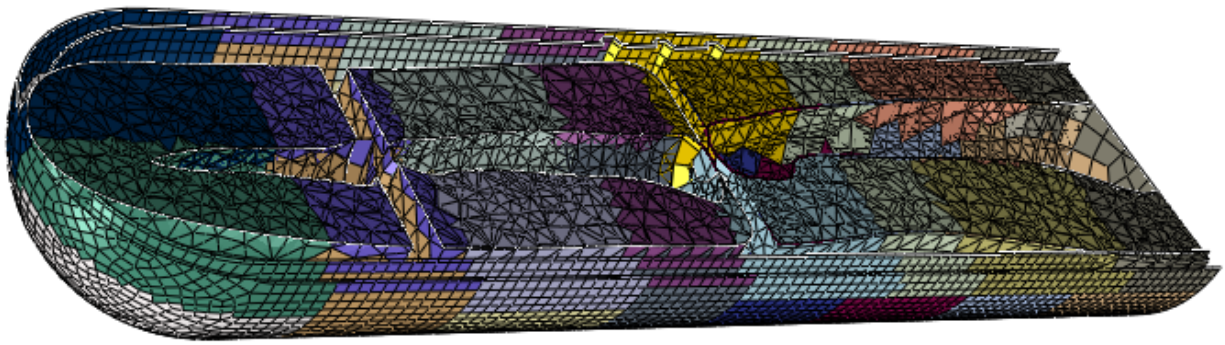

Figure 3.18: Domain Discretization for Parallelization

3.6 Investigation of Contributions to Glove Resistance

In order to determine how much glove pressure, material stiffness and bunching contribute to the overall resistance provided by the EVA glove finger, for a given glove design (material properties and geometry), an analysis was run with both nominal internal pressure and no pressure. A comparison between nominal glove resistance, glove resistance with no pressure and the amount of resistance caused by the contact of the finger with the bunched area of the glove will provide valuable insight into the contributing factors of glove resistance.

For any given design, the glove resistance contribution due to bunching was calculated as the joint torque about the PIP joint due to contact with the glove in the Palmar surface of the Medial Segment as shown in Equation 3.3.

$$M_{PIP,Bunch} = F_{Y,PP}(Z_{PIP} - Z_{PP}) + F_{Z,PP}(Y_{PIP} - Z_{PP}) \tag{3.3}$$

This calculation assumes that the contact force on the palmar surface of the medial finger segment is solely due to the bunched area of the glove. For this model, this is a valid approximation as illustrated in Figure 3.19:

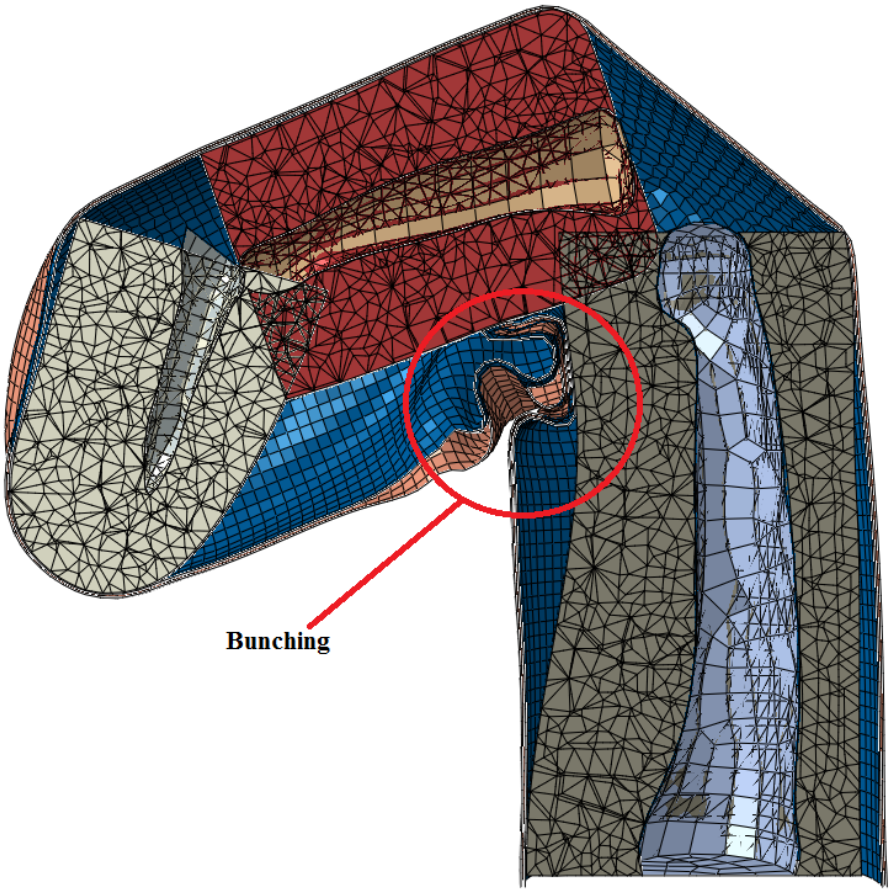

Figure 3.19: Glove Bunching Location in Finite Element Model

The glove resistance contribution due to material stiffness was determined by running an analysis with 0 PSI of internal pressure of the glove. Then, the resistance contribution due to material stiffness was calculated by subtracting the bunching contribution from the entire glove resistance. Equation 3.4 details this calculation.

$$\begin{aligned} M_{PIP,Material} = {} & F_{Y,DD}(Z_{PIP} - Z_{DD}) + F_{Z,DD}(Y_{PIP} - Y_{DD}) \\ & + F_{Y,PD}(Z_{PIP} - Z_{PD}) + F_{Z,PD}(Y_{PIP} - Z_{PD}) \\ & + F_{Y,DP}(Z_{PIP} - Z_{DP}) + F_{Z,DP}(Y_{PIP} - Y_{DP}) \end{aligned} \tag{3.4}$$

Finally, the resistance contribution due to the internal pressure of the glove was determined by comparing the resulting glove resistance for the 0 PSI case and the 4.3 PSI case. The difference

between these two cases is determined to be the contribution due to the presence of a nominal internal pressure of the glove.

3.7 Parametric Study

A parametric study investigating the effects of glove design parameters on joint torque was performed over a total of 8 design variables. A full-factorial 2-level parametric study was performed with the levels of each design variable shown in Table 3.4. The model was run for each combination of design variables, and joint torque due to glove contact about the PIP and DIP joints was recorded.

Design Variable	**Level 1**	**Level 2**
Pressure Bladder Thickness	0.15 mm	0.3 mm
Restraint Layer Thickness	0.3 mm	0.45 mm
Pressure Bladder Young's Modulus	6.5 MPa	13 MPa
Restraint Layer Young's Modulus	100 MPa	200 MPa
Convolute Starting Location	30 mm	40 mm
Number of Convolutes	3	5
Convolute Radius	1.5 mm	3.0 mm
Glove Internal Pressure	4.3 PSI	8.6 PSI

Table 3.4: Summary of Parametric Study

After running the parametric study, the main effects of each design variable were determined by calculating the average joint torques for both levels of each design variable averaged across all cases. While this is a standard statistical technique, there is a significant limitation in that the average effects do not provide any insight into the behavior of outliers. It is possible that a design variable will show minimal effect on average, but can have large effect for specific designs. Due to this, care should be taken in interpreting the results of a parametric study.

4. RESULTS AND DISCUSSION

This section will provide results for the mass-scaling study, mesh refinement study, investigation into the dominant contributing factors of the resistance provided by the glove and parametric study results.

4.1 Analysis Strategy

Before studying the interaction between the index finger and EVA glove, it is necessary understand the behavior and validity of the analysis strategy. This section will present the results of the mass scaling study (and the validity of the quasi-static solution), the effects of each finger idealization on the model, the results from the mesh refinement study on the finger, bladder and restraint layer as well as a comparison between the model output and existing experimental data.

4.1.1 Calibration of Explicit Quasi-Static Solver

The results for this section show the behavior of using Abaqus' explicit solver to model the finger-glove interaction as a quasi-static problem. Figure 4.1 shows the normalized CPU time versus mass-scaling factor. The CPU times are normalized by the longest CPU time and the values range from 1 to 0.25.

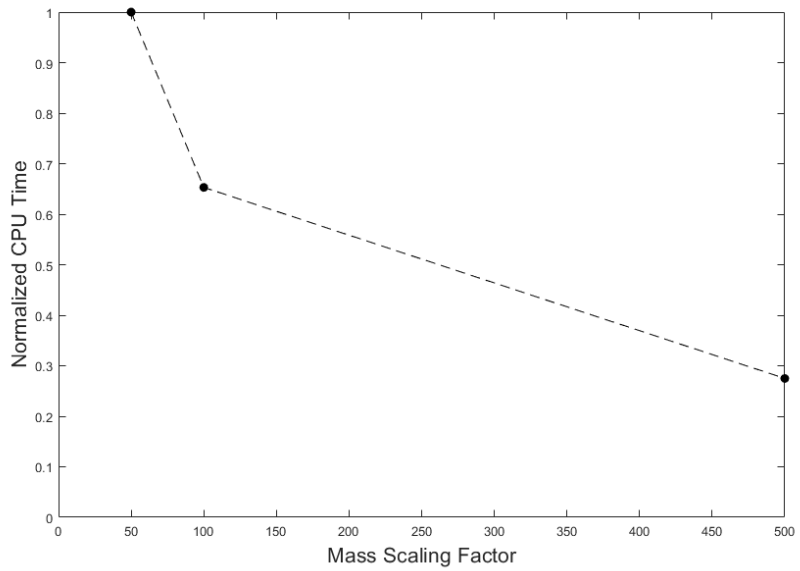

Figure 4.1: Normalized CPU Time for Various Mass Scaling Factors

As expected, as the mass-scaling factor is increased, the computational time decreases. As a shorter run-time is desirable (in order to facilitate more analysis runs), the largest mass-scaling factor that produces accurate results is ideal. However, Figure 4.1 does not provide any information about the validity of the solutions for each mass-scaling level.

Figures 4.2 and 4.3 show the M_{DIP} as a function of R_{DIP} and M_{PIP} as a function of R_{PIP} for various mass scaling factors respectively. Both joint torques show similar trends: larger mass-scaling factors lead to larger fluctuation in the resulting joint torque.

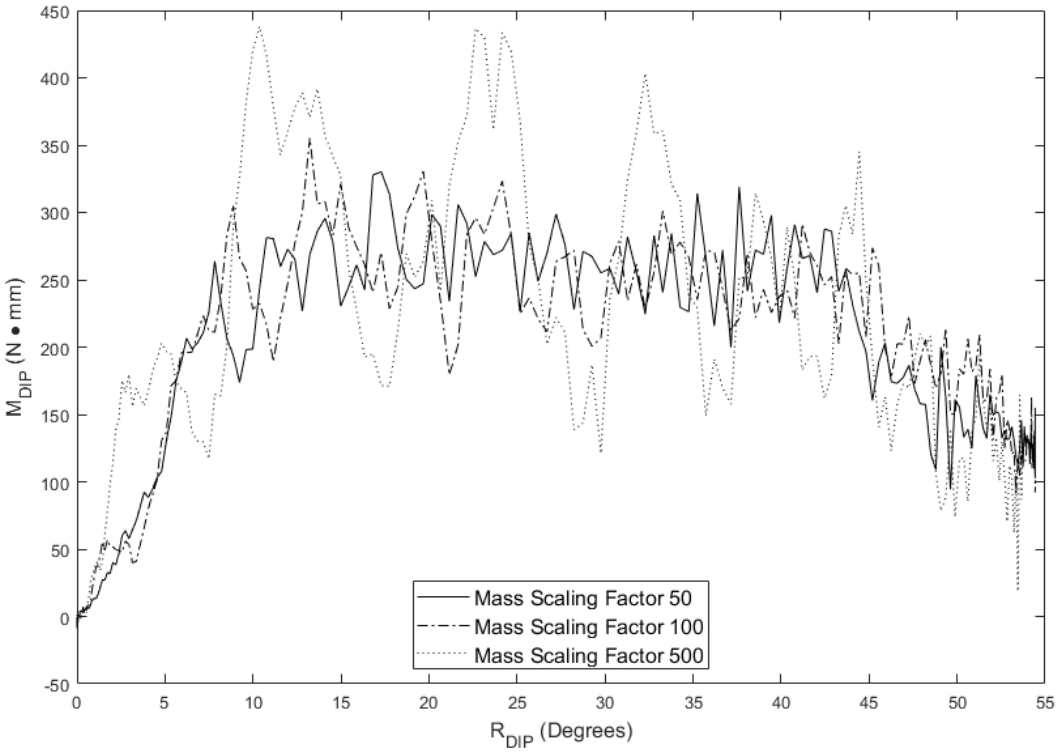

Figure 4.2: M_{DIP} vs. R_{DIP} for Various Mass Scaling Factors

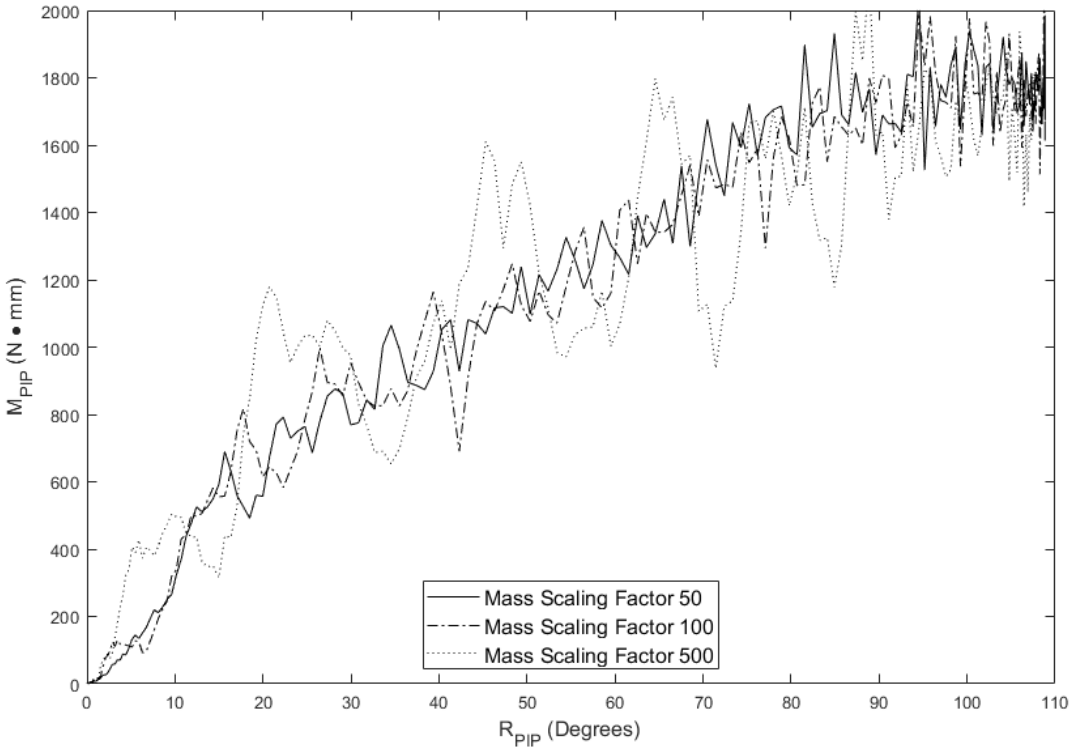

Figure 4.3: M_{PIP} vs. R_{PIP} for Various Mass Scaling Factors

While there is no significant difference in a moving average of the joint torque for each mass-scaling factor, the presence and amplitude of the noise is quite significant. Already, this leads one to rule out the use of a mass-scaling factor of 500 for this analysis. While the reduction in computational cost for using a mass-scaling factor this large is desirable, the large amount of fluctuation in the joint torques lead one to question the validity of this solution.

As static equilibrium is not automatically satisfied in a quasi-static analysis when using an explicit finite element solver, it is important to compare the kinetic energy with respect to the internal energy of the model. It is well documented that the ratio of Kinetic Energy to Internal Energy should be less than 0.1 for valid quasi-static results. Figure 4.4 shows the time history of this ratio during the analysis for each level of mass-scaling. It should be noted that the area of interest is from Analysis Step Time 4s to 14s (during the bending step). an acceptable quasi-static

result.

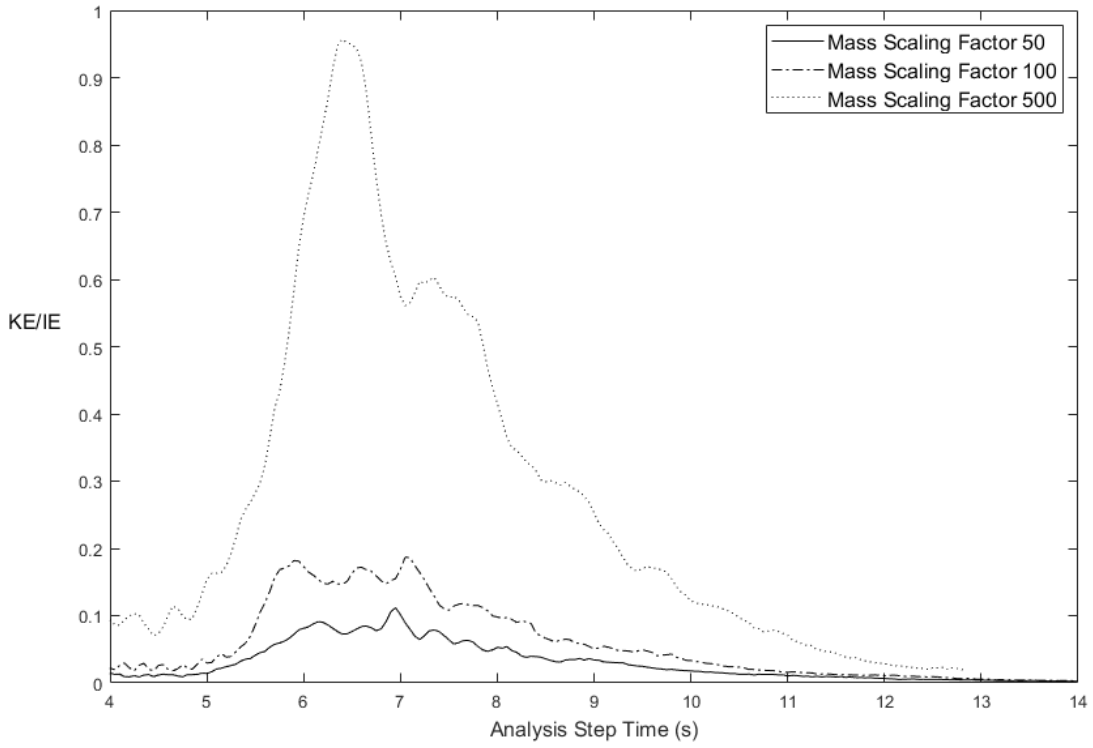

Figure 4.4: $\frac{KE}{IE}$ Time Histories of Mass Scaling

For a mass scaling factor of 500, one can see that for the majority of the step, the kinetic energy is significant relative to the internal energy of the model. This ratio is much higher than the threshold for a valid quasi-static analysis. For a mass scaling factor of 100, it is clear that the ratio of kinetic energy to internal energy is much less than the previous factor. However, during the majority of the step, the ratio of KE to IE is still larger than the 0.1 threshold for a valid quasi-static analysis. The time history of the ratio of KE to IE for a mass-scaling factor of 50 shows that this mass scaling factor yields an energy ratio that falls below this threshold.

One can directly correlate the presence (and amplitude) of noise in the joint torque data with the energy ratios. As the ratio of Kinetic Energy to Internal Energy increases, inertial terms become

significant in the analysis. This is undesirable for a quasi-static analysis. This inertial dominance leads to unrealistic motions in the model, leading to significant fluctuations in contact pressure and the resultant joint torque. At the same time, it is desirable to minimize the CPU time of the model. Because of this, the largest mass-scaling factor that admits a permissible quasi-static solution will be used for the remainder of this thesis. A mass-scaling factor of 50 fits this criteria and will be used for the remainder of this analysis.

4.1.2 Effect of Finger Idealization on Joint Torques

As two idealizations of the bulk-flesh of the finger were considered (full and segmented idealizations), it was necessary to determine which idealization was ideal for this study. Figure 4.5 shows the deformed configuration for both the full finger idealization and segmented finger idealization at the same level of rotation. The left of the figure illustrates the deformed configuration of the full finger idealization. The right of the figure illustrates the deformed configuration of the segmented finger idealization. It should be noted that qualitatively, the response of the pressure bladder and restraint layer is quite similar between the two idealizations. Wrinkling of the glove has occurred in both idealizations, with a similar wrinkling mode and location in both (near the PIP joint). Additionally, the primary areas of the finger in contact with the glove are the finger pad as well as the dorsal surface of the proximal segment of the finger. This figure illustrates the similar response in the buckling of the glove for both idealizations.

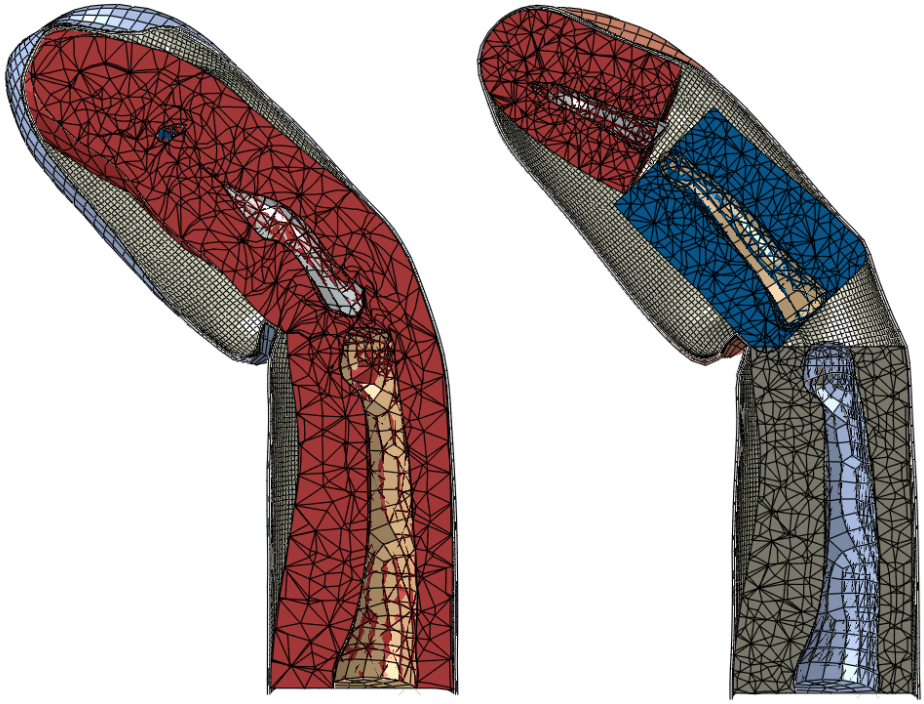

Figure 4.5: Finger Deformation Comparison

While Figure 4.5 illustrates the maximum amount of bending achieved by the full finger idealization, Figure 4.6 illustrates the maximum amount of bending achieved with the segmented finger idealization. One can clearly see that the segmented finger idealization is able to achieve more realistic ranges of motion of the finger.

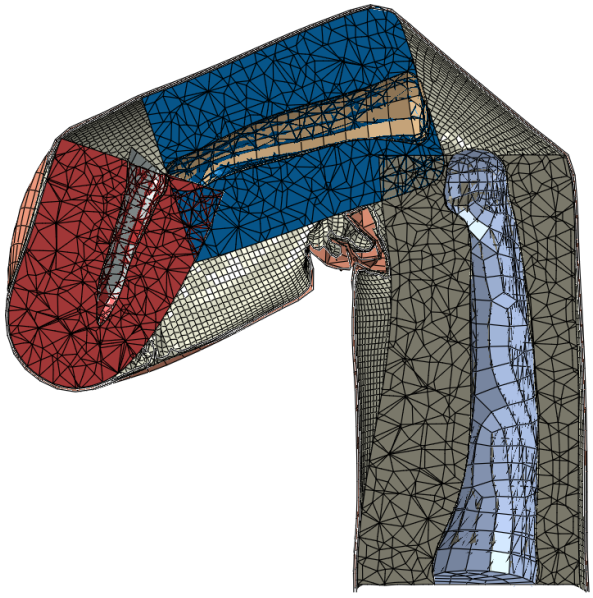

Figure 4.6: Full Deformation of Segmented Finger Idealization

The analysis terminates prematurely for the full-finger idealization due to excessive element deformation. While the segmented finger idealization achieves approximately 110 degrees of rotation on the PIP joint, the full finger idealization terminates prematurely at approximately 45 degrees of rotation of the PIP joint. This premature termination occurs due to excessive distortion of the elements in the flesh between the medial and proximal phalanges. (shown in Figure 4.7).

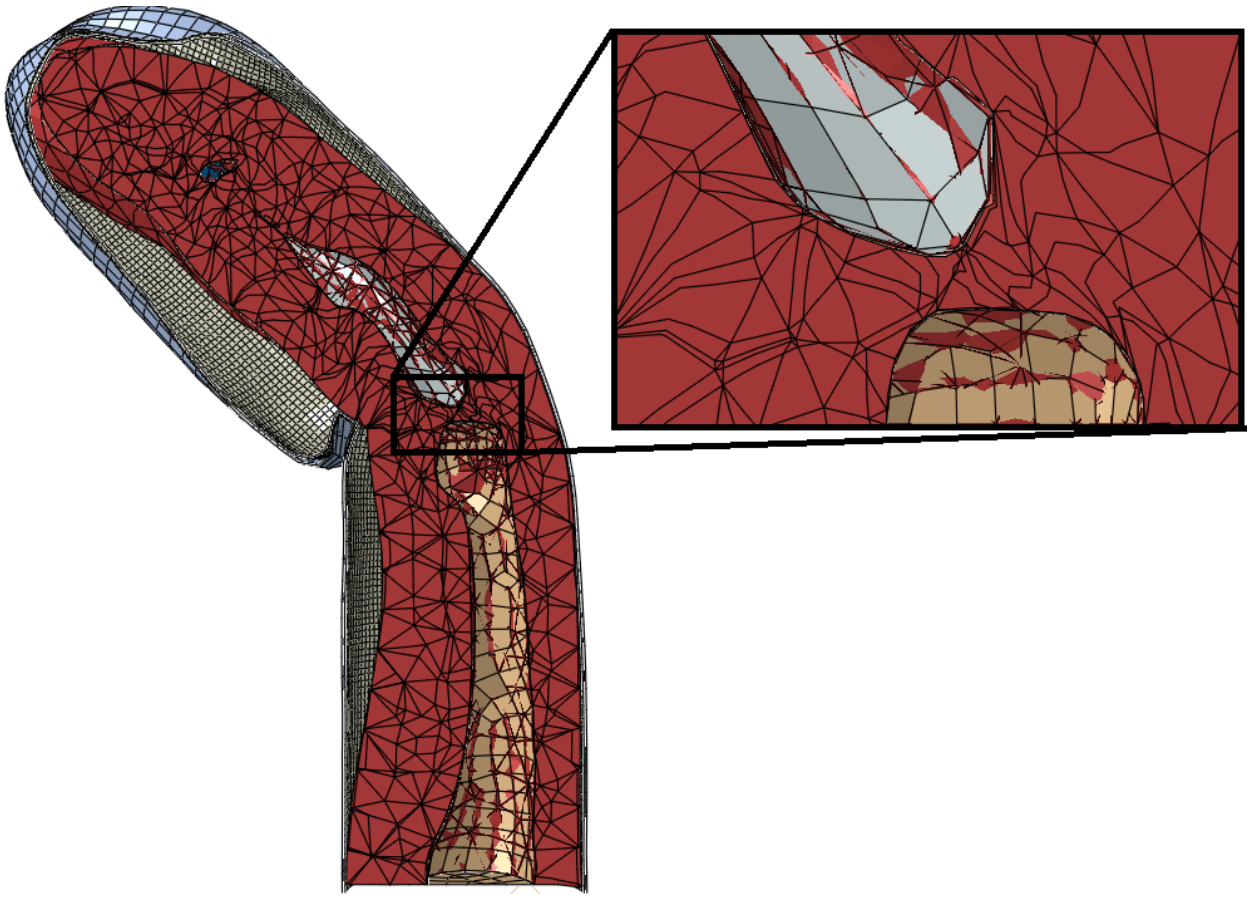

Figure 4.7: Element Distortion in Full Finger Idealization

The excessive distortion of these elements causes the analysis to terminate prematurely. However, Abaqus does include an adaptive re-meshing utility that can allow the analysis to re-mesh portions of the model during analysis. This could be used to eliminate the issues of element distortion in the full finger idealization. The use of adaptive re-meshing could enable the use of the full-finger idealization to achieve full motion of the finger. However, this is left as future work.

Figures 4.8 show the joint torques for both the full finger and segmented finger idealizations for joint torque about the DIP joint. For joint torque about the PIP joint, the full-finger idealization predicts a joint torque approximately 30% less than the segmented finger idealization at a rotation of 45 degrees. It is unclear why this is the case as the joint torques do not account for the mechanical response of the flesh.

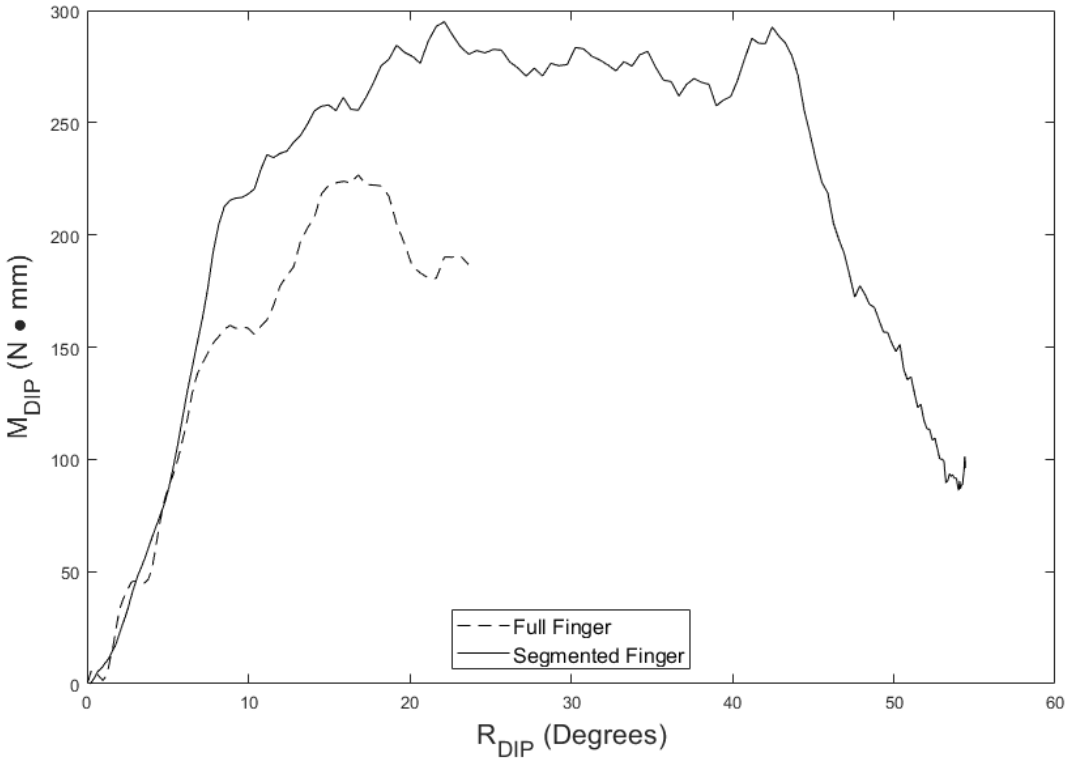

Figure 4.8: M_{DIP} Comparison for Full and Segmented Finger Idealizations

Figure 4.9 shows the joint torque comparison for both the full finger and segmented finger idealizations for joint torque about the PIP joint. For joint torque about the PIP joint, the full-finger idealization predicts a joint torque approximately 40% less than the segmented finger idealization at a rotation of 45 degrees.

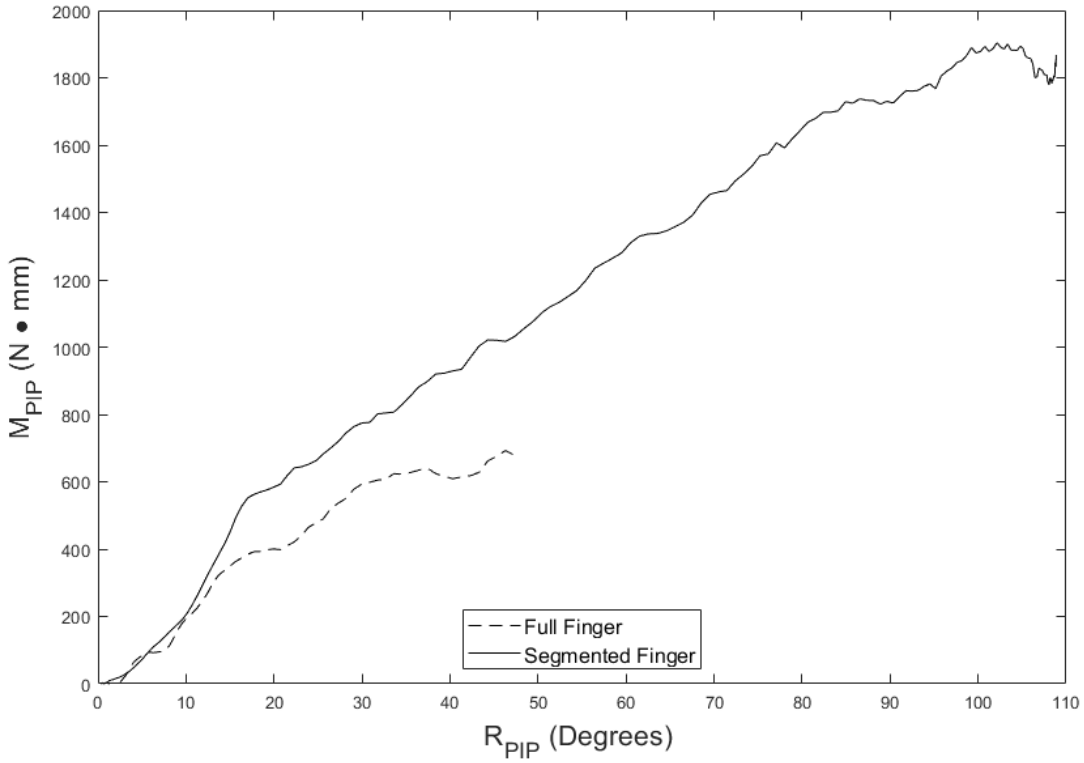

Figure 4.9: M_{PIP} Comparison for Full and Segmented Finger Idealizations

There are clearly some differences in the magnitude of joint torques calculated for each finger idealization, but the joint torques follow similar trends. However, as the goal of this model is to quantify sensitivity of glove resistance to glove design parameters, comparative analyses will be performed. Therefore, the differences in joint torque magnitude for the different finger idealizations are not of utmost concern. The ability to deform the index finger to realistic motions was necessary for this study. Because of this requirement, analysis proceeded with the segmented finger idealization.

4.1.3 Mesh Refinement Study

Three levels of mesh refinement of the segmented flesh idealization were run with all other parameters held constant. Figure 4.10 shows the surface meshes for each level of mesh refinement of the segmented finger idealization.

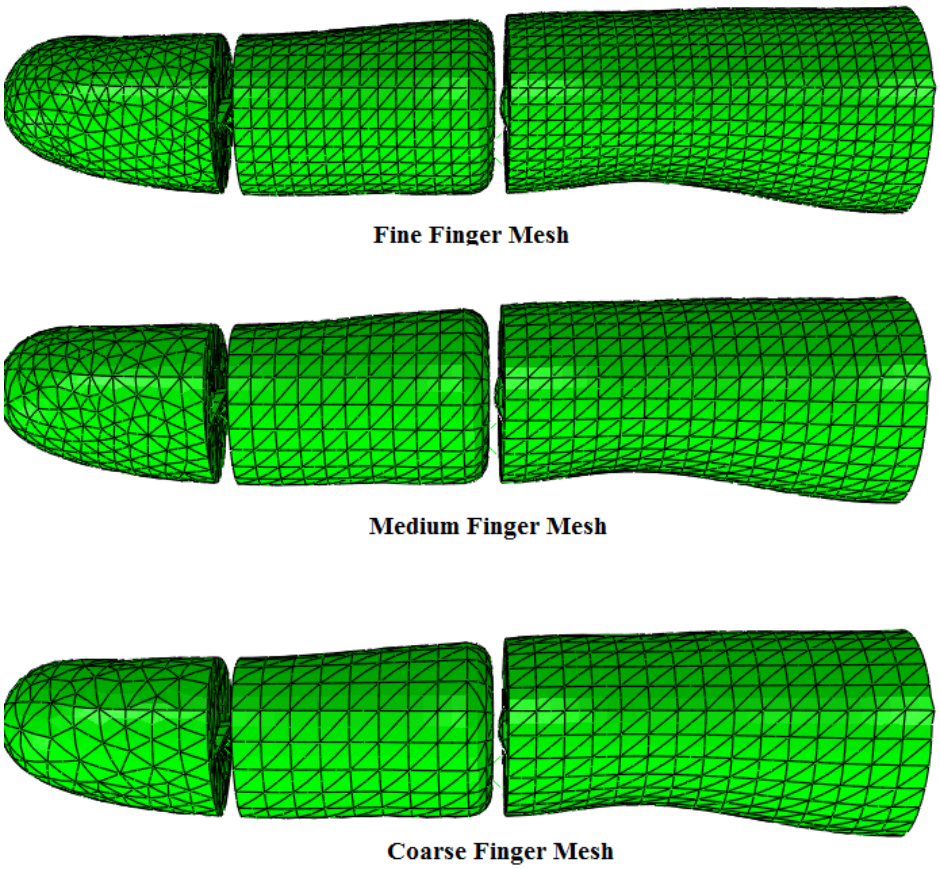

Figure 4.10: Finger Mesh Refinement Levels

Figure 4.11 shows the resultant joint torque about the Distal Interphalangeal joint due to contact with the glove for the coarse, medium and fine levels of mesh refinement of the finger. Figure 4.12 shows the resultant joint torque about the Proximal Interphalangeal joint due to contact with the glove for each level of mesh refinement of the finger.

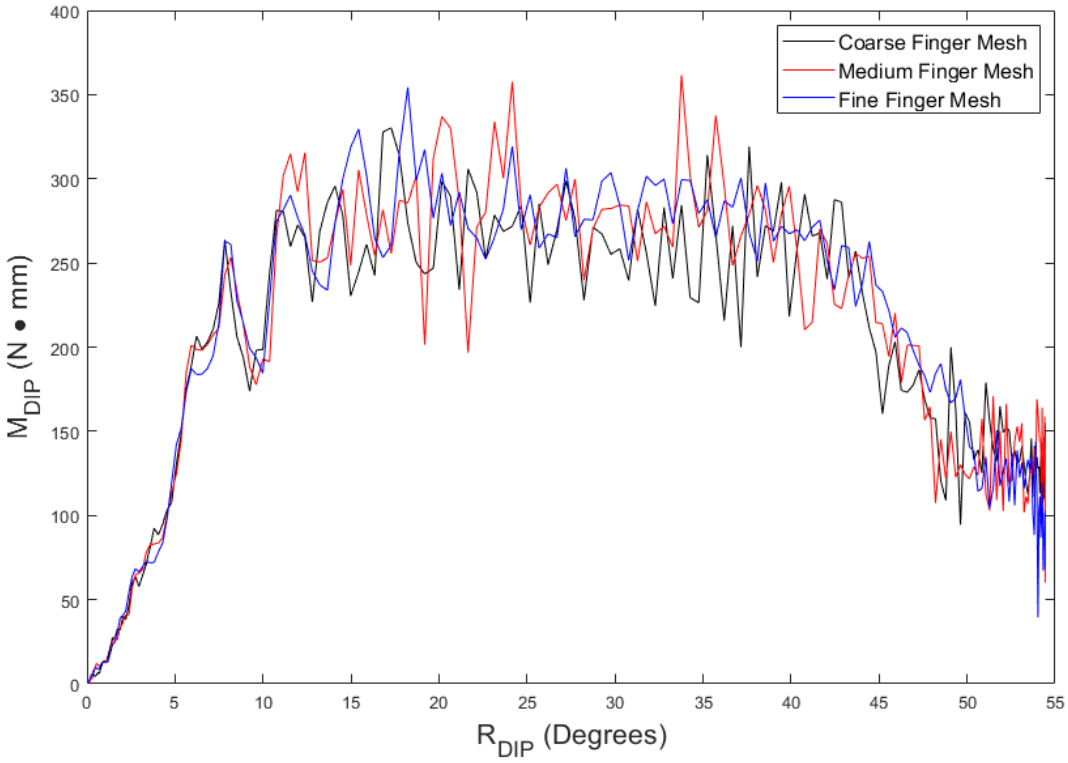

Figure 4.11: M_{DIP} Comparison for Finger Mesh Refinement

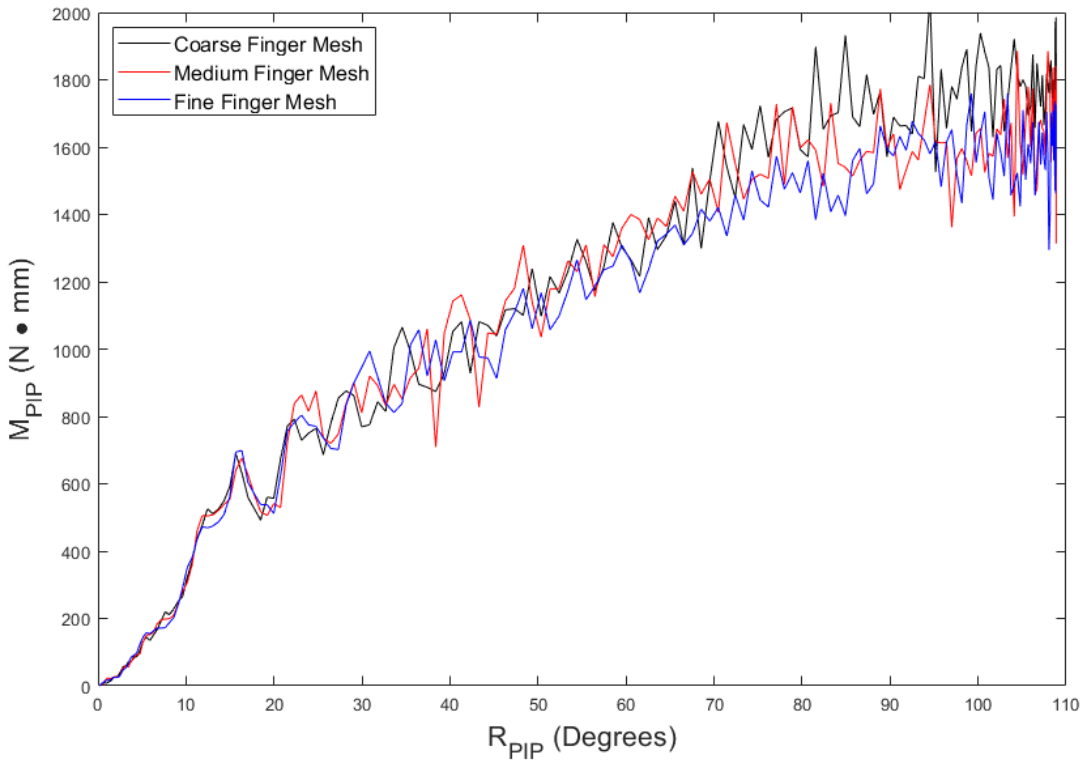

Figure 4.12: M_{PIP} Comparison for Finger Mesh Refinement

Figures 4.11 and 4.12 show that the mesh refinement of the finger has very little affect on the resistance of the glove. However, it is difficult to discern small differences in these plots. However, by applying a simple moving average filter to the data seen in Figures 4.11 and 4.12, one can compare the finger mesh refinements a bit more clearly.

Figure 4.13 shows the moving average of the joint torque about the DIP joint for each level of finger mesh refinement. Figure 4.14 shows the moving average of the joint torque about the PIP joint for each level of finger mesh refinement.

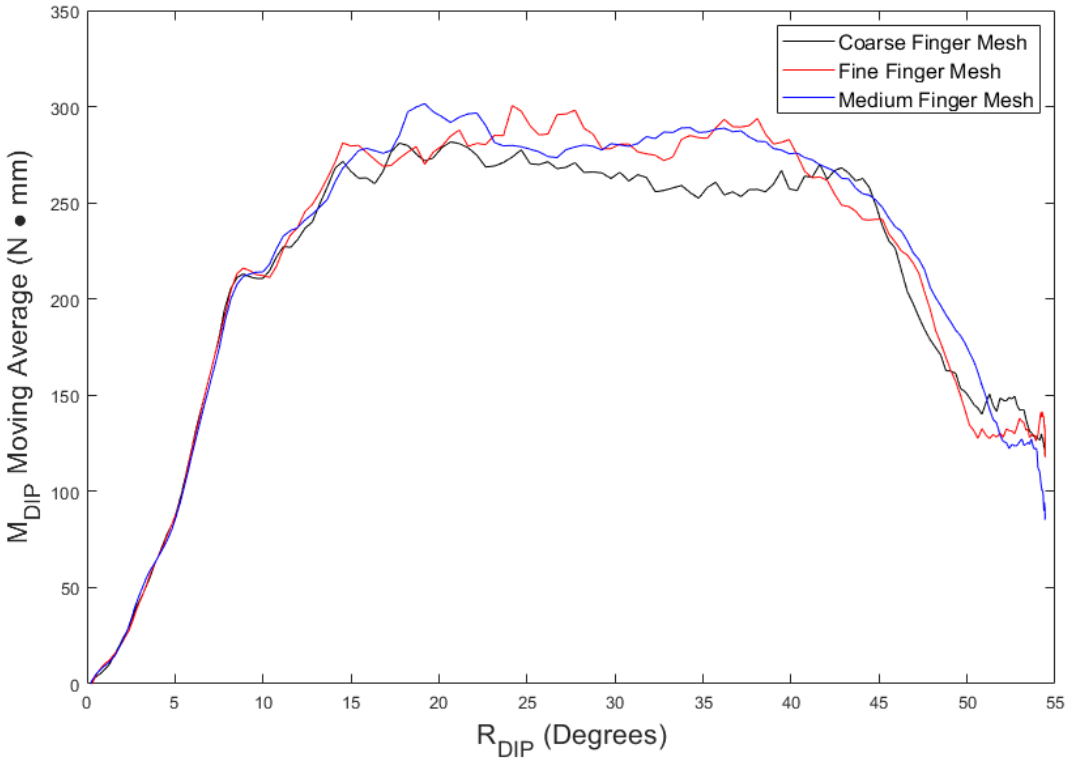

Figure 4.13: M_{DIP} Comparison for Pressure Bladder and Restraint Layer Mesh Refinements

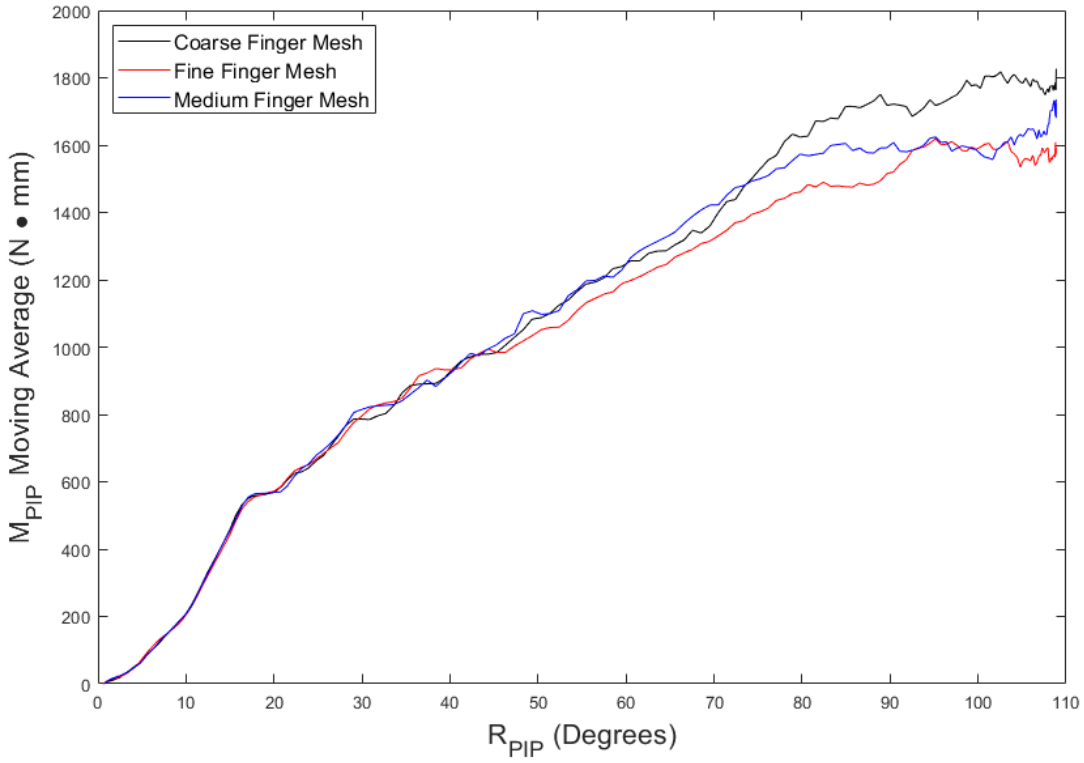

Figure 4.14: M_{PIP} Comparison for Pressure Bladder and Restraint Layer Mesh Refinements

Here, one can see that there is still not much disagreement between the levels of mesh refinement. However, at large rotations of the PIP joint (around 70 degrees), the coarse mesh starts to diverge from the medium and refined levels of mesh refinement. Because of this slight disagreement, the medium level of mesh refinement for the finger will be used for the remainder of the analysis.

After the required level of mesh refinement of the flesh was determined, a mesh refinement study was performed on the pressure bladder and restraint layer parts. Figures 4.15 and 4.16 show a comparison between glove resistance for each level of mesh refinement for the pressure bladder and restraint layers.

Figure 4.15 shows the comparison of joint torque about the DIP joint for each level of mesh refinement on the pressure bladder and restraint layer. Figure 4.16 shows the comparison of joint

torque about the PIP joint for each level of mesh refinement on the pressure bladder and restraint layer.

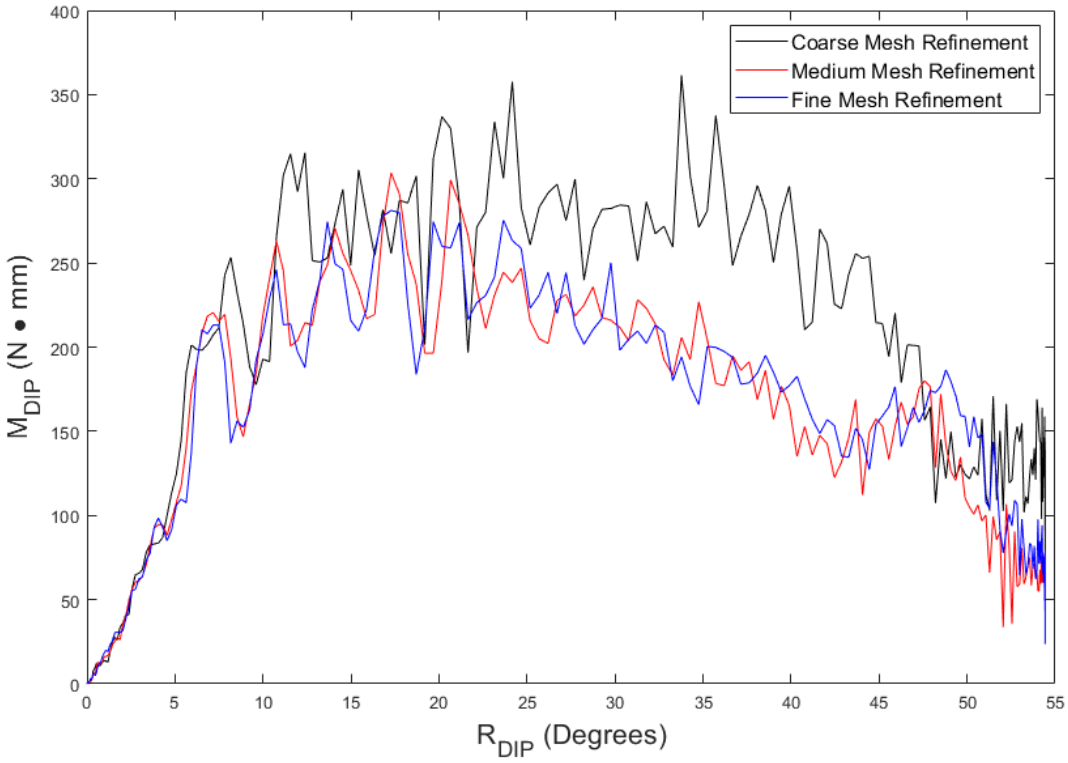

Figure 4.15: Comparison of M_{DIP} for Various Levels of Mesh Refinement

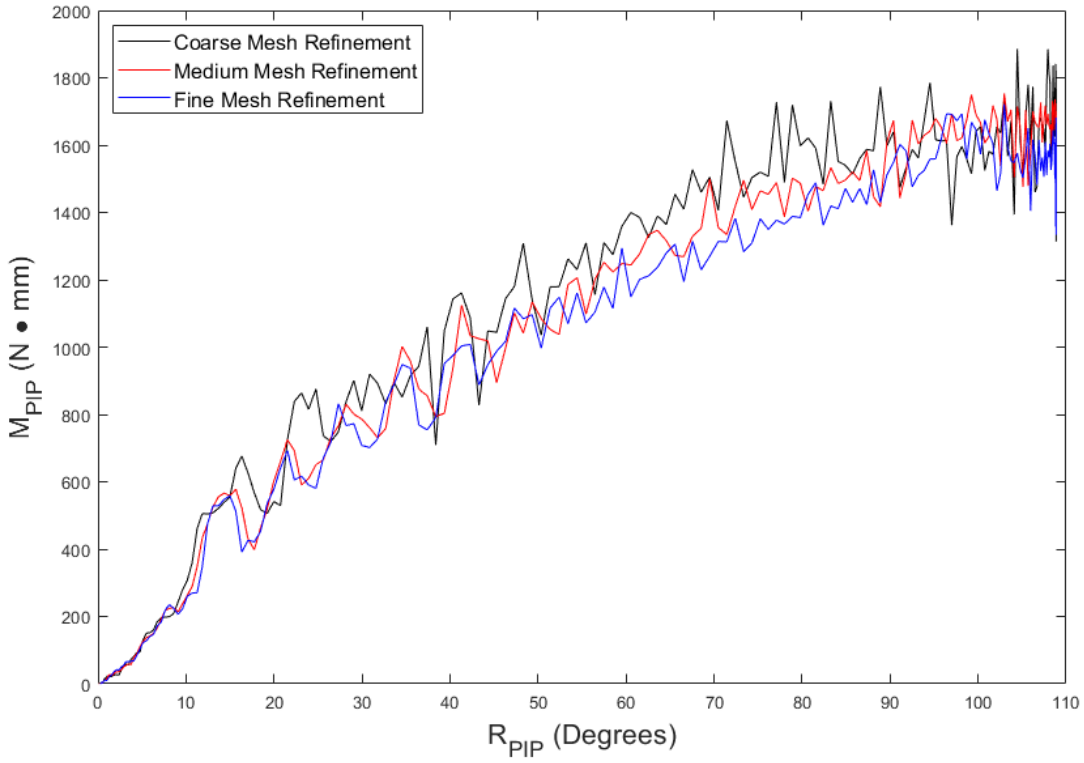

Figure 4.16: Comparison of M_{PIP} for Various Levels of Mesh Refinement

While it is clear that the coarse mesh level exhibits significant differences from the other mesh refinement levels for the joint torque about the DIP joint, it is difficult to see any other differences. However, by applying a simple moving average filter to the data, the differences become more clear (Figures 4.15 and 4.16) by eliminating excessive noise in the joint torque data..

Figure 4.17 shows a moving average of the joint torque about the DIP joint for each level of mesh refinement on the pressure bladder and restraint layer. Figure 4.18 shows a moving average of the joint torque about the PIP joint for each level of mesh refinement on the pressure bladder and restraint layer.

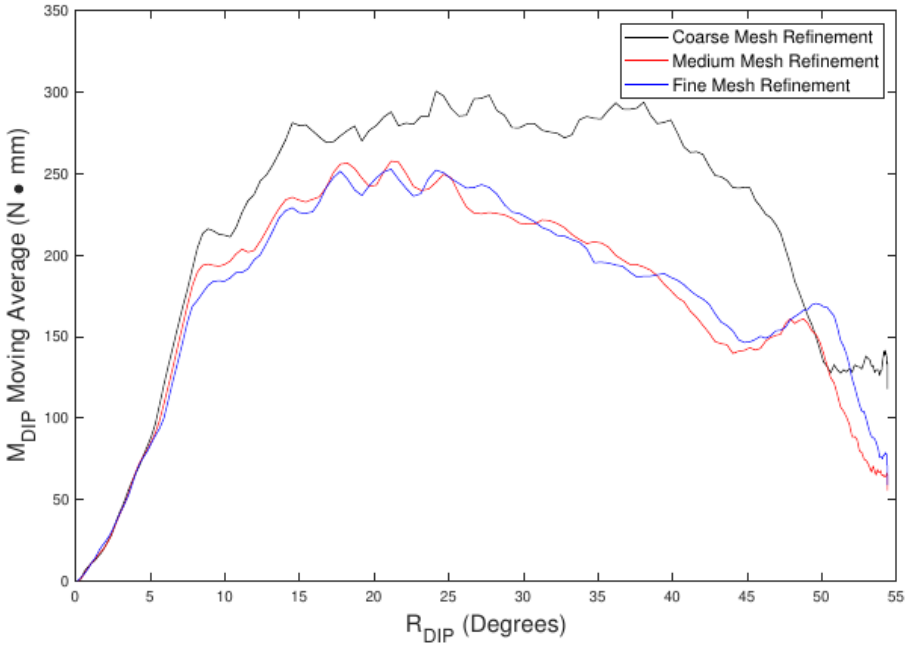

Figure 4.17: Comparison of M_{DIP} for Various Levels of Mesh Refinement

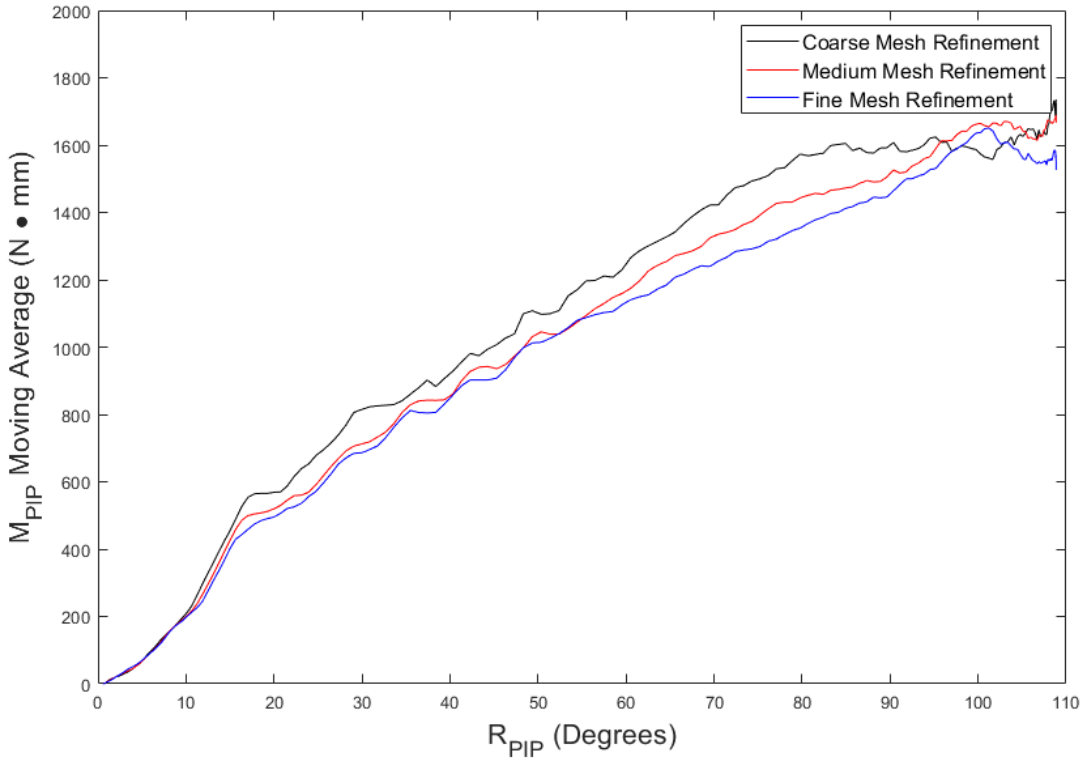

Figure 4.18: Comparison of M_{PIP} for Various Levels of Mesh Refinement

While the joint torque about the Distal Interphalangeal joint shows a significant difference between the coarse mesh and the fine/medium meshes, all three meshes show agreement with the joint torque about the Proximal joint. However, both the medium and fine levels of mesh refinement show agreement across both joint torques. Therefore, one can conclude that the medium mesh refinement has converged for the outputs of utmost interest for this research project. The medium level of mesh refinement will be used for the remainder of the analysis.

4.1.4 Experimental Comparison

While existing experimental data on the joint torque required to move a Phase VI EVA glove does not exist, a comparison between the output of this finite element model and experimental data can be made by using experimental data on the Russian Orlan glove produced by Mousavi et al. [27]. While the experimental data by Mousavi contains many unknowns and differences from this

model, it is the best comparison that can be made at this time.

It should be noted that the data generated by Mousavi was collected using a Russian Orlan Glove and the operating pressure of that suit (5.8 PSI). Additionally, the data was collected for all layers of the glove (including the TMG).

It is worth noting the interesting phenomenon that for both the DIP and PIP joints, there is some initial displacement of the joints despite no torque being applied to those joints. While the researchers do not address this issue, it is possible that this displacement was caused by the weight of the mechanical finger causing an initial torque on the joint and a resulting displacement that was not accounted for in the method the researchers used to measure joint torque. Despite this, a qualitative comparison can be made. Figure 4.19 compares M_{PIP} vs. R_{PIP} for both the Abaqus model and Mousavi et al's experimental data.

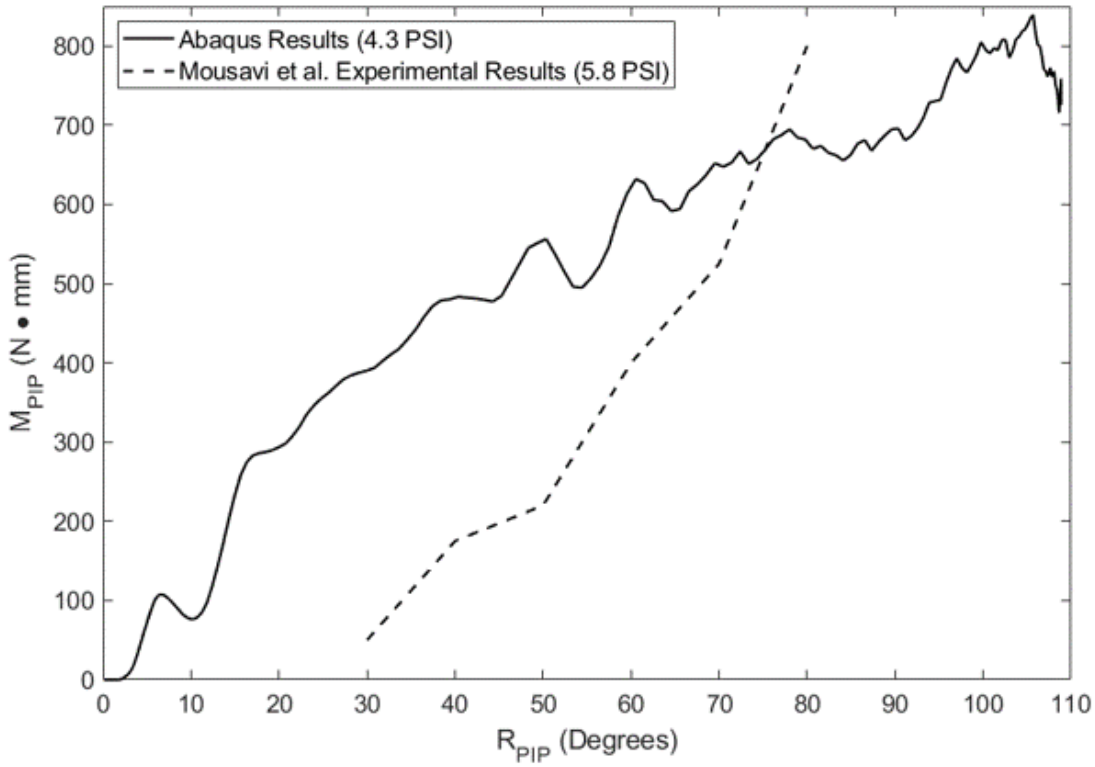

Figure 4.19: M_{PIP} vs. R_{PIP} for Abaqus Model and Mousavi et al. Experimental Data

Comparing the model results to those by Mousavi, one can see that the joint torques calculated using the finite element model are on the same order of magnitude of the experimental results. As the data by Mousavi et al. is the most relevant experimental data in the available literature for comparison to the finite element model, this is the best comparison that can be made at the current time. Because of this, in the future, more experimental data will need to be collected to validate the finite element model. However, as the purpose of this model currently is to understand the contributing factors to glove resistance and the sensitivities of joint torques to glove design, it is not of paramount importance that the exact value of the joint torque be experimentally validated at the current time.

4.2 Dominant Factors Contributing to Glove Resistance

This section presents the results from the study meant to determine the contributing factors to the glove resistance. Figure 4.20 shows the moment about the distal interphalangeal joint due to contact with the glove for the unpressurized case, pressurized case and case with double the nominal pressure load.

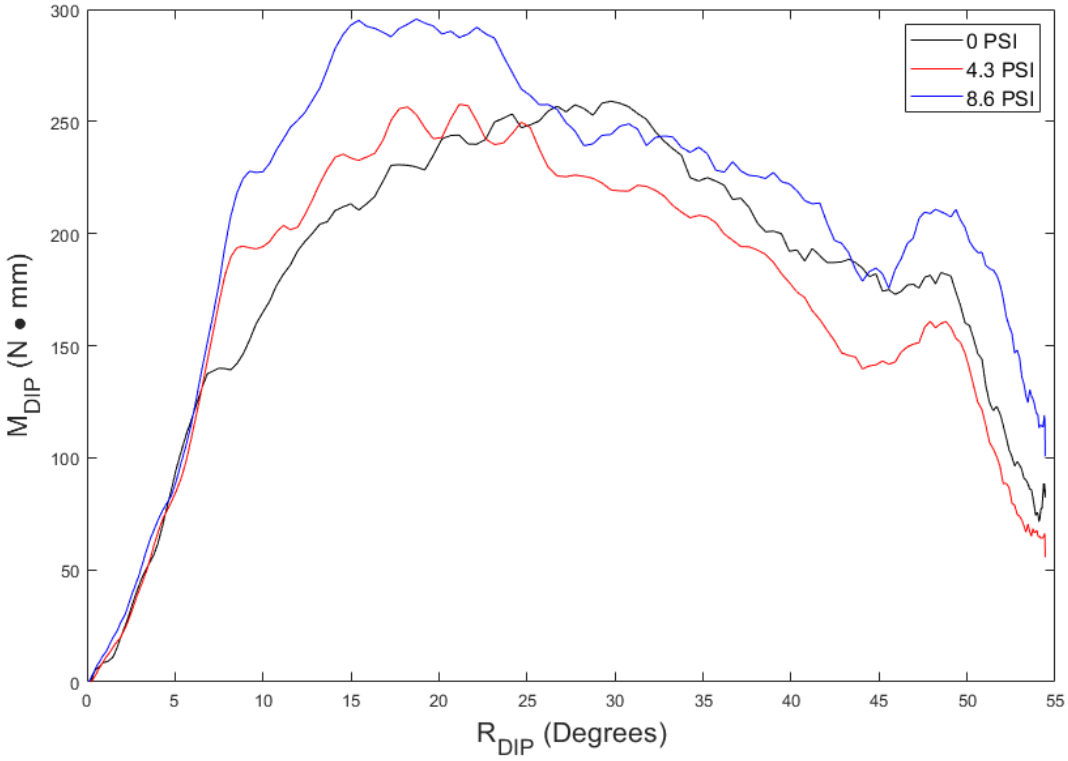

Figure 4.20: M_{DIP} vs. R_{DIP} Comparison Due to Internal Pressure

Figure 4.21 shows the moment about the proximal interphalangeal joint due to contact with the glove for the unpressurized case, pressurized case and case with double the nominal pressure load

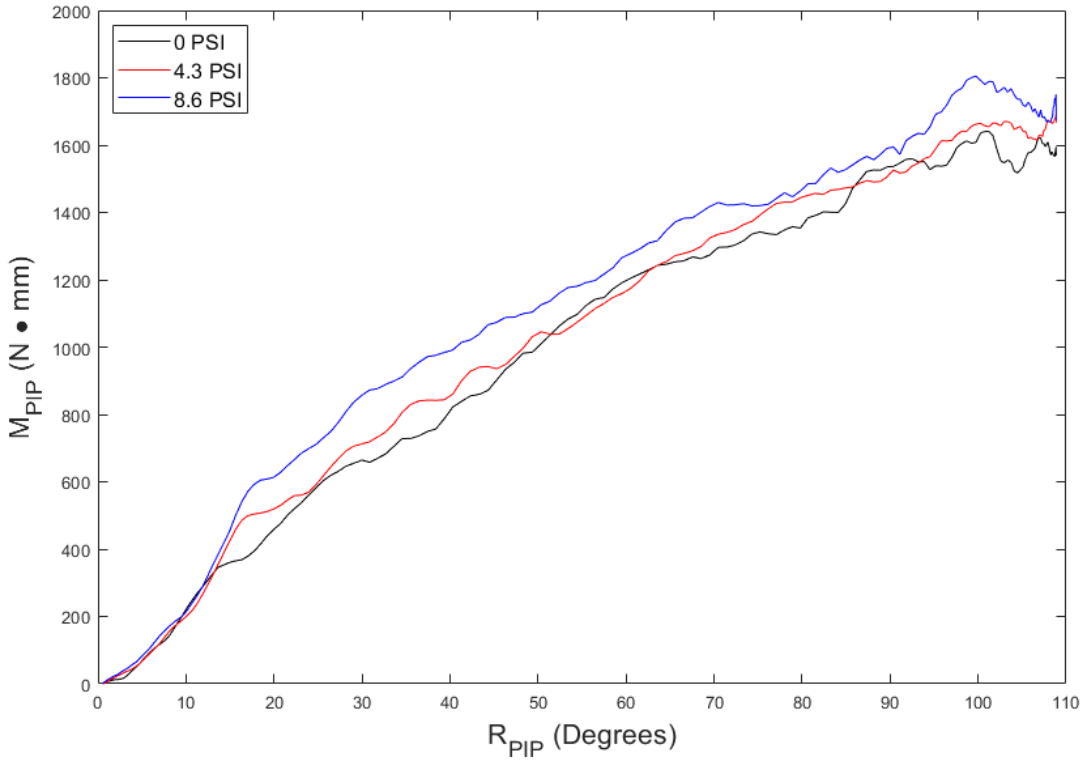

Figure 4.21: M_{PIP} vs. R_{PIP} Comparison Due to Internal Pressure

Figures 4.20 and 4.21 shows that increasing the pressure from 0 PSI to 4.3 PSI causes a very small increase in the overall resistance of the glove. However, increasing the pressure to 8.6 psi causes a significant increase in glove resistance. For the addition of a nominal pressure load, we see an increase in resistance of the glove on the order of 5 to 10%. This data agrees with existing experimental results for crewmember grip strength in pressurized and unpressurized conditions [17]. The experimental results show that the addition of pressure (in the glove without the TMG layer) decreases subject's grip strength from 66% of nominal to 58% of nominal. This shows that pressure provides around a 10% increase in glove resistance.

Figure 4.22 shows bunching's contribution to glove resistance as defined in Equation 3.3 in Section 3. This figure shows the relationship between proximal interphalangeal joint torque and joint rotation due to bunching of the glove for the unpressurized glove, pressurized glove and

double-pressure glove.

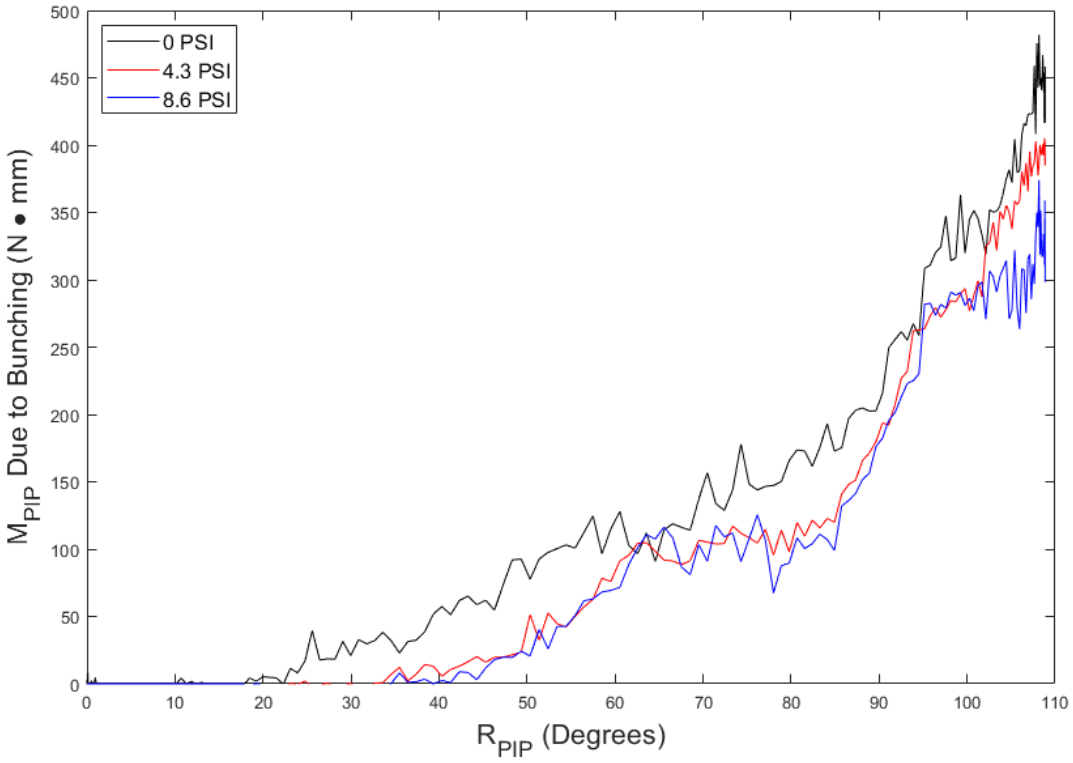

Figure 4.22: M_{PIP} vs. R_{PIP} Comparison Due to Bunching

From Figure 4.22, one can see that the resistance contribution due to bunching increases rapidly as the finger is bent. As the finger starts to bend, bunching provides no resistance to motion as wrinkling and bunching have yet to occur. However, at around 20 degrees of rotation of the PIP joint in the unpressurized case, bunching starts to occur and inhibit the motion of the finger. For the pressurized and double pressure cases, this starts to occur around 40 degrees of rotation. As bunching occurs, all three cases follow a similar trend and the joint torque contribution due to bunching increases steadily. One interesting phenomenon illustrated in this graph is the effect of pressure on the resistance contribution due to bunching. Throughout the entire motion of the finger, the unpressurized case provides the most resistance due to bunching. Figure 4.23 shows a

sectioned view of the unpressurized and pressurized cases.

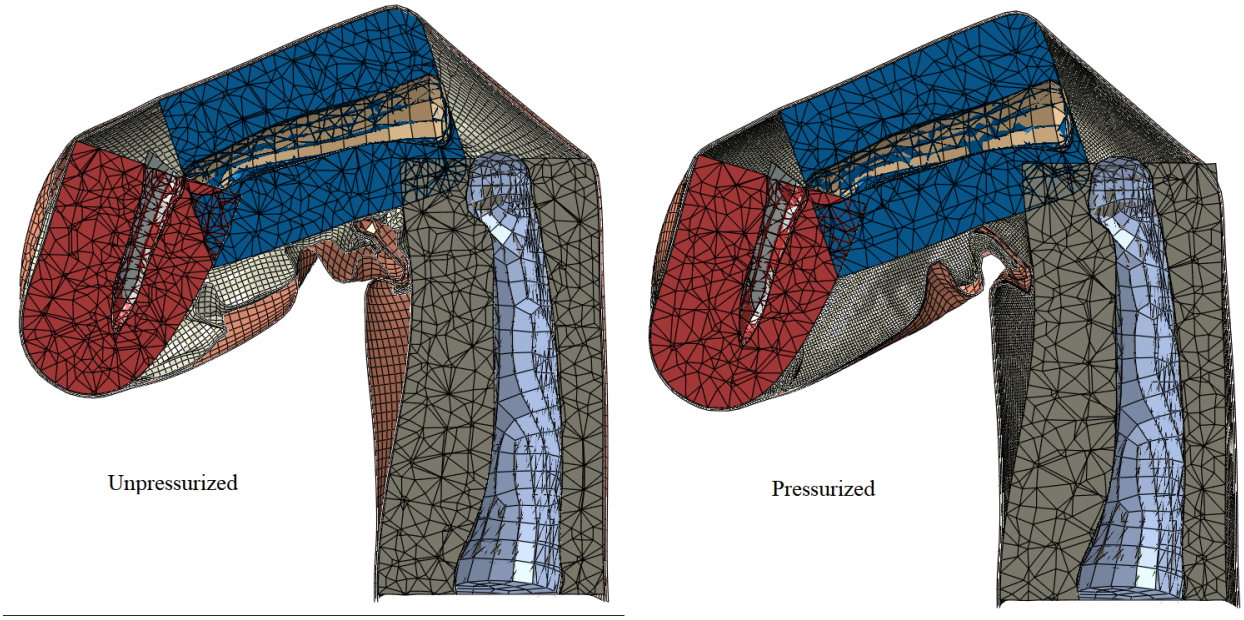

Figure 4.23: Comparison of Bunching for Pressurized and Unpressurized Glove

Figure 4.23 illustrates the cause of the reduction in resistance due to bunching for the pressurized case. Bunching occurs much sooner and much greater in the unpressurized glove than the pressurized. Pressure is providing a stabilizing load and acts to limit the amount of bunching of the glove during bending. While the addition of a nominal internal pressure (of 4.3 PSI) does significantly reduce the contribution of glove resistance due to bunching, Figure 4.22 shows that the addition of a larger internal pressure (of 8.6 PSI) does not further limit the resistance contribution due to bunching.

Finally, Figure 4.24 shows the glove resistance contribution due to the resistance of the pressure bladder and restraint layer materials as defined in Section 3.6.

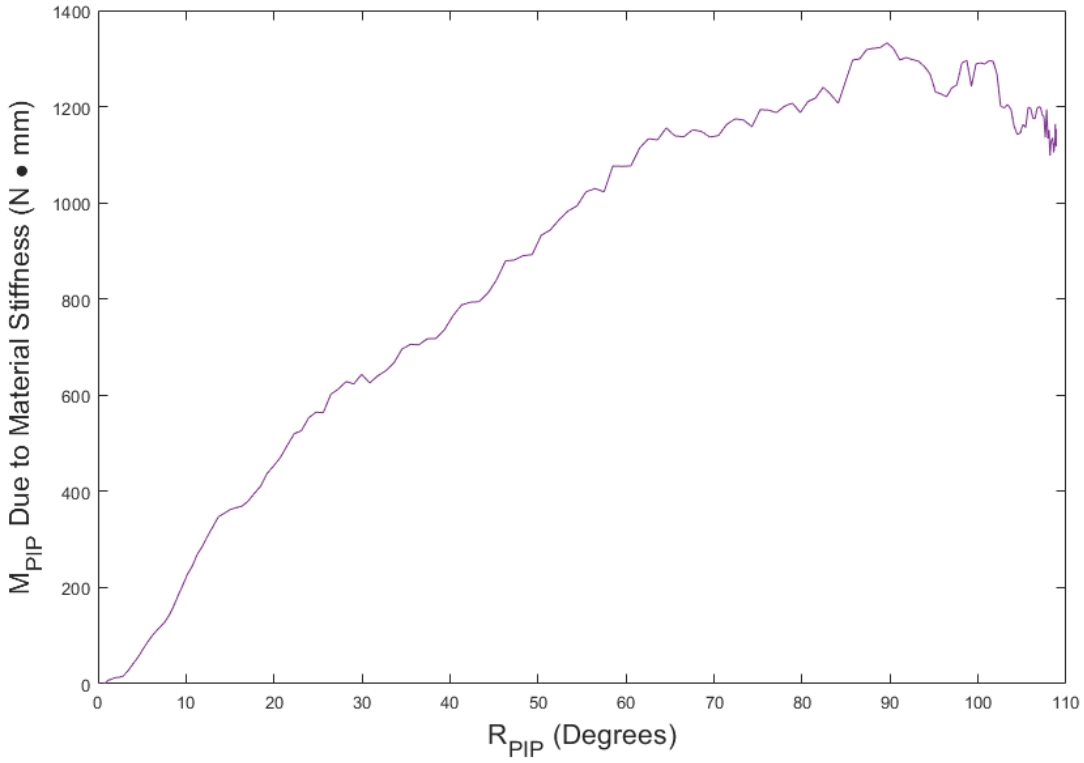

Figure 4.24: Glove Resistance Contribution due to Material Stiffness

There are a number of implications from the investigation into the contributing factors of glove resistance. First, is that material stiffness is the greatest contributing factor to glove resistance. Therefore, when designing the next generation of gloves, care should be made to select compliant materials wherever possible. The next largest contribution to glove resistance is bunching of the material. While wrinkling and bunching is inevitable in the bending of thin membrane structures, care should be taken to design gloves that delay and inhibit the formation of bunching. While the presence of an internal pressure reduces the effects of bunching, it was shown that the use of a larger internal pressure shows no additional reduction of the bunching effects and results in a significantly stiffer glove than the nominal pressure case.

As the effects of bunching become more significant as more rotation of the finger occurs, one possible solution would be to design a glove that is configured to have no bunching at a specific

"equilibrium" point. While the glove finger idealization used in this model was designed for an "equilibrium" point of zero finger bending, it is possible to design a glove that requires no torque to maintain the most common hand posture used in EVA. While there is currently no available literature on the specifics of this posture, it is likely that repetitive dexterous tasks such as traversing hand rails or using a Pistol-Grip tool require a significant amount of hand strength and are some of the most common hand postures in EVA. The ability to maintain those hand postures with minimal strength could provide a serious effective performance increase.

4.3 Approximation of Pre-Bunching of Restraint Layer

While the model used for the remainder of this analysis ignores the pre-bunching of the restraint layer, it is important to understand how that bunching affects the overall response of the glove. As the pre-bunching effectively reduces the in-plane stiffness of the restraint layer, a first-order approximation was considered where the material modulus of the restraint layer was reduced in the area of largest stress. Figure 4.25 illustrates the area of reduced modulus.

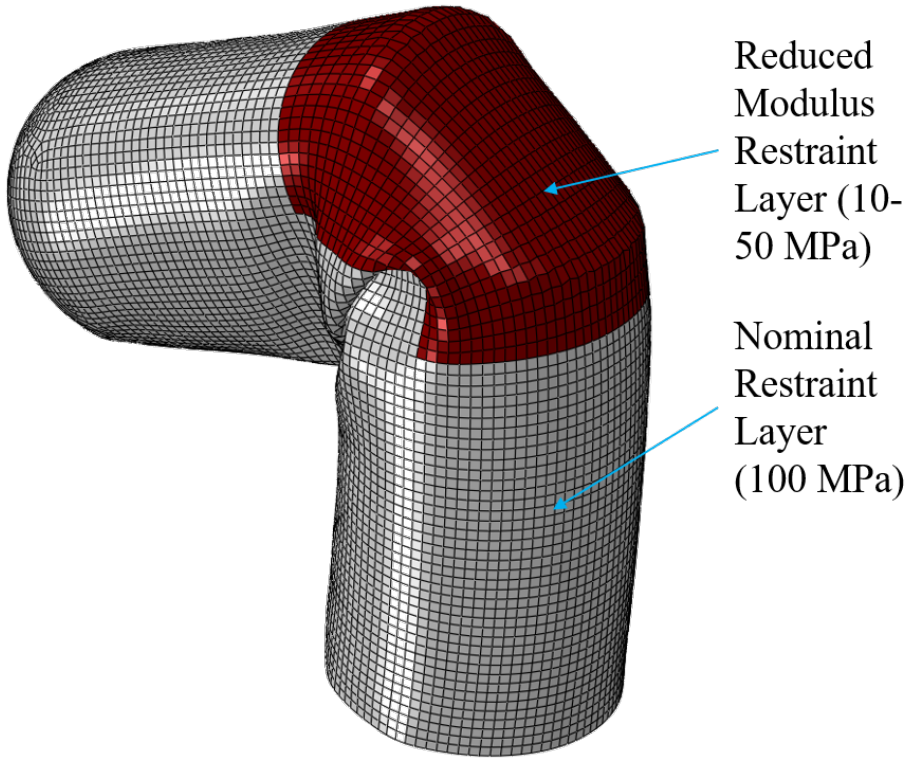

Figure 4.25: Approximation of Pre-Bunching of Restraint Layer

In addition to the nominal material modulus, two reduced modulus configurations were considered, one where the material modulus was reduced from 100 MPa to 50 MPa and the other reduced to 10 MPa.

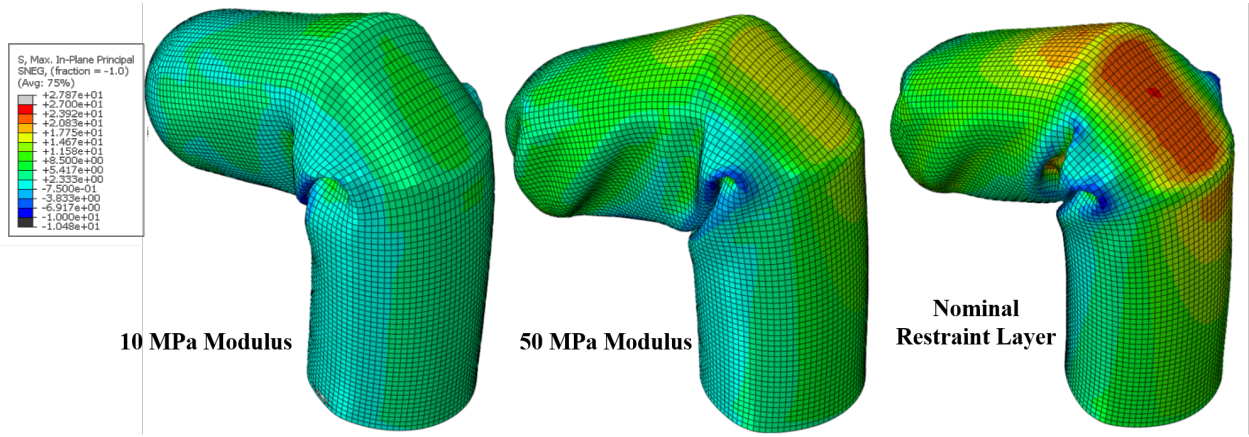

Figure 4.26: Maximum In-Plane Stress for Pre-Bunching Approximation of Restraint Layer

As expected, reducing the material modulus in the area of highest stress reduces the stress in that area. From this first-order approximation of the effects of the pre-bunching of the restraint layer, one can see that the pre-bunching significantly reduces the stress in the restraint layer. Figure 4.27 shows the comparison between glove resistance for each of the three above cases.

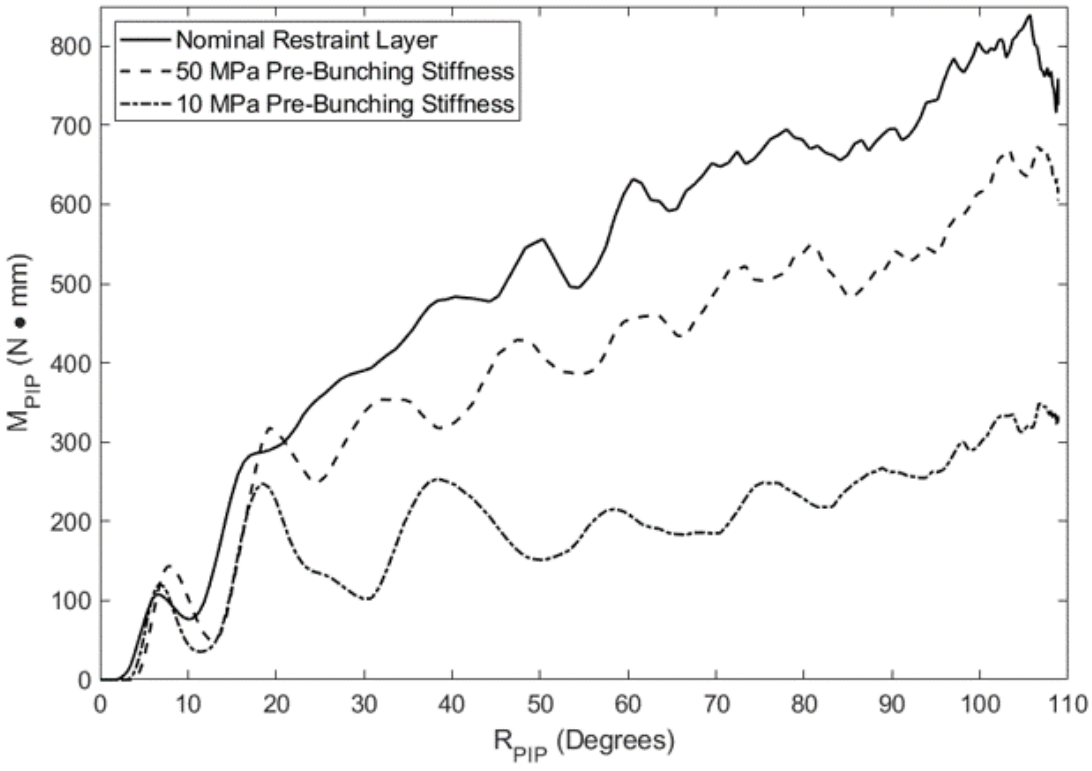

Figure 4.27: M_{PIP} vs. R_{PIP} for Restraint Layer Pre-Bunching Approximation

One can see that reducing the modulus of the restraint layer in the area of highest stress by a factor of 10 reduces the resistance of the glove to nearly half of its notional value. While the further analysis discussed in this thesis neglects any of the pre-bunching effects of the restraint layer, it is important to note that this appears to be a significant factor in resulting glove resistance and further analysis should incorporate a more refined model of the restraint layer.

4.4 Effect of Glove Design Variables on Glove Performance

This section presents the results from the parametric study on the effects of glove design parameters on glove performance. For each design variable, M_{DIP} vs R_{DIP} and M_{PIP} vs R_{PIP} were averaged over all cases with a specific level of that design variable. This allows for the direct comparison of the sensitivity of glove resistance to that specific design variable.

4.4.1 Convolute Radius Effects

Figure 4.28 shows the effects of convolute radius on the glove resistance about the DIP joint. This shows the resistance averaged over all cases for both the low value and high value of the convolute radius. From Figure 4.28, it is clear that the convolute radius has a large effect on the glove resistance about the DIP joint at approximately 45 degrees of rotation of the DIP joint.

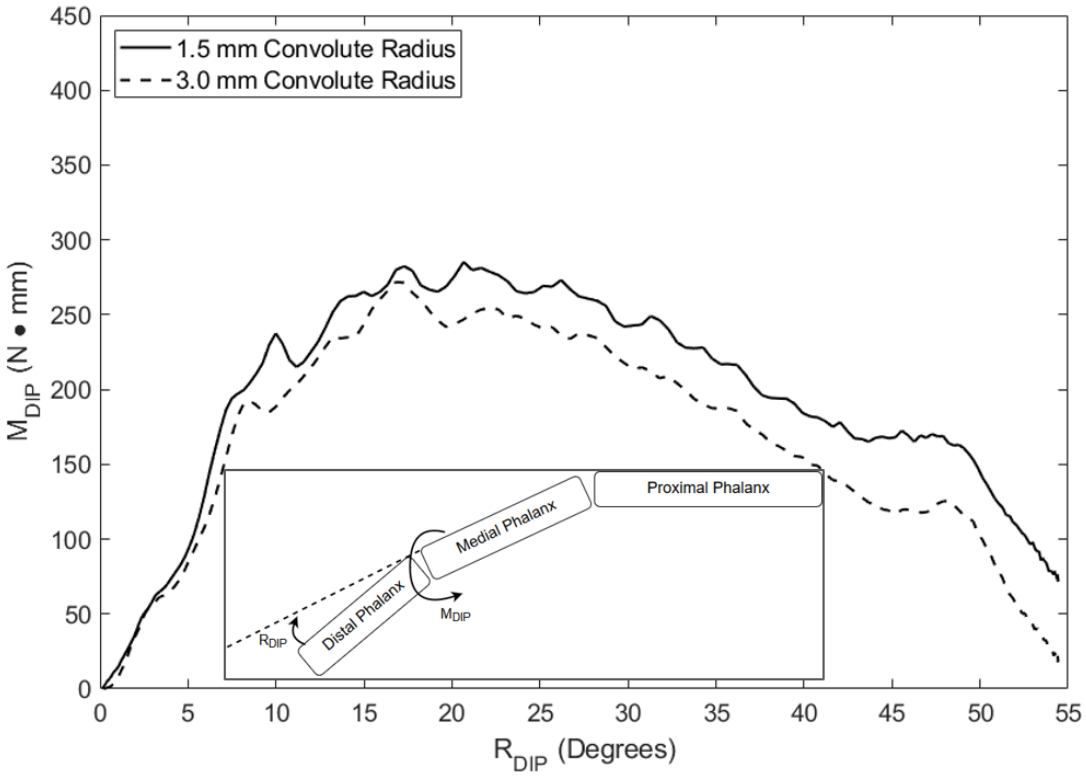

Figure 4.28: Effect of Convolute Radius on M_{DIP}

Figure 4.29 shows the effects of convolute radius on glove resistance about the PIP joint. This shows the resistance averaged over all cases for both the high and low values for the convolute radius. Here, similar effects to those seen in the resistance about the DIP joint are seen. The larger convolute radius reduces the resistance of the glove by approximately 10%.

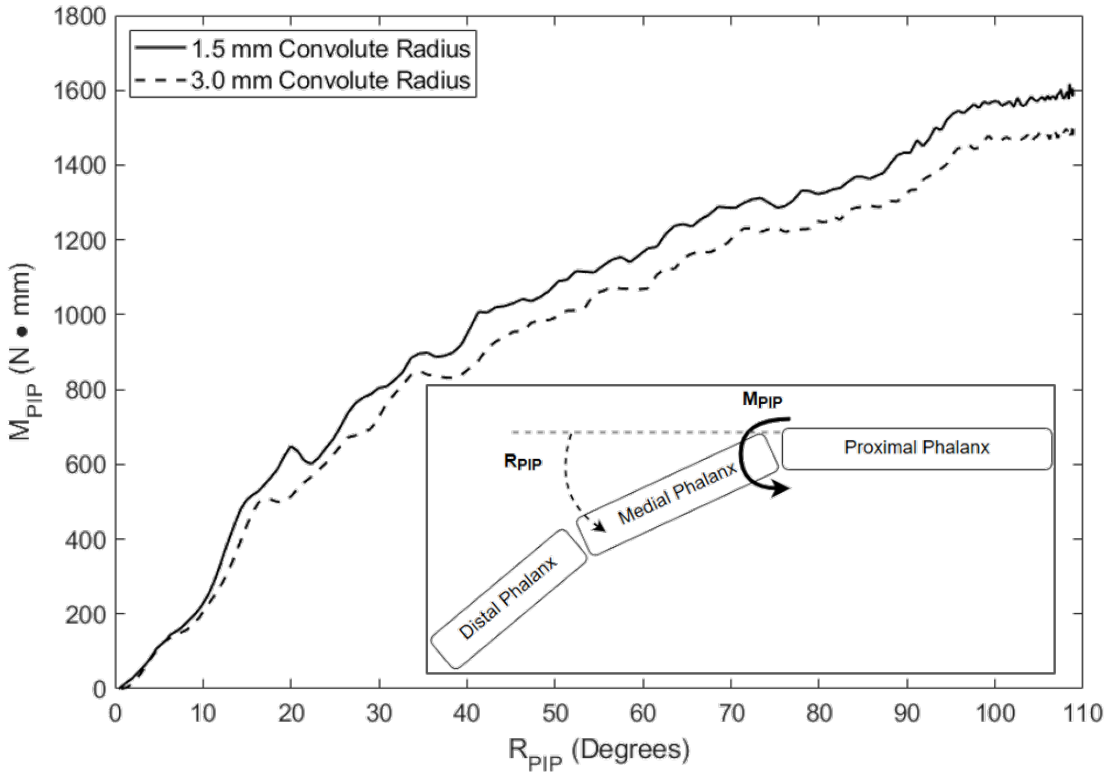

Figure 4.29: Effect of Convolute Radius on M_{PIP}

Figure 4.30 shows the deformed configurations for a glove design with 1.5 mm convolute radius and 3.0 mm convolute radius with all other design parameters held constant. While the response of the glove finger looks quite similar for the two configurations, careful inspection of the area of bunching shows the primary difference between the two designs. The larger convolutes result in less tight bunching, spreading the contact force out on a larger portion of the palmar surface of the medial finger segment.

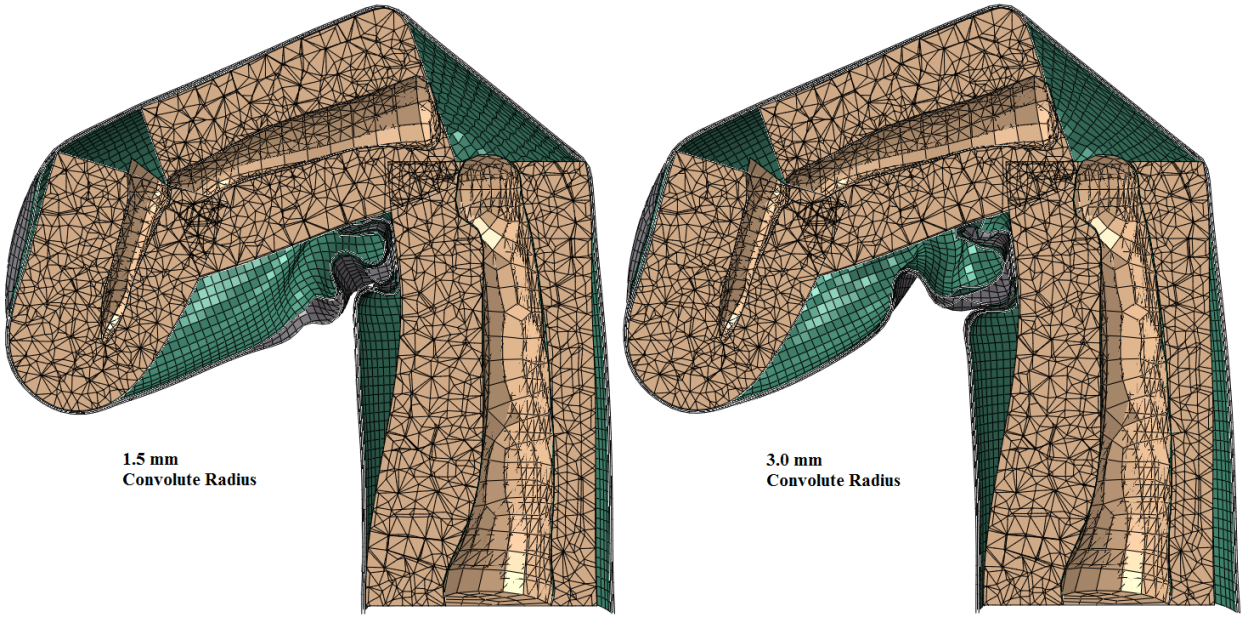

Figure 4.30: Convolute Radius Comparison - Deformed Configurations

4.4.2 Number of Convolutes Effects

Figures 4.31 shows the effects of the number of convolutes on the resulting glove resistance about the DIP joint. One can see that there is little difference in the DIP joint torque between the 5 convolute and 3 convolute cases.

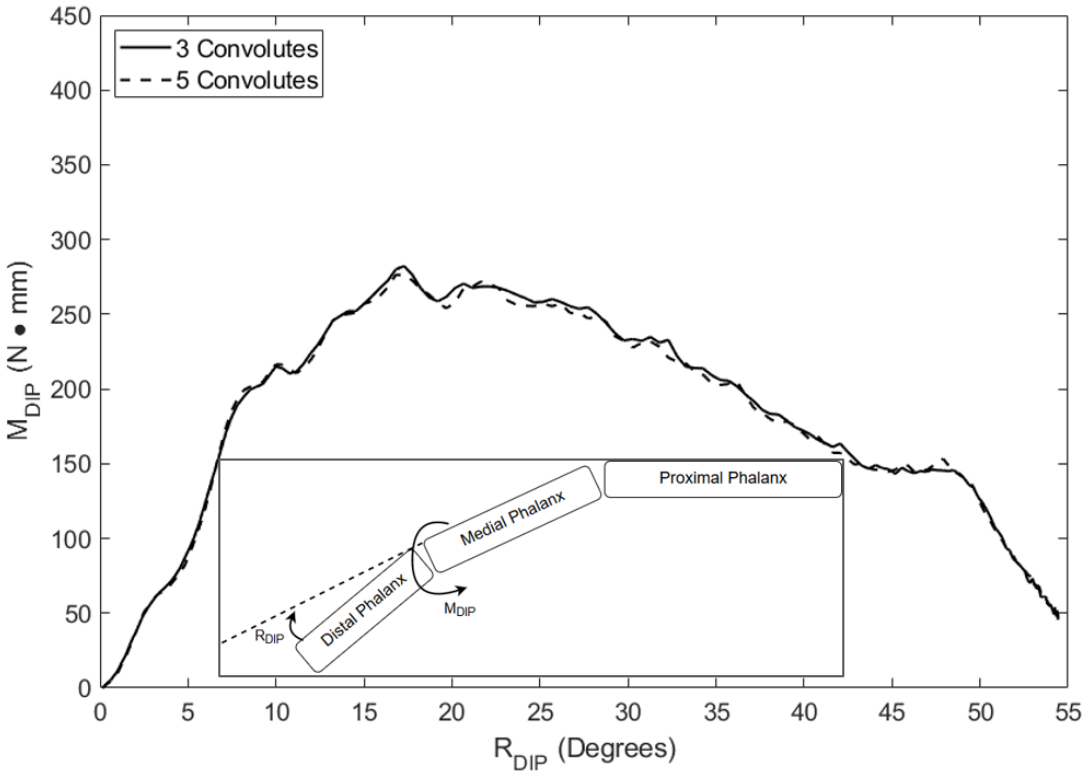

Figure 4.31: Effect of the Number of Convolutes on M_{DIP}

Figure 4.32 shows the effects of the number of convolutes on PIP joint torque. Here, there is a noticeable difference in the resulting joint torque between the 3 and 5 convolute case with the 5 convolute case requiring a joint torque approximately 2% less than the 3 convolute case for a given rotation of the finger.

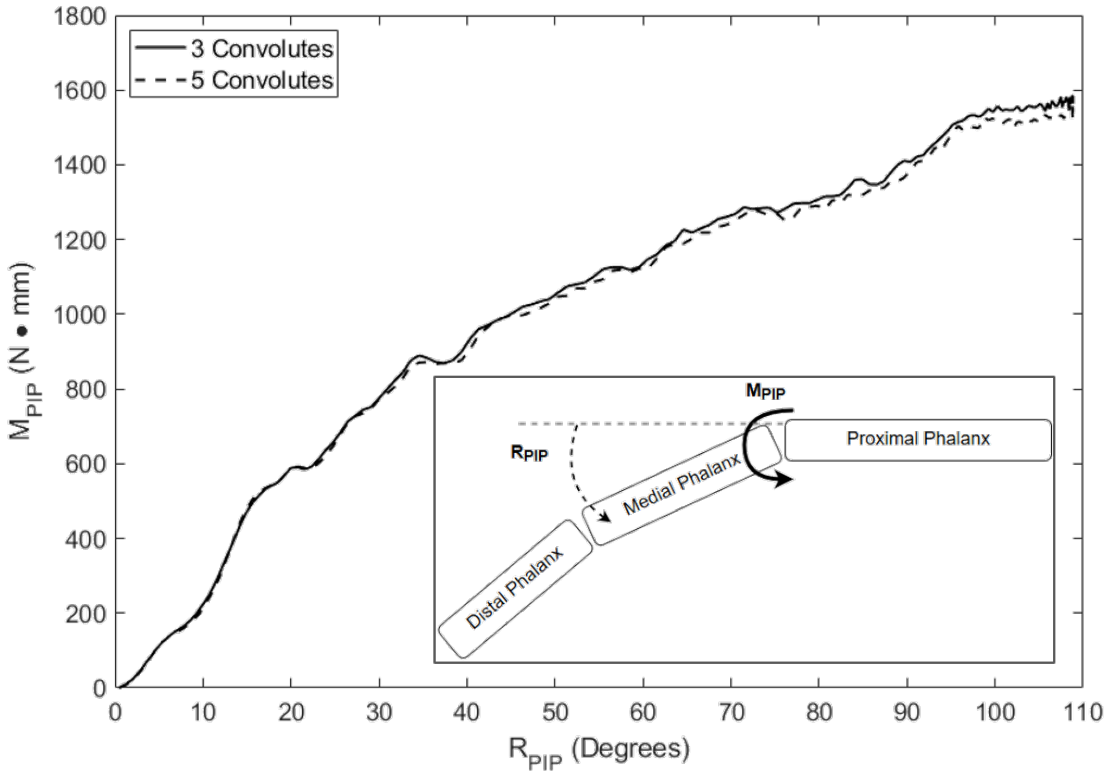

Figure 4.32: Effect of the Number of Convolutes on M_{PIP}

Figure 4.33 shows the deformed configuration for a glove design with 3 convolutes and 5 convolutes with all other design parameters held constant. Here, one can see slightly less bunching in the glove design with 5 convolutes.

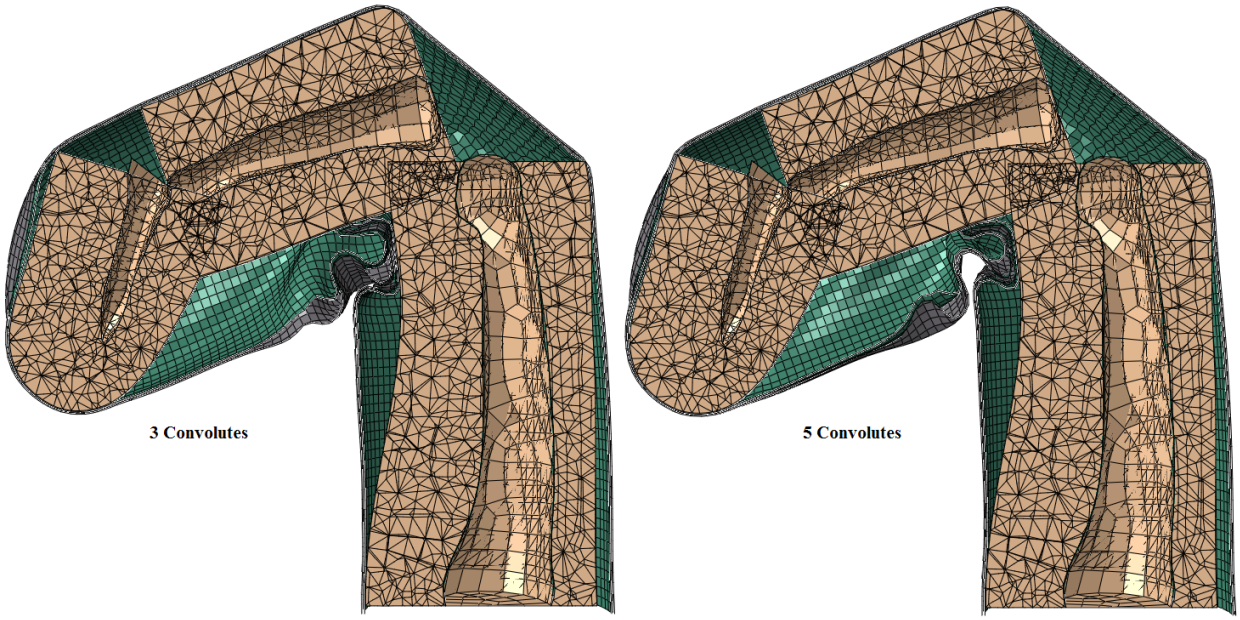

Figure 4.33: Number of Convolutes Comparison - Deformed Configurations

4.4.3 Convolute Location Effects

Figures 4.34 shows the resulting resistance about the DIP joint for the high and low values of the convolute starting location. This figure shows that while there is some effect of varying the location of the convolutes on the DIP joint torque, that effect is quite small.

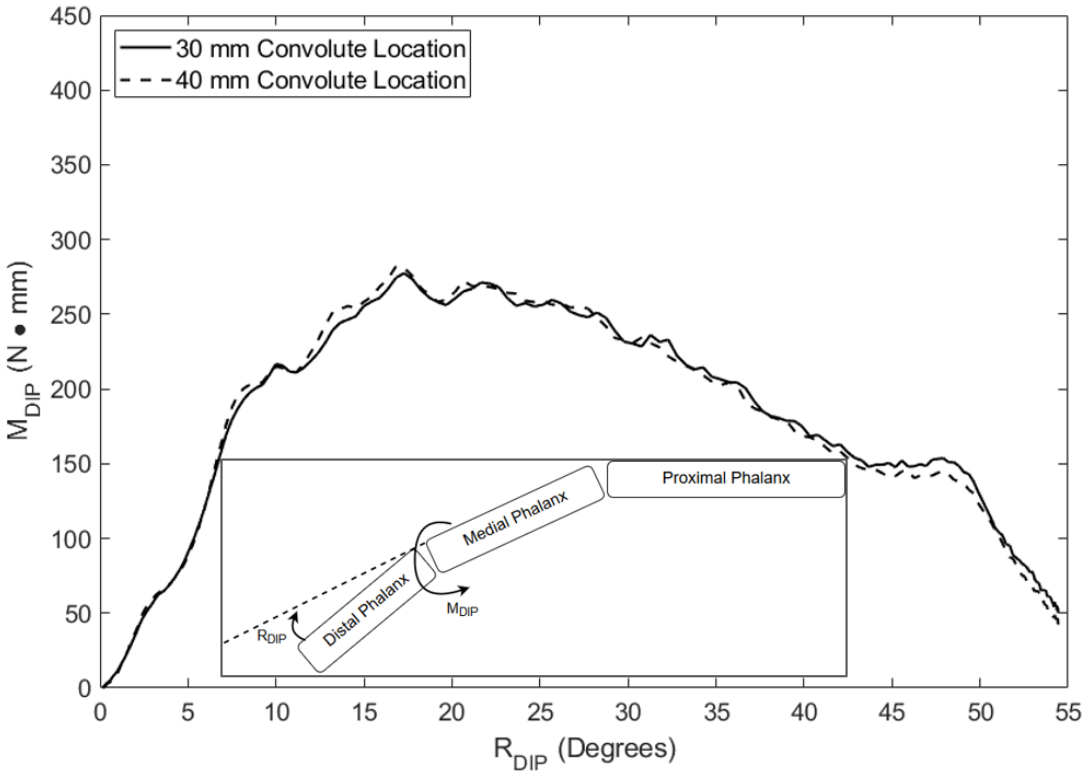

Figure 4.34: Effect of Convolute Starting Location on M_{DIP}

Figure 4.35 shows the results for the joint torque about the PIP joint for both the high and low values of the convolute starting location. The results seen in this figure are similar to those for the DIP joint torque. A very small effect on the performance of the glove is caused by varying the convolute location.

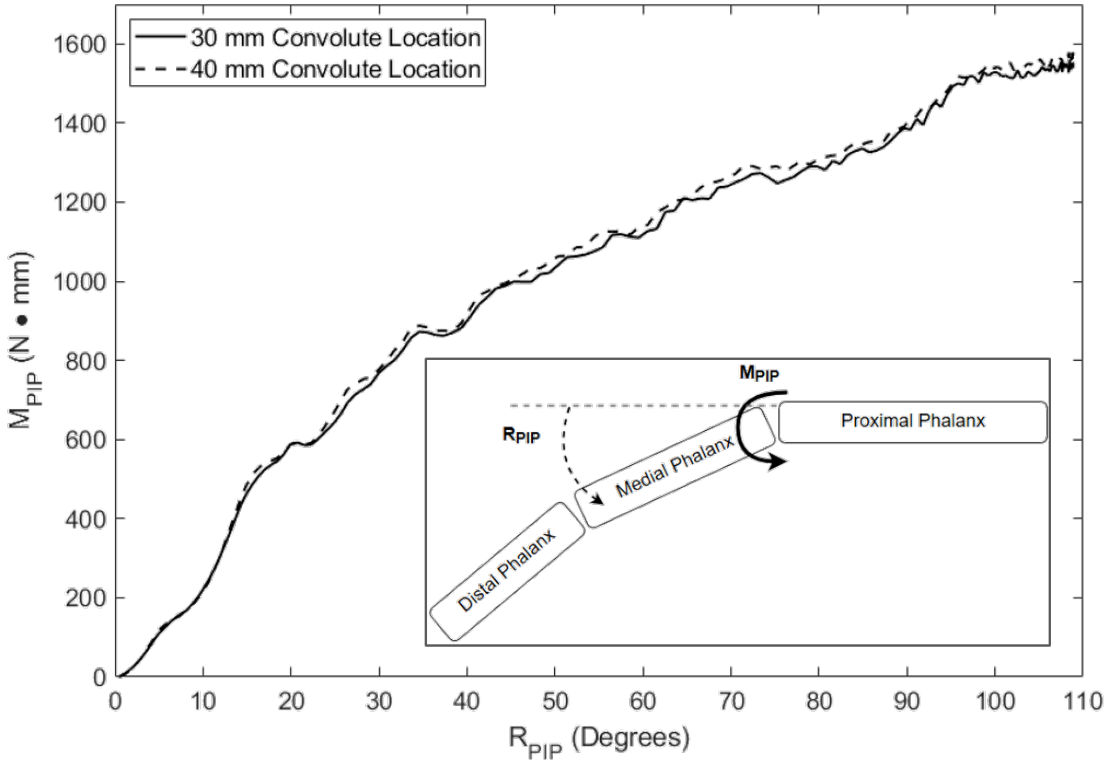

Figure 4.35: Effect of Convolute Starting Location on M_{PIP}

Figure 4.36 shows the deformed configuration for a glove design with a 30 mm convolute starting location and 40 mm convolute starting location with all other design parameters held constant. This figure illustrates the underlying cause of the slight increase in glove resistance for the 40 mm convolute starting location. One can see slightly more bunching in this design, providing more resistance about the PIP joint.

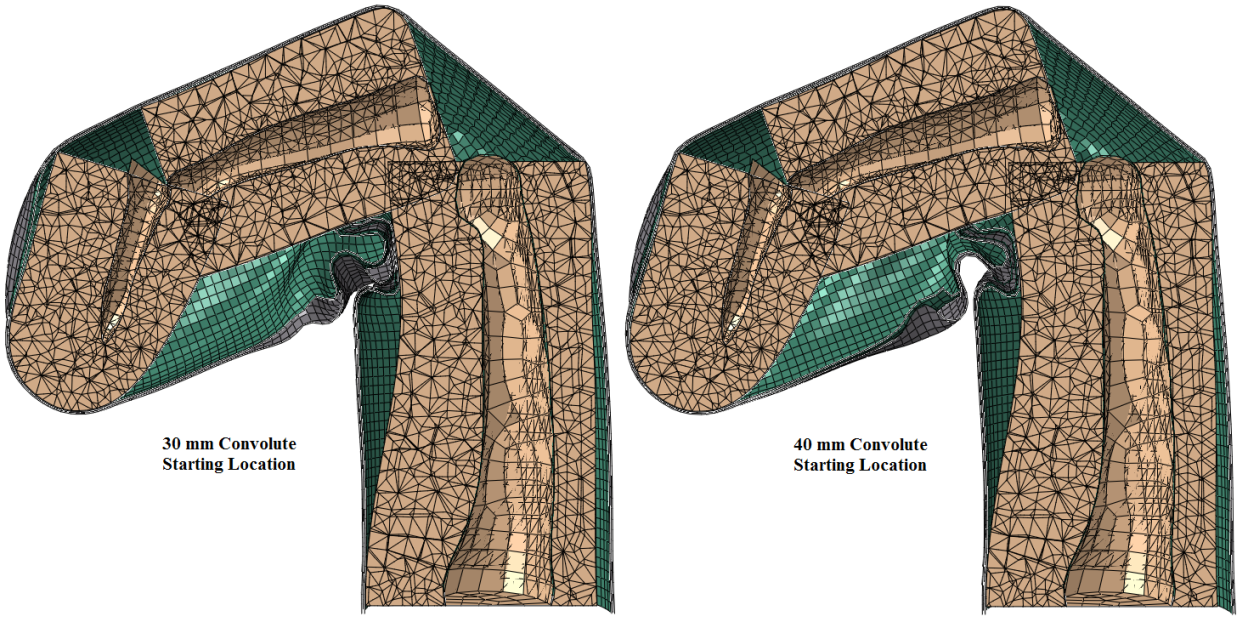

Figure 4.36: Convolute Starting Location Comparison - Deformed Configurations

4.4.4 Glove Internal Pressure Effects

Figures 4.37 and 4.38 show the effects of glove pressure on the resistance of the glove about the DIP and PIP joints respectively. These graphs show that there is very little effect of glove pressure when averaged over all other design parameters. This is contradictory to the results seen in figures 4.20 and 4.21. It should be noted that the results of the resistance contribution were for one single glove design. As many different glove configurations are considered, and the effects averaged across all of those designs, it becomes apparent that pressure has a smaller effect on the resulting glove resistance.

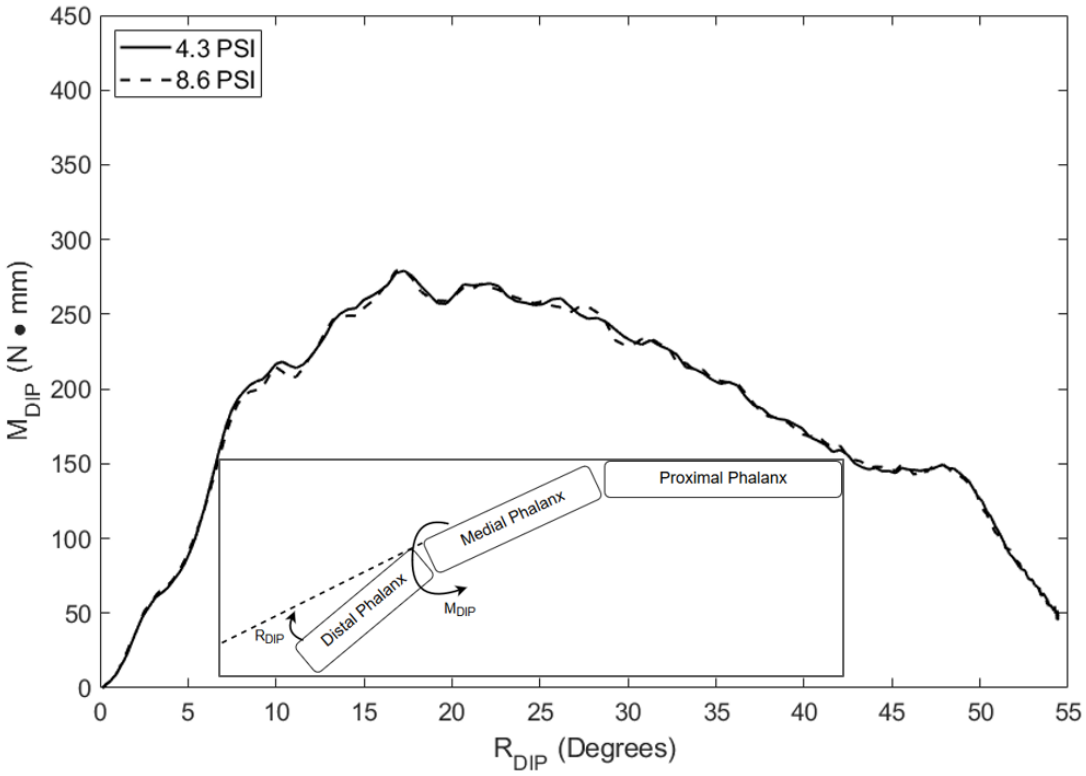

Figure 4.37: Effect of Glove Internal Pressure on M_{DIP}

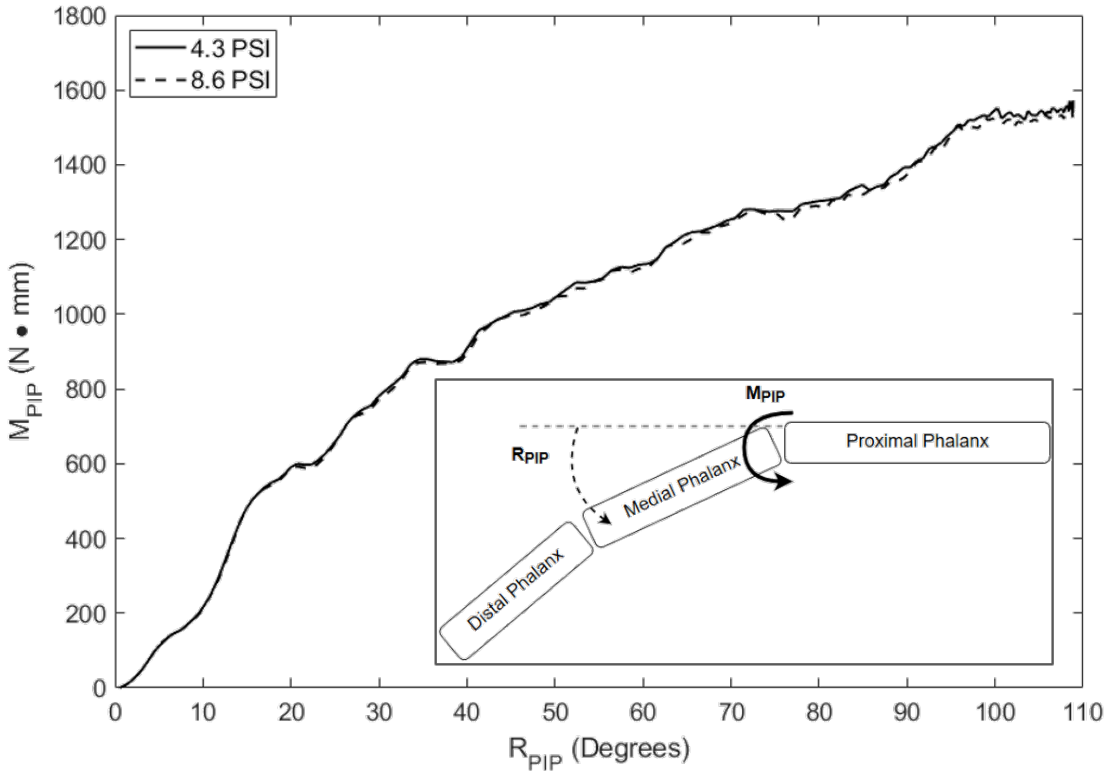

Figure 4.38: Effect of Glove Internal Pressure on M_{PIP}

Figure 4.39 shows the deformed configuration for an internal pressure of 4.3 PSI and 8 PSI with all other design variables held constant. There is no discernible difference between the response of this design between the two pressure levels. This is backed up by the quantitative data that shows no increase in resistance due to the addition of pressure when averaged across all tested designs.

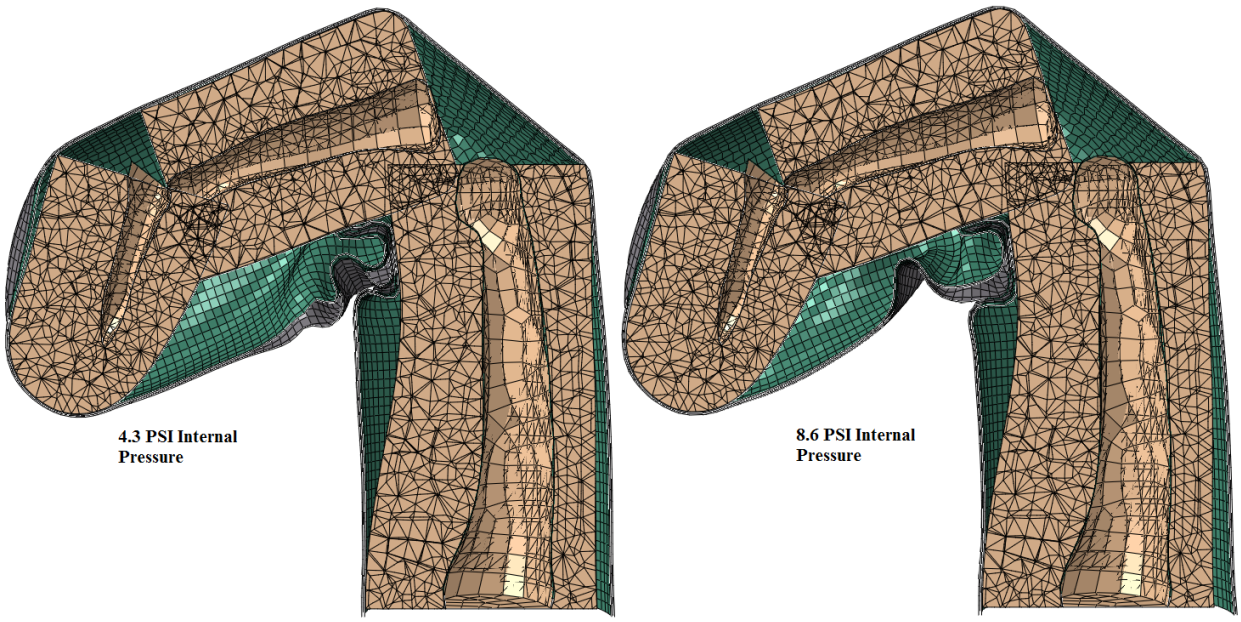

Figure 4.39: Glove Internal Pressure Comparison - Deformed Configurations

4.4.5 Pressure Bladder Thickness Effects

Figure 4.40 shows the effects of bladder thickness on glove resistance about the DIP joint. Here, one can see that increasing the bladder thickness from a value of 0.15 mm to 0.3 mm, an approximately 30% increase in joint torque about the DIP joint at 45 degrees of rotation occurs. This is a significant increase in resistance, however, the increase is not constant throughout the entire motion of the finger.

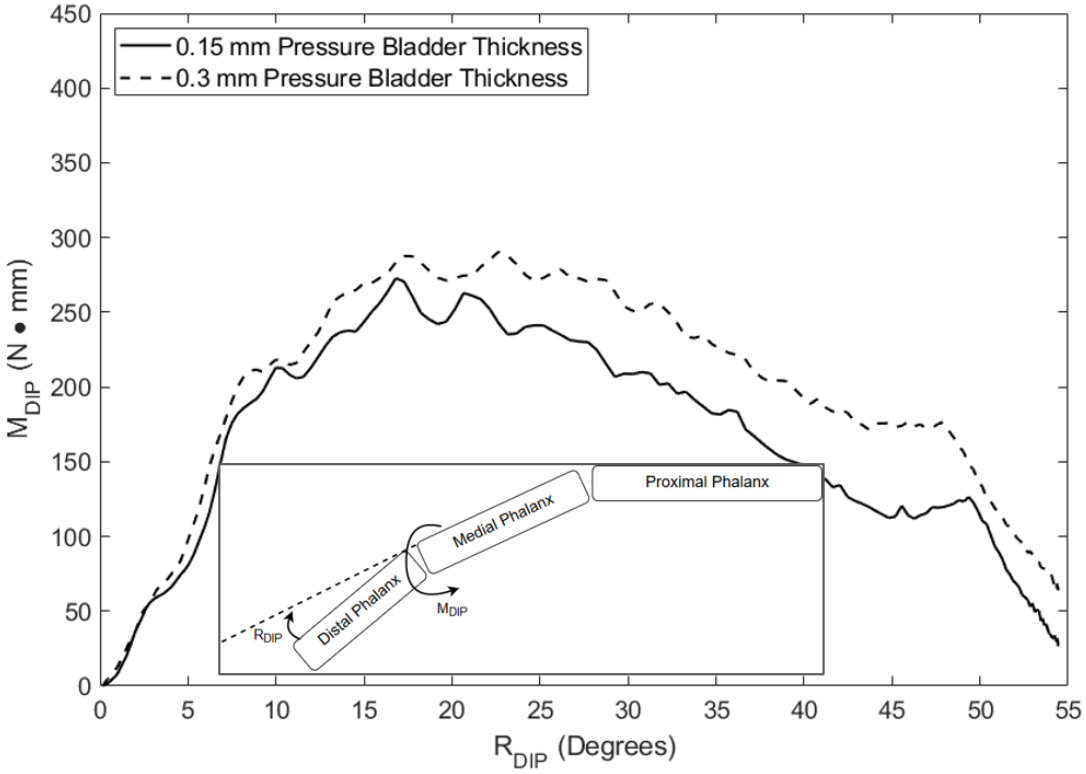

Figure 4.40: Effect of Pressure Bladder Thickness on M_{DIP}

Figure 4.41 shows the effects of bladder thickness on glove resistance about the PIP joint. Here, one can see an increase in glove resistance about the PIP joint similar to that seen in the DIP joint.

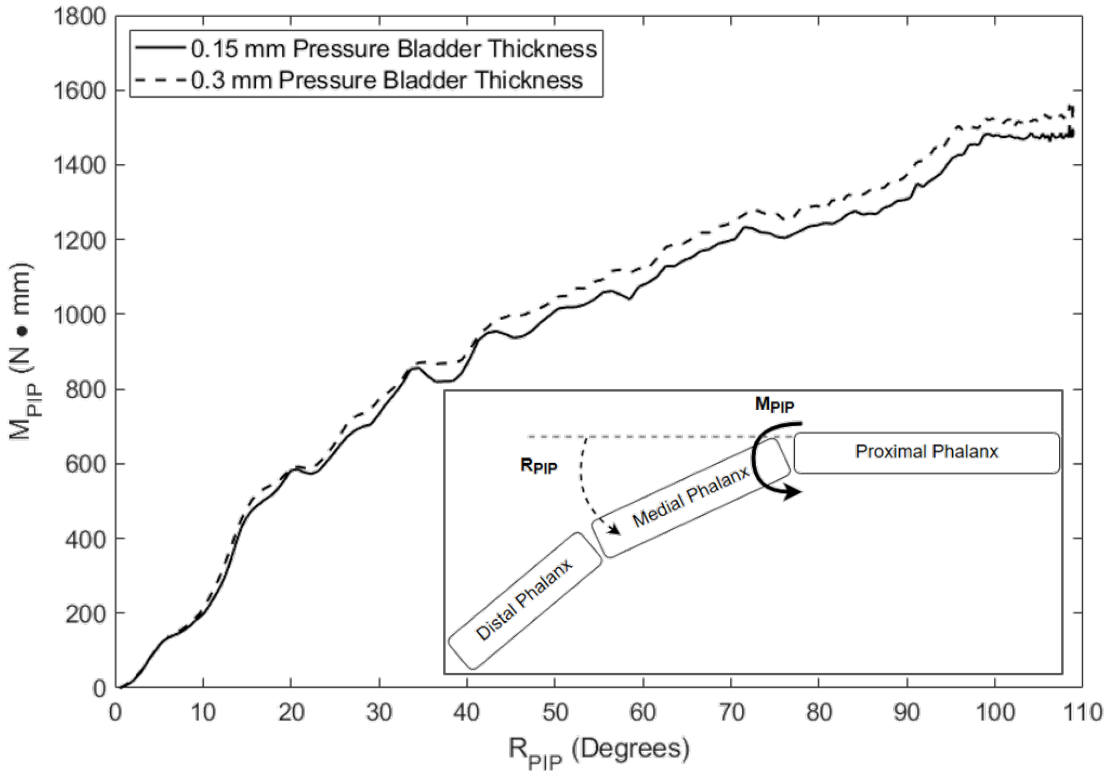

Figure 4.41: Effect of Pressure Bladder Thickness on M_{PIP}

Figure 4.42 shows the deformed configurations of a glove design with 0.15 mm pressure bladder thickness and 0.3 mm pressure bladder thickness with all other design parameters held constant. Here, one can see that the thicker pressure bladder results in more bunching of the glove. In fact, at the maximum amount of bending, the thicker pressure bladder causes the bunching of the glove to contact the palmar surface of the medial finger segment in two locations, providing more resistance to motion about the PIP joint as seen in Figure 4.41.

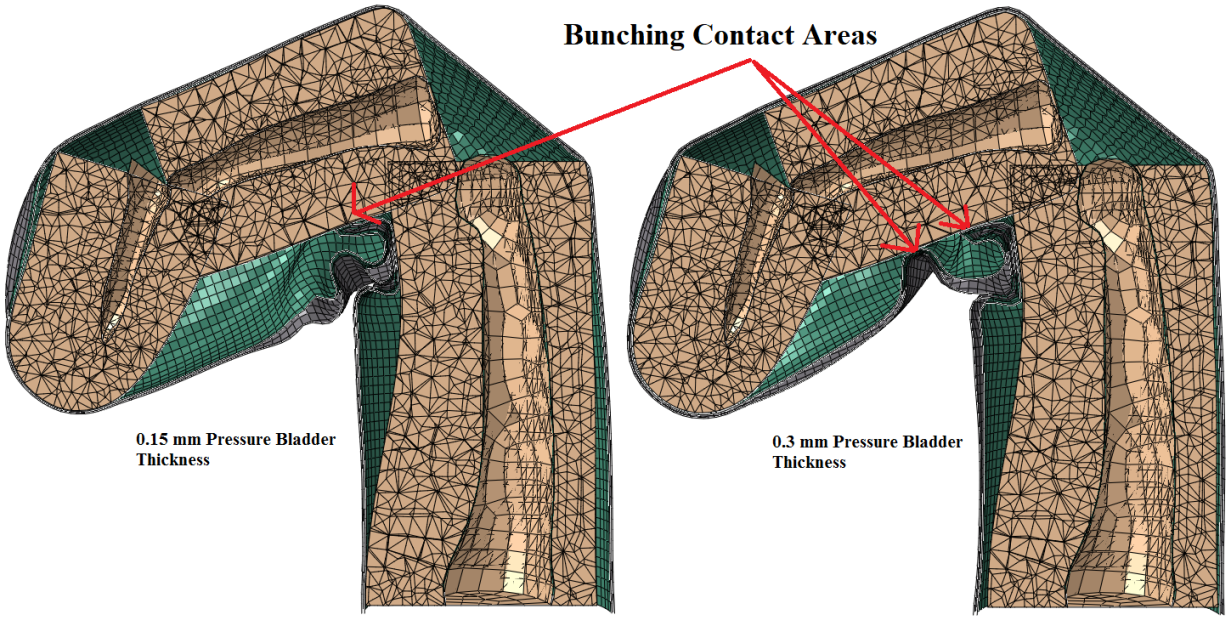

Figure 4.42: Pressure Bladder Thickness Comparison - Deformed Configurations

4.4.6 Restraint Layer Thickness Effects

Figure 4.44 shows the comparison between joint torque about the DIP joint for a restraint layer thickness of 0.3 mm and 0.45 mm. One can see an increase in glove resistance of nearly 100% when considering the effects averaged over all other cases.

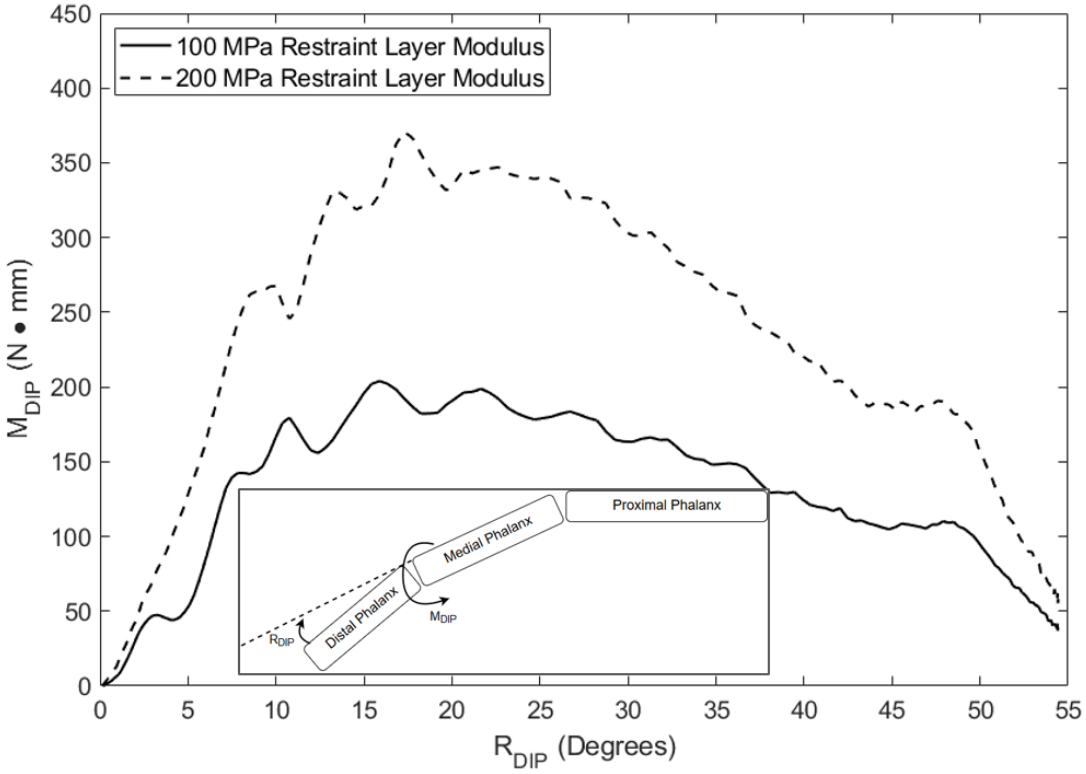

Figure 4.43: Effect of Restraint Layer Thickness on M_{DIP}

Figure 4.44 shows the compartion between joint torque about the PIP joint for the two levels of restraint layer thickness. Similar to the results for joint torque about the DIP joint, increasing the thickness of the restraint layer from 0.3 mm to 0.45 mm increases the resistance of the glove about the PIP joint by nearly 60% at 110 degrees of rotation of the PIP joint.

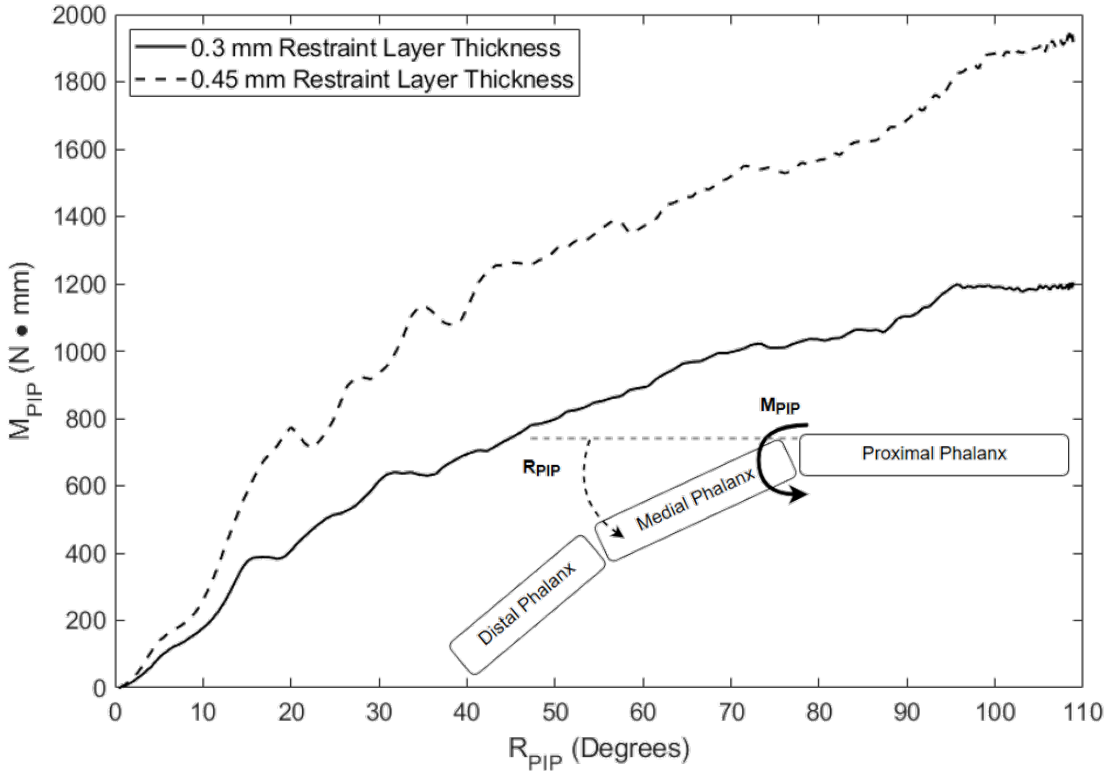

Figure 4.44: Effect of Restraint Layer Thickness on M_{PIP}

Figure 4.45 shows the deformed configurations for a restraint layer thickness of 0.3 mm and 0.45 mm with all other design parameters held constant. Here, one can see that there is a significantly different response of the glove between the designs. The thicker restraint layer causes the glove to not stretch as easily and bunch much differently than the thinner design. Not only does the thicker restraint layer material provide more resistance due to the in-plane stretching during bending, it also provides more resistance when bunched, significantly increasing the resistance of the glove. While doubling the pressure bladder thickness (low value of 0.15 mm and high value of 0.3 mm) increased the glove resistance about the PIP joint by approximately 20%, a smaller increase in restraint layer thickness (low value of 0.3 mm and high value of 0.45 mm) showed a much larger effect on glove resistance (seen in Figures 4.43 and 4.44).

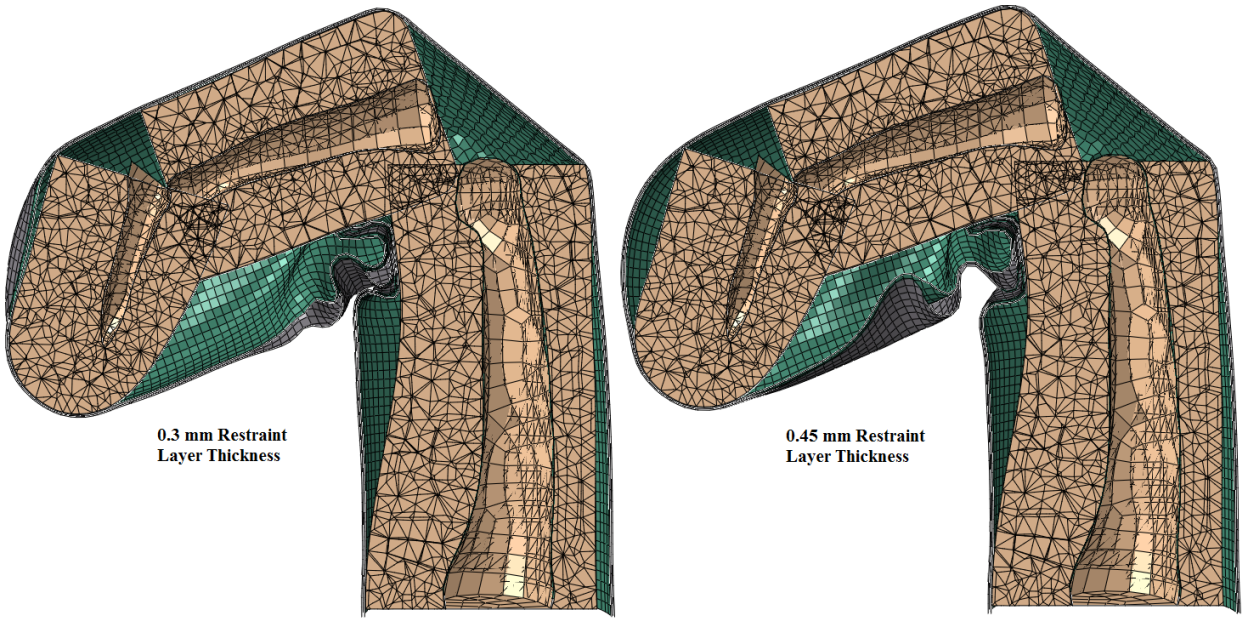

Figure 4.45: Restraint Layer Thickness Comparison - Deformed Configurations

4.4.7 Pressure Bladder Material Modulus Effects

Figure 4.46 shows the effects of the pressure bladder modulus on overall glove resistance about the DIP joint. Both designs exhibit similar response.

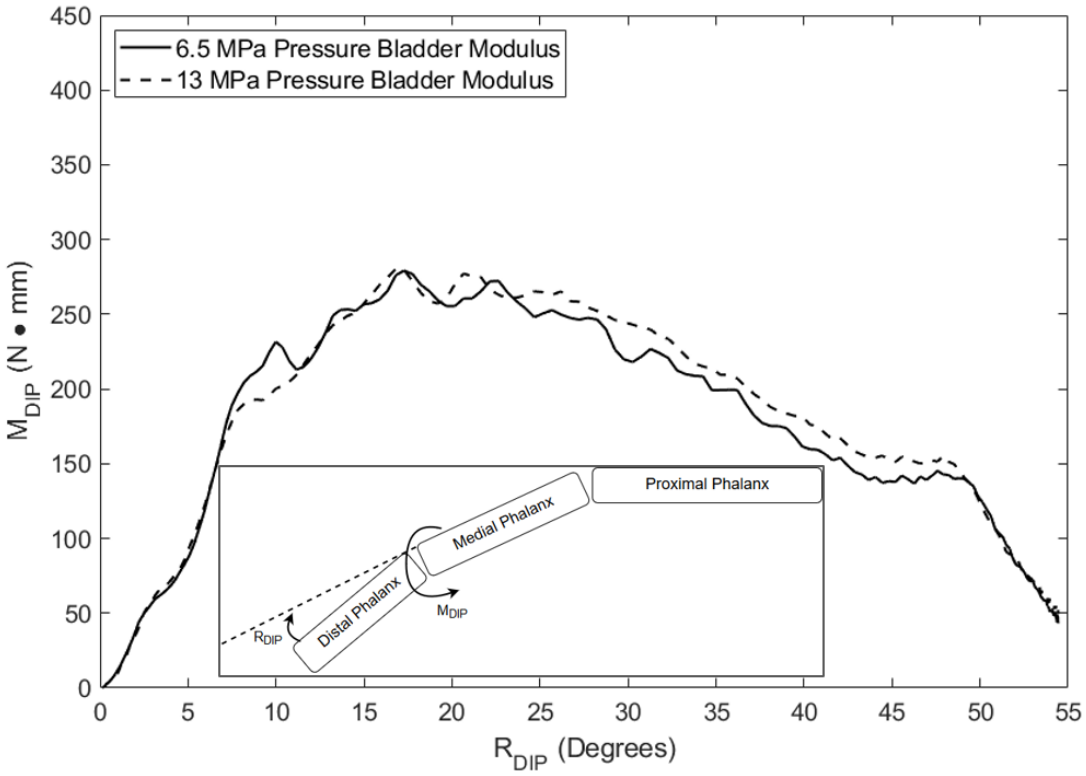

Figure 4.46: Effect of Pressure Bladder Modulus on M_{DIP}

Figure 4.47 shows the comparison of joint torque about the PIP joint for a pressure bladder stiffness of 6.5 MPa and 13 MPa. One can see that doubling the stiffness of the pressure bladder (from 6.5 MPa to 13 MPa) had no noticeable effect on the glove resistance about either the DIP or PIP joints.

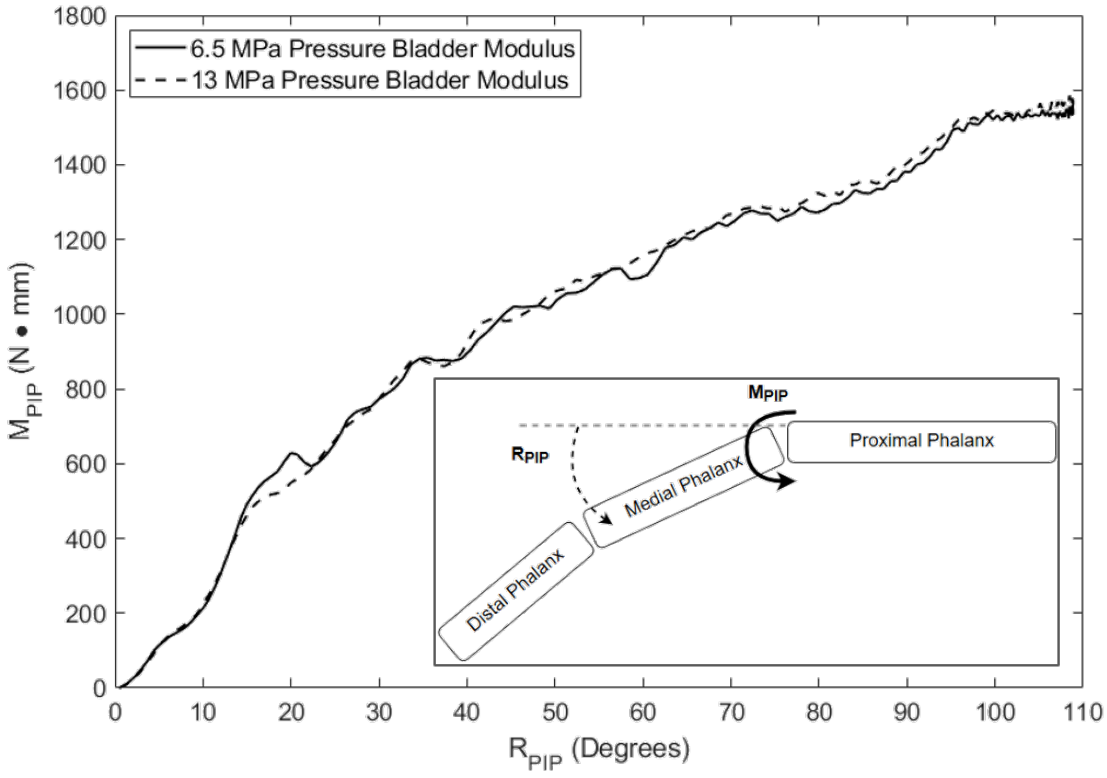

Figure 4.47: Effect of Pressure Bladder Modulus on M_{PIP}

Figure 4.48 shows the deformed configurations of pressure bladder stiffness of 6.5 MPa and 13 MPa with all other design parameters held constant. Here, one can see a significant difference in the bunching behavior of the pressure bladder. The stiffer pressure bladder material bunches, and contacts the finger, in two distinct locations. While one would expect a significant increase in resistance due to this (and the in-plane stretching of the pressure bladder), the restraint layer is the dominant factor in the resistance of the resulting glove.

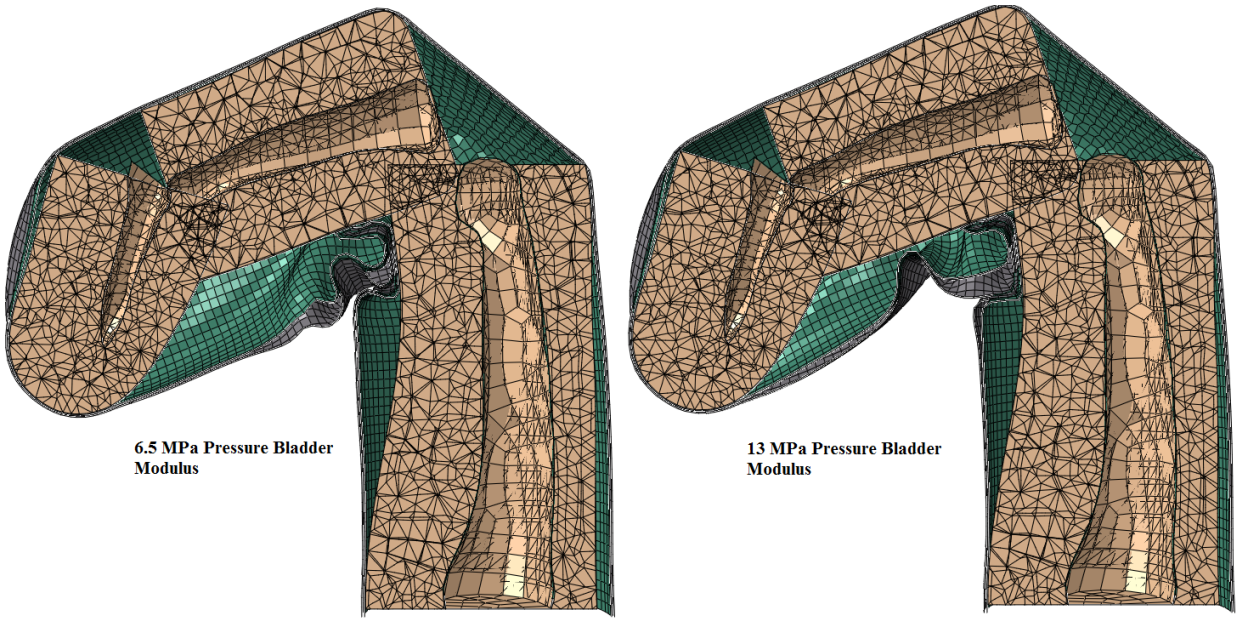

Figure 4.48: Pressure Bladder Modulus Comparison - Deformed Configurations

4.4.8 Restraint Layer Material Modulus Effects

Figure 4.49 illustrates the large effect doubling the modulus of the restraint layer (from 100 MPa to 200 MPa) has on the resulting glove resistance about the DIP joint.

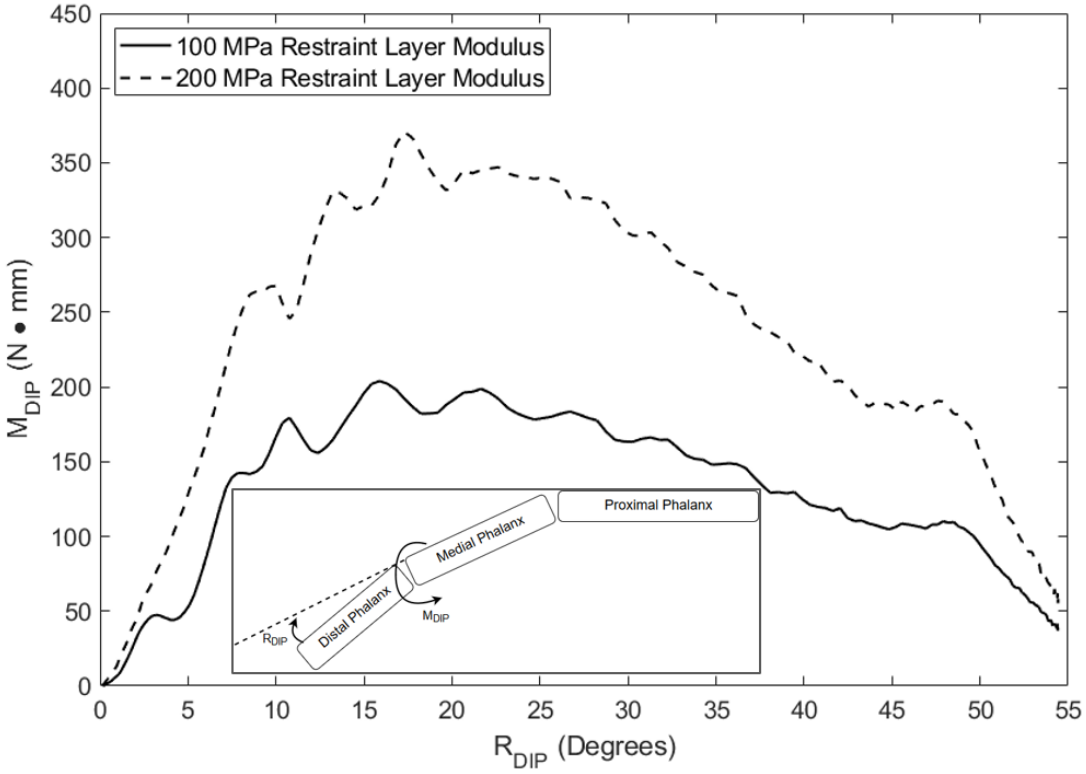

Figure 4.49: Effect of Restraint Layer Modulus on M_{DIP}

Figure 4.50 shows the joint torque about the PIP joint for the restraint layer stiffness of 100 MPa and 200 MPa. At 100 degrees of rotation of the PIP joint, the stiffer restraint layer results in a glove resistance more than double that of the more compliant material.

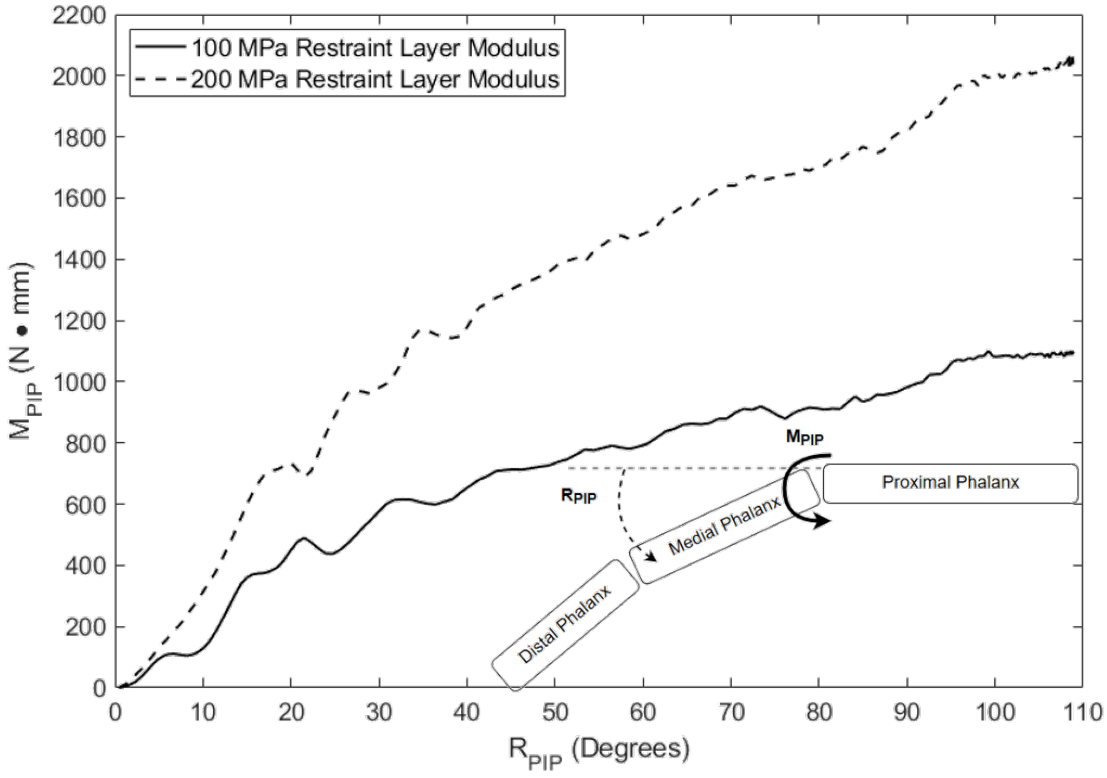

Figure 4.50: Effect of Restraint Layer Modulus on M_{PIP}

Figure 4.51 shows the deformed configurations for a restraint layer stiffness of 100 MPa and 200 MPa with all other design parameters held constant. Similar to the pressure bladder thickness comparison, one can see a significantly different bunching response of the glove for the two restraint layer stiffnesses. This change in bunching response, combined with the stiffer material, explain the significant effective resistance increase seen with the stiffer restraint layer material.

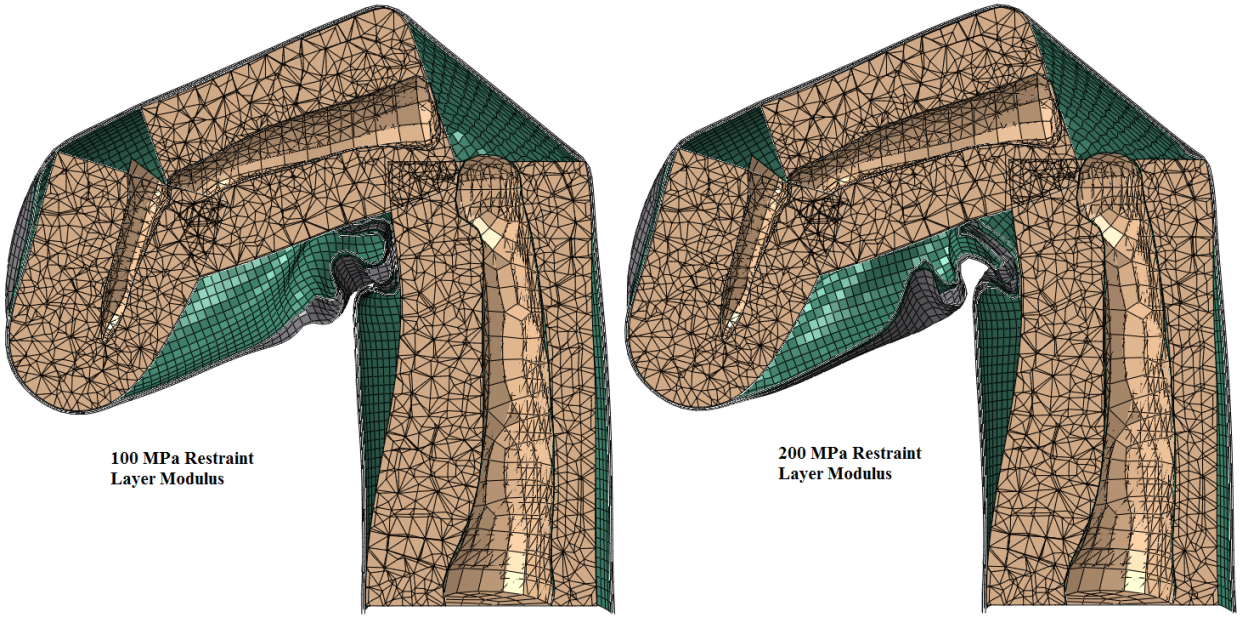

Figure 4.51: Restraint Layer Modulus Comparison - Deformed Configurations

4.4.9 Summary of Parametric Study

From the results presented in this section, it is clear that the thickness and stiffness of the restraint layer have the largest effect on glove resistance out of all of the tested design variables. This result is quite logical. As the role of the restraint layer is to carry all of the man and pressure induced loads inside of the glove and as the pressure bladder is not carrying much of these loads, it is logical that the stiffness and thickness of the pressure bladder will not have much of an effect on the performance of the glove. Because of this, altering the stiffness and thickness of the restraint layer should have a large effect. Additionally, the previous results also show that the location and number of convolutes does not have a substantial effect on glove performance. However, the size (i.e. the radius) of the convolutes does have an effect on the glove resistance.

5. SUMMARY AND CONCLUSIONS

5.1 Summary and Conclusions

In conclusion, this research project developed a robust finite element model of the interaction between a notional human index finger, index finger of the pressure bladder and restraint layer of an EVA glove. While a number of simplifying assumptions (primarily on material response and glove finger geometry) were made for this first effort, qualitative agreement with the limited existing experimental data provides credibility to this model. However, experimental validation using a similar experimental setup to that used in the finite element model is a necessary next step.

For the model used in this research, there are a number of conclusions and implications that can be made. It was shown that for a given design, increasing the internal pressure of the glove has a small impact on the overall resistance provided by the glove. However, the results from the parametric study show that when averaged over a number of designs, increasing the internal pressure of the glove from 4.3 PSI to 8.6 PSI does not have a significant effect. This result illustrates a serious disadvantage of the Main Effects methodology. By averaging results across many cases, it is possible that the average effect is negligible while some cases exhibit large effects. Therefore, it is important to validate the results from a parametric study by viewing the effects on designs one is most interested in. Additionally, as a simplifying assumption of constant internal pressure was made, the contribution to glove resistance from pressure can only occur through keeping the material of the glove away from the neutral axis and limiting bunching of the glove. In reality, it is plausible that the internal pressure of the glove does not remain constant as the internal volume of the glove changes. If that were the case, changing the internal pressure of the glove would require work to compress the oxygen, therefore requiring more work input by the crewmember to deform the glove. This is a phenomenon that is not captured by the current model and additional work should further explore this area.

Additionally, it was shown that the most significant contribution to glove resistance is due to

the material modulus of the pressure bladder and restraint layer. As the restraint layer is more than an order of magnitude stiffer than the pressure bladder, the majority of the glove resistance can be contributed to the material modulus of the restraint layer. The next largest contributing factor to glove resistance is bunching of the glove during bending. The effect of bunching is reduced with the addition of pressure, however it still remains a large contributor to overall resistance provided by the glove during large motions of the finger.

The parametric study showed that the most sensitive design variables are the thickness and modulus of the restraint layer and the thickness of the pressure bladder. Additionally, the convolute radius has a small effect on the overall glove resistance. While experimental validation of the presented finite element model is needed, from this preliminary study, a number of recommendations can be made in order to improve the performance of an EVA glove finger.

Care should be taken to keep the thickness and material modulus to a minimum in the restraint layer. As the thickness and modulus of the restraint layer contribute to overall glove resistance through both stretching and bunching, a reduction in material modulus causes a significant decrease in the effective resistance of that glove. Careful analysis should be performed to determine where the majority of the material is needed and what stiffness and material orientation is necessary to carry all of the man and pressure induced loads inside of the glove. Additionally, convolutes should be incorporated wherever possible. The presence of convolutes in the pressure bladder significantly reduces the overall resistance, and it is presumable that a similar feature in the restraint layer would provide similar performance benefits. The presence of convolutes causes a reduction in effective strain in the pressure bladder and effectively delays wrinkling and bunching of the glove, resulting in a more compliant glove. Further analysis and refinement of the pre-bunching of the restraint layer is necessary.

Finally, careful design should be used to reduce the amount of bunching of the glove wherever possible. As the second largest contributor to glove resistance (second only to the material modulus of the restraint layer), the presence of bunching causes a serious restriction of motion of the finger. Whether manufacturing gloves for a pre-bent neutral configuration or the application of smart

materials, controlling and reducing the amount of wrinkling in the fingers of the glove is crucial. Finally, it should be stated that the scope of this project was limited to the analysis of the pressure bladder and restraint layer of the index finger. Experimental data has shown that the presence of the TMG layer of the glove causes a serious performance decrement as well. Additionally, motions of the MCP joint are just as critical as motions of the PIP joint in grapsing. Therefore, future work should be done to expand the model to include the TMG layer as well as the MCP joint and palm of the hand. Additionally, it is recommended that work be done to incorporate the full-finger idealization for realistic motions of the finger as this will provide results more representative of the real hand-suit interaction. Despite the limitations of this model, it has been shown to be a robust analytical tool that, with further experimental validation, can be a powerful tool in the design and analysis of future EVA gloves.

5.2 Future Work

Future work should first incorporate a more realistic geometric model of the restraint layer including side seams and the pre-bunching due to sizing adjustment chords. Furthermore, material samples should be acquired to characterize material behavior. Following this, the material models of the pressure bladder and restraint layer should be updated to reflect the experimental results. Future work should also seek to develop an experimental setup to validate the results of this model. This experimental setup should incorporate a mechanically actuated finger capable of measuring joint displacement and joint torque similar to that used by Mousavi et al. The results from this experiment should be used to modify and validate the finite element model until agreement is achieved. Following that, the refined model should be used to perform a larger sensitivity analysis of the glove design parameters. With this experimentally validated model, further studies into the contact interaction between the finger and glove can be performed.

REFERENCES

[1] M. Pelegrin, "Space and deep space environment," *Automatic Control 1990*, pp. 1–10, 1991.

[2] R. Pirich, J. Weir, D. Leyble, S. Chu, and M. Digiuseppe, "Effects of the lunar environment on space vehicle surfaces," *2010 IEEE Long Island Systems, Applications and Technology Conference*, 2010.

[3] "Mars facts." Web, NASA.

[4] D. Portree and R. Trevino, "Walking to olympus: An eva chronology," *NASA History Office*, 1997.

[5] "Eva at 50," *Collect Space, Available: http://www.collectspace.com/news/news-031815a-spacewalk-50th-alexei-leonov.html*.

[6] "Ed white performing first eva," *Smithsonian National Air and Space Museum, Available: https://airandspace.si.edu/exhibitions/outside-the-spacecraft/online/image-detail.cfm?id=8548*.

[7] "Gt 12 earth sky eva," *NASA, Available: https://archive.org/details/S66-63536*.

[8] "Apollo 11," *NASA, Available: https://www.hq.nasa.gov/alsj/a11/AS11-40-5903HR.jpg*.

[9] "Skylab 2 eva," *Astronautix, Available: http://www.astronautix.com/s/skylab2.html*.

[10] "Personal interview: Dr. bonnie j. dunbar," *Texas AM University*, 2019.

[11] K. Thomas and H. McMann, "Us spacesuits," 2006.

[12] "Nasa extravehicular mobility unit (emu) lss/ssa data book," *UTC Aerospace Systems*, 2017.

[13] "Phase vi eva glove," *NASA Suit Up, Available: https://www.nasa.gov/suitup*.

[14] "The space shuttle extravehicular mobility unit," *Suited for Spacewalking*, 1998.

[15] D. Graziosi, J. Stein, A. Ross, and J. Kosmo, "Phase vi advanced eva glove development and certification for the international space station," *SAE Technical Paper Series*, 2001.

[16] "Bladder, glove, phase vi," *Smithsonian National Air and Space Museum, Available: https://airandspace.si.edu/collection-objects/bladder-glove-phase-vi*.

[17] M. Mesloh, S. England, E. Benson, S. Thompson, and S. Rajulu, "The effects of extravehicular activity (eva) glove pressure on hand strength," *Advances in Human Factors and Ergonomics Series Advances in Applied Digital Human Modeling*, pp. 156–165, 2010.

[18] J. O'Hara, J. Cleland, and D. Winfield, "The development of a test methodology for the evaluation of eva gloves," *Journal of Aerospace*, vol. 97, pp. 663–671, 1988.

[19] R. Bishu and G. Klute, "Investigation of the effects of extravehicular activity (eva) gloves on performance," *NASA Technical Paper 3401*, 1993.

[20] R. Bishu, G. Klute, and K. Byungjoon, "The effect of eva gloves on dexterity and tactility," *Human Factors and Ergonomics Society 37th Annual Meeting*, 1993.

[21] R. Bishu and G. Klute, "Force-endurance capabilities of extravehicular activity (eva) gloves at different pressure levels," *NASA Technical Paper 3420*, 1993.

[22] A. Diaz, A. Anderson, and M. Kracik, "Development of a comprehensive astronaut spacesuit injury database," *Advances in Human Factors and Ergonomics Series Advances in Applied Digital Human Modeling*, 2015.

[23] L. Farran, R. Ennos, and E. S.J., "The effect of humidity on the fracture properties of human fingernails," *The Journal of Experimental Biology*, vol. 221, pp. 3677–3681, 2008.

[24] R. A. Opperman, J. M. Waldie, A. Natapoff, D. J. Newman, J. Hochstein, L. Pollonini, R. R. Ansari, and J. A. Jones, "Anthropometric and blood flow characteristics leading to eva hand injury," *SAE Technical Paper Series*, 2009.

[25] C. Reid and S. McFarland, "Feasibility assessment of an extravehicular glove sensing platform to evaluate potential hand injury risk factors," 2015.

[26] S. McFarland and S. Walsh, "Nasa's high performance eva glove: Project element summaries," 2018.

[27] M. Mousavi, S. Appendino, and A. Battezato, "Stiffness of an eva glove: objective evaluation and testing procedures," 2013.

[28] Vishala, W. Scholten, R. Fernandes, B. Dunbar, and D. Hartl, "Finite element analysis of an index finger flexion in an extravehicular activity glove," *AIAA Modeling and Simulation Technologies Conference, 2018*, 2018.

[29] A. Elsabbagh, "Nonlinear finite element model for the analysis of axisymmetric inflatable beams," *Thin-Walled Structures*, vol. 96, pp. 307–313, 2015.

[30] S. Gajbhiye, S. Upadhyay, and S. Harsha, "Finite element analysis of an inflatable torus considering air mass structural element," *Advances in Space Research*, vol. 53, pp. 163–173, 2014.

[31] J. Rowe, S. Smith, and A. Simpson, "Development of a finite element model of warping inflatable wings," *47th AIAA/ASME/ASCE/AHS/ASC Structures, Structural Dynamics, and Materials Conference 14th AIAA/ASME/AHS Adaptive Structures Conference 7th*, 2006.

[32] E. Sosa and J. Wong, "Finite element simulation of deployment of large-scale confined inflatable structures," *Thin-Walled Structures*, vol. 104, pp. 152–167, 2016.

[33] R. Glaser, V. Caccese, and M. Shahinpoor, "Comparative finite element and experimental analysis of a thin deployable membrane space structure," *Finite Elements in Analysis and Design*, vol. 138, pp. 48–65, 2018.

[34] J. Han, E. Yoo, and J. Roh, "Wrinkling control of inflatable booms using smart material patch," *SPIE Smart Structures and Materials*, 2006.

[35] E. Iulanio, R. Potes, S. Langlois, and R. Roumeas, "Validation of the finite element model of an inflatable beam structure using experimental data and study of its behaviour under the effects of the residual trapped air," *Proceedings of the European Conference on Spacecraft Structures, Materials and Mechanical Testing 2005*, 2005.

[36] K. Senda, N. Kishimoto, K. Higuchi, Y. Shoukaku, S. Mizuguchi, T. Ogasawara, and T. Oda, "Finite element method analysis and experiment of 2-dimensional deployable membrane

structures embedding inflatable tubes," *Structures, Structural Dynamics and Materials Conference, 2008*, 2008.

[37] J. Hill and R. Braun, "Explicit finite element analysis of inflatable braided strapped beams," *Aerodynamic Decelerator Systems Technology Conferences, 2015*, 2015.

[38] T. Khalil and et al., "Integrated vehicle-dummy-air bag model for frontal crash simulation by fe analysis," *Crashworthiness and Occupant Protection in Transportation Systems, ASME*, pp. 355–366, 1995.

[39] P. Aghssa and M. Riesner, "The use of finite element method in computing the dynamic pressure inside a fuel tank during vehicle crash to predict fuel leakage," *SAE Internal, Troy Michigan, April 8-10*, 1997.

[40] "Prediction of plastic deformation under contact condition by quasi-static and dynamic simulations using explicit finite element analysis," *Journal of Mechanical Science and Technology*, vol. 30, pp. 5093–5101.

[41] "Efficient solid-shell finite elements for quasi-static and dynamic analyses and their application to sheet metal forming simulation," *Key Engineering Materials*, vol. 651-653, pp. 344–349.

[42] D. Lu, B. Shahidi, C. Rivard, and R. Li, "Some studies for the application of explicit fe codes in simulation of quasi-static testes," *1997 ASME Mechanical Engineering Congress and Exposition*, 1997.

[43] "Dynamic-explicit elastic plastic finite-element simulation of hemispherical punch-drawing of sheet metal," *Engineering Computations*, vol. 13, pp. 327–338.

[44] "Explicit dynamic formulation to demonstrate compliance against quasi-static aircraft seat certification loads (cs25.561) - part i: Influence of time and mass scaling," *Journal of Aerospace Engineering*, vol. 228(11), pp. 1982–1995.

[45] "Explicit dynamic formulation to demonstrate compliance against quasi-static aircraft seat certification loads (cs25.561) - part ii: Influence of body blocks," *Journal of Aerospace Engineering*, vol. 228(11), pp. 1890–1903.

[46] "Comparison of the implicit and explicit finite element methods in quais-static analyses of rubber-like materials," *Constitutive Models for Rubber*, pp. 517–522.

[47] NASA, "Nasa-std-3001 vol 1," 2015.

[48] T. Belytschko, J. Ong, W. Liu, and J. Kennedy, "Hourglass control in linear and nonlinear problemts," *Computer Methods in Applied Mechanics and Engineering*, vol. 43, pp. 251–276, 1984).

APPENDIX A

HOURGLASS EFFECT OF SHELL ELEMENTS IN PRESSURE BLADDER MODEL

In the previously discussed finite element model of the interaction between a human index finger and EVA glove pressure bladder and restraint layer, the pressure bladder and restraint layer were modeled using quadrilateral shell elements using a reduced integration scheme. These are denoted S4R elements in Abaqus. In general, a 4 node quadrilateral finite element requires 4 integration points for full-quadrature integration. However, it is desirable used a reduced integration scheme that employs only one integration point. The advantage to this is significantly reduced computational expense. However, by using a reduced integration scheme, one can introduce a form of mesh instability known as hourglassing. Hourglassing is spurious deformation of the finite element mesh resulting in zero-energy deformation of the mesh [48]. Figure A.1 shows an example of such phenomenon in a 2-D quadrilateral element with a single integration point. The element is subjected to some bending, resulting in nodal displacements, however both of the dotted line do not change length or orientation. Therefore, at the integration point, zero strain is imparted and therefore the element experiences zero stress. Hence the element is deformed with zero strain energy.

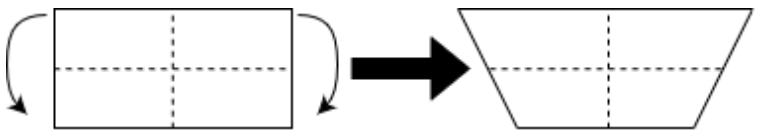

Figure A.1: Example of Zero-Energy Deformation

Hourglassing can be controlled by introducing artificial stiffness to the hourglass deformation mode, introducing an artificial viscosity to the material, by refining the mesh or by using fully integrated elements [48].

It is recognized that the undesirable phenomenon of the hourglass effect of the first-order shell elements in the pressure bladder model occurs during the bending analysis. Figure A.2 illustrates an example of such hourglassing in the pressure bladder during bending.

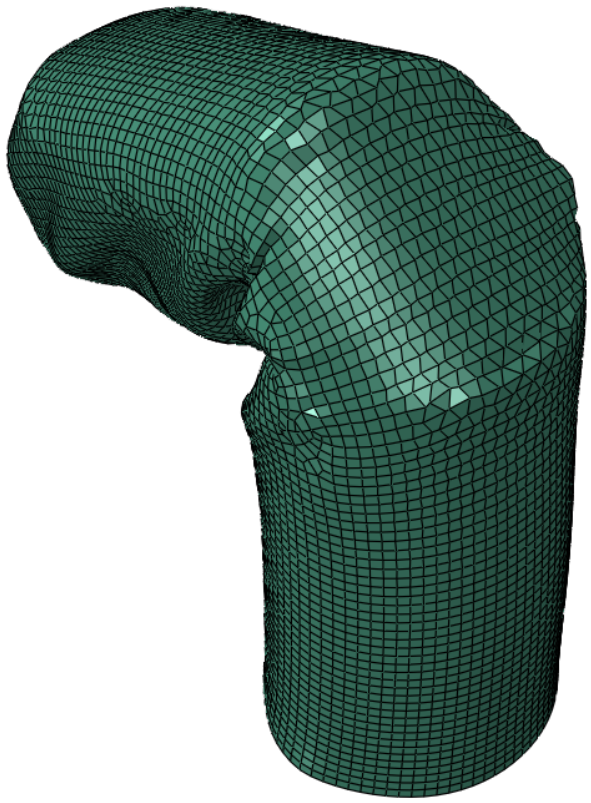

Figure A.2: Example of Hourglassing in Pressure Bladder

While the presence of hourglassing in the pressure bladder is undesirable, it is hypothesized that as the pressure bladder had minimal contribution to the overall resistance of the glove, the mesh instability in the pressure bladder has minimal effect on the response of the glove. To substantiate this claim, the model was run with fully-integrated S4 elements in the pressure bladder with all other variables held constant. Figure A.3 shows the pressure bladder deformed configuration for both full integration and reduced integration. Here, one can see that the use of full integration removes the hourglassing effect in the pressure bladder.

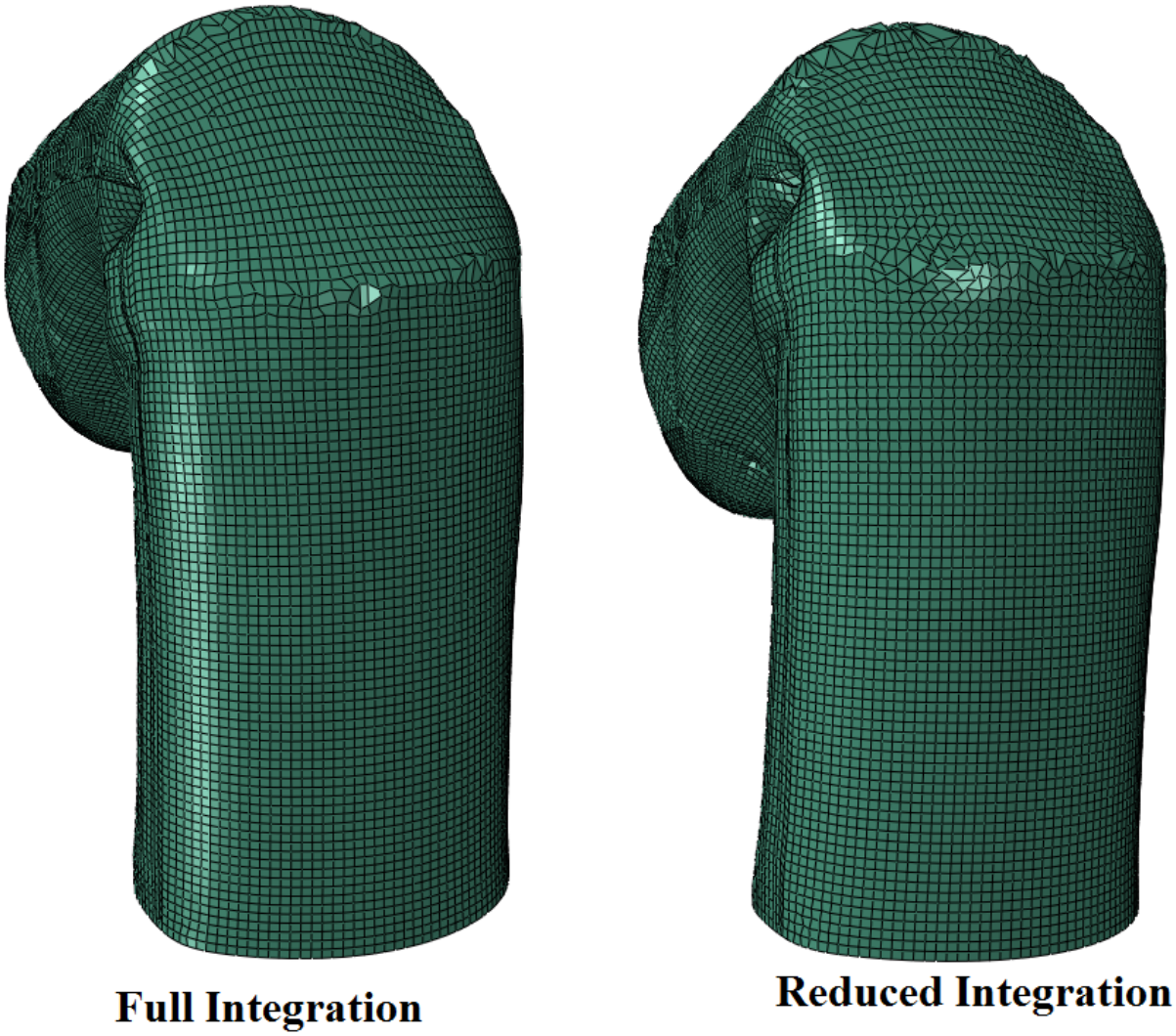

Figure A.3: Deformed Configuration of Pressure Bladder with Full and Reduced Integration

Figure A.4 shows the comparison in the resistance caused by the glove for both the full integration and reduced integration.

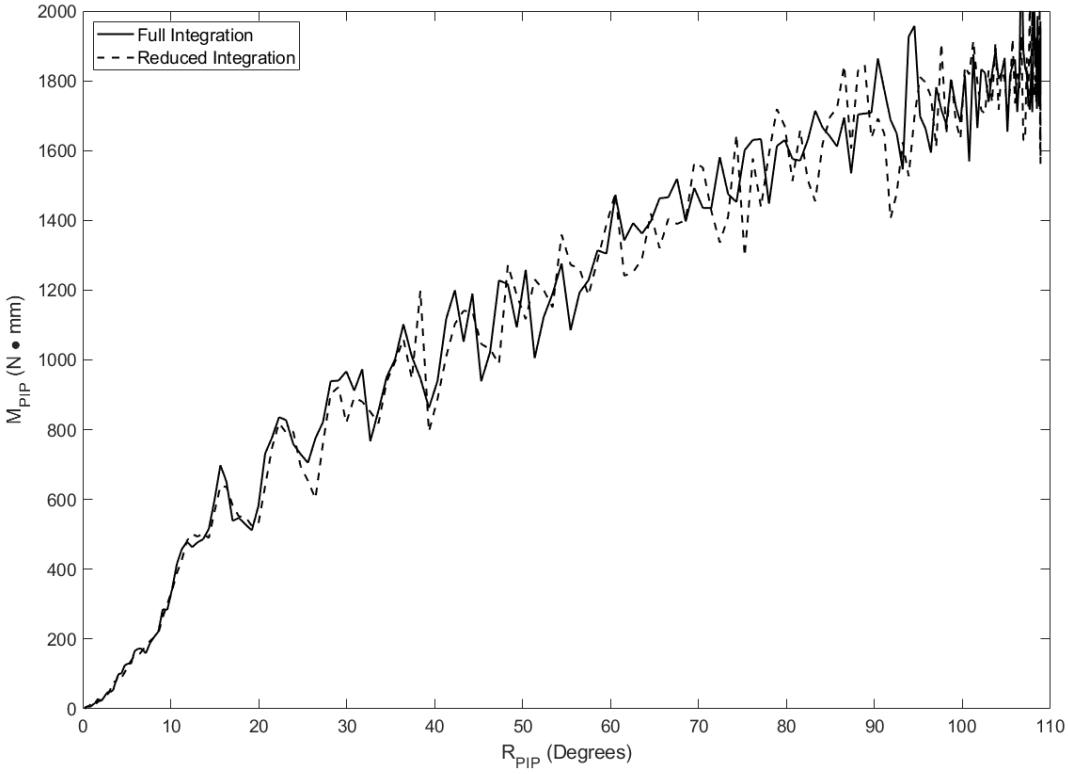

Figure A.4: M_{PIP} vs. R_{PIP} for Full Integration and Reduced Integration

Here, one can see that the hourglassing present in the reduced integration has minimal effect on the overall response of the glove. Although hourglassing is a highly undesirable effect, and future work should eliminate such phenomenon from the model, it was shown that the presence of hourglassing in the previously discussed results had minimal effect on said results.